Cavity-atom interactions in a thermal strontium beam

Development of a simple apparatus for quantum metrology

ACADEMISCH PROEFSCHRIFT

ter verkrijging van de graad van doctor
aan de Universiteit van Amsterdam
op gezag van de Rector Magnificus
prof. dr. ir. P.P.C.C. Verbeek
ten overstaan van een door het College voor Promoties ingestelde commissie,
in het openbaar te verdedigen in de Agnietenkapel
op donderdag 26 juni 2025, te 10.00 uur

door Camila Beli Silva

geboren te Aguaí

Promotiecommissie

Promotor:	prof. dr. F. E. Schreck	Universiteit van Amsterdam
Copromotor:	dr. S.A. Schäffer	Københavns Universitet
Overige leden:	dr. P.W. Courteille	Universidade de São Paulo
	dr. J.C.J. Koelemeij	Vrije Universiteit Amsterdam
	dr. A. Safavi Naini	Universiteit van Amsterdam
	prof. dr. M.S. Golden	Universiteit van Amsterdam
	prof. dr. K. van Druten	Universiteit van Amsterdam

Faculteit der Natuurwetenschappen, Wiskunde en Informatica

The research for this doctoral thesis received financial assistance from the European Union's Horizon 2020 research and innovation programme, grant agreement No 820404 (iqClock project, iqclock.eu) and No 860579 (MoSaiQC project, mosaiqc.eu). It was furthermore financed through the Dutch National Growth Fund (NGF), as part of the Quantum Delta NL programme (quantumdelta.nl). The research was carried out at the Van der Waals-Zeeman Institute, Institute of Physics, University of Amsterdam.

Summary

In this thesis, I report on my work under the supervision of Prof. Dr. Florian Schreck and Dr. Stefan A. Schäfer on the kHz superradiant clock at the University of Amsterdam. The research presented here revolves around a single theme: the development of a superradiant clock based on the kHz transition of strontium-88. To date, this experimental apparatus remains the only one of its kind.

The main scientific goal of this project has been to experimentally realize the regime of continuous superradiance. While this goal has not yet been reached, we have made significant progress in paving the way toward its achievement. The obstacles encountered during this journey forced us to come up with ideas to overcome them, and this is what is presented in Chapter 3, where the modifications made to the apparatus are detailed. In Chapter 6, a new method to transversely cool the dense atomic beam and its experimental implementation is discussed.

After upgrading the system, light amplification due to collective atomic behavior from the atoms in the upper lasing state $^3P_1$ of strontium was observed, reaching up to 500%. This is 40 times greater than previously reported and is thoroughly discussed in Chapter 7.

Finally, in Chapter 8, the exciting and intriguing behavior of atomic emission onset is presented. This represents a major achievement during my PhD, as it marks the first measurement in which collective emission from the atoms is observed, though it is not sustained. Although there are still riddles to be solved and further investigations to be made, it is believed that in the near future, our experiment will reach its goal and become a continuous superradiant laser.

Samenvatting

In dit proefschrift rapporteer ik over mijn werk onder leiding van Prof. Dr. Florian Schreck en Dr. Stefan A. Schäfer over de kHz superradiënte klok aan de Universiteit van Amsterdam. Het onderzoek dat hier wordt gepresenteerd draait om één centraal thema: de ontwikkeling van een superradiënte klok op basis van de kHz-overgang van strontium-88. Tot op heden is dit experimentele apparaat het enige van zijn soort.

Het belangrijkste wetenschappelijke doel van dit project is geweest om experimenteel het regime van continue superradiantie te realiseren. Hoewel dit doel nog niet is bereikt, hebben we aanzienlijke vooruitgang geboekt in het effenen van de weg naar het behalen van dit doel. De obstakels die we onderweg tegenkwamen, dwongen ons om ideeën te bedenken om deze te overwinnen, en dit wordt gepresenteerd in Hoofdstuk 3, waarin de aangebrachte wijzigingen aan het apparaat worden gedetailleerd. In Hoofdstuk 6 wordt een nieuwe methode besproken die is geïmplementeerd om de dichte atoomstraal te koelen.

Na de upgrade van het systeem werd lichtversterking door collectief atomaire gedrag van de atomen in de bovenste lasstaat $^3P_1$ van strontium waargenomen, met een versterking van maar liefst 500%. Dit is 40 keer groter dan de eerdergrondig besproken in Hoofdstuk 7.

Ten slotte wordt in Hoofdstuk 8 het opwindende en intrigerende gedrag van de opkomst van atomaire emissie gepresenteerd. Dit vertegenwoordigt een belangrijke prestatie tijdens mijn promotieonderzoek, aangezien het de eerste meting markeert waarin collectieve emissie van de atomen wordt waargenomen, hoewel deze niet wordt gehandhaafd. Hoewel er nog raadsels zijn die opgelost moeten worden en verder onderzoek nodig is, wordt verwacht dat ons experiment in de nabije toekomst zijn doel zal bereiken en de eerste continue superradiënte laser zal produceren.

"Eu vi muitos cabelos brancos
Na fronte do artista
O tempo não para e, no entanto, ele nunca envelhece
Aquele que conhece o jogo
Do fogo das coisas que são
É o Sol, é o tempo, é a estrada, é o pé e é o chão."
- Caetano Veloso, *Força Estranha*

Aos meus pais e conterraneos.

Contents

Chapter 1

Introduction

The history of humanity and timekeeping could be told side by side. One could argue that the field began as soon as humans started to perceive and measure the passage of time. Throughout history, humans have devised various methods to track time. Initially, they relied on observation of the stars and celestial movements to predict seasonal changes, serving as a guide for planting and harvesting crops.

As civilization advanced, artifacts were developed to measure time more precisely. Sundials, water clocks, and candles were among the early tools used for this purpose. With technological progress, these "natural" artifacts gave way to fully mechanical devices, such as pendulum clocks. A century ago, the age of electronic clocks began, marked by quartz-crystal-based clocks that achieved at least an order of magnitude greater accuracy than mechanical clocks.

However, the demand for even greater precision and accuracy continued to grow. It became evident that no mechanical or electronic clocks were perfectly identical; their "ticks" of time inevitably drifted apart. This realization led to a revolutionary idea: Why not return to nature itself? Atoms of the same element, unlike mechanical or electronic components, are fundamentally identical everywhere in the universe, on Earth or on the far side of the galaxy, under the same conditions. By using these perfectly uniform structures as a reference for time, humanity entered a new era of timekeeping: the age of atomic clocks.

In simple terms, an atomic clock uses the resonant frequency of atoms as a reference for measuring time. In 1955, a device based on a beam of hot cesium atoms addressed by microwave fields became the first atomic clock to be used as a time standard. This device achieved remarkable accuracy, with an error of approximately 20 parts per billion [1]. In 1968, the second was defined as $9\,192\,631\,770$ cycles of the unperturbed ground-state hyperfine transition frequency of the cesium 133 atom [2].

Developments in atomic physics have driven continuous progress in the preparation, manipulation, and detection of atoms, molecules, and ions. Since the 1990s, breakthroughs such as laser cooling and trapping, and experimental methods for preparing new states of matter and control of interaction between particles have significantly advanced techniques for the precise control and manipulation of quantum states [3, 4]. These innovations have enabled scientists to develop new generations of atomic clocks with unprecedented accuracy and stability. The accuracy of state-of-the-art strontium optical lattice clocks has now reached approximately 2×10^{-18}[5], meaning that they would deviate by no more than one second over 15 billion years, exceeding the age of the Universe.

The interest in atomic clocks extends far beyond timekeeping. They are used in areas such as navigation, communication, and geodesy [6]. Moreover, the enhancement of precision metrology has deepened our understanding of fundamental physics through studies of phenomena such as the electric dipole moment, gravitational redshift, and measurements of the fine-structure constant [7, 8, 9].

This thesis presents a pathfinder for the continuous development of quantum metrology. It introduces a novel active frequency reference based on the phenomenon of continuous superradiance.

1.1 Superradiance

When an ensemble of N atoms is prepared in the upper level of a two-level system with an open transition, it decays to the lower energy level via spontaneous emission. The atoms within the ensemble are assumed to interact independently with the radiation field. The emitted field is isotropic, and the decay follows an exponential law, with the characteristic decay time τ_{sp} related to the transition linewidth by the reciprocal relation $\gamma = 1/\tau_{sp}$.

However, when the ensemble is confined within a region smaller than the wavelength of the radiation field, it exhibits an enhanced emission rate compared to independent spontaneous emission. The atoms begin to radiate spontaneously much faster and more intensely than independent atoms, resulting in emission that occurs over a duration of t_{sp}/N with an intensity proportional to the square of the number of atoms in the ensemble, and, depending on the geometry of the atoms' arrangement, the emission occurs in a defined direction. The radiation emission profile is distinctly different from an exponential decay [10]. This phenomenon, known as superradiance, occurs due to spontaneous phase locking of atoms within the ensemble. It was first described by Dicke in 1954 [11]. His approach revealed that, under these conditions, all atoms interact with a common radiation field, behaving as a collective quantum system. This contrasted with the prevailing treatment at the time, which considered atoms to radiate independently.

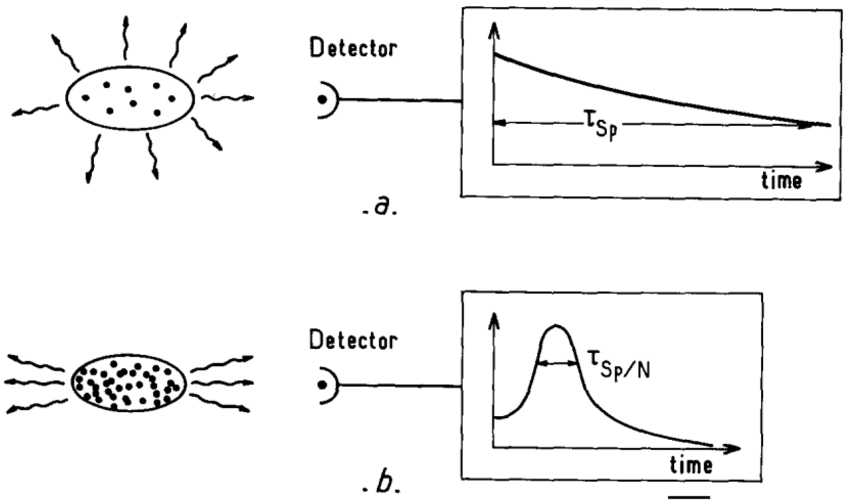

FIGURE 1.1: Contrast between the fundamental properties of ordinary and superradiant emission. a) Ordinary emission from an ensemble of atoms, which is isotropic and follows an exponential decay with a characteristic time of τ_{sp}. b) Superradiant emission from an ensemble of N atoms, characterized by a pulse with a significantly shortened duration, scaling as τ_{sp}/N . Figure reproduced from [10].

Since the superradiant phenomenon was first described by Dicke, it has remained a topic of long-standing interest. One direct application that might be considered is its potential as a tool for retrieving light from a narrow transition. This is particularly relevant for clock transitions which typically have linewidths on the order of mHz or lower.

As mentioned previously, the spontaneous emission rate is inversely proportional to the linewidth. Consequently, once atoms are excited to the upper level of such a transition, it can take up to several minutes for a single photon to be emitted. This emission occurs in arbitrary directions, leading to lower detection efficiencies.

The potential of superradiance lies in its ability to generate an enhanced collective emission signal from narrow transitions on a timescale shorter than that of the natural decay time. This emitted light can then be used as a direct frequency reference, giving rise to a new type of atomic clock, known as an active atomic clock [12].

1.2 Establishing superradiance

When the ensemble is confined within a region smaller than the wavelength of the radiation field, the atoms can emit superradiantly. However, if the atoms emit with random dipole phases, the total emission will experience random interference, and consequently the emission will not be superradiant. The total power will scale only with the number of atoms N , as shown in Figure 1.2.

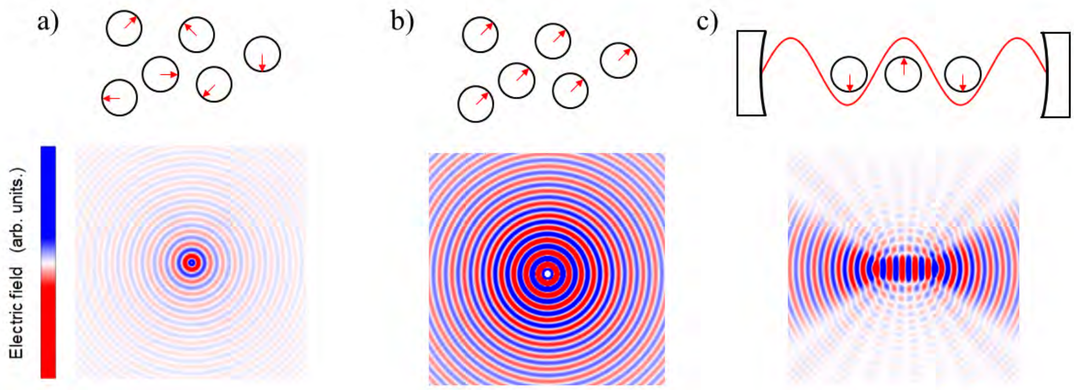

FIGURE 1.2: Emission of phased array emitters in different configurations. a) N emitters spaced more closely than the emission wavelength, with dipoles having random phases. The resulting emitted electric field undergoes random interference, leading to a total emitted power that scales proportionally to the number of emitters. b) Emitters in the same spatial configuration as in a) but now with identical dipole phases. The emitted electric fields constructively interfere, resulting in a total power that scales with the square of the number of emitters. c) Atoms spaced at half the wavelength within the mode of an optical cavity, with alternating phases. The resulting field constructively interferes along the cavity axis, leading to an output power that also scales with the square of the number of emitters.

For a scaling N^2, the atoms must have the same dipole phase. However, achieving the small confinement criterion is experimentally challenging. This approach will face issues such as collisions and molecule formation. One way to overcome this challenge is to couple the atoms by placing them in an optical cavity mode. This coupling will lead to the atoms' emission dipoles being phase synchronized with the cavity field, whenever the atoms are in the cavity mode. This not only achieves the desired power scaling but also engineers the emission direction, being preferentially along the cavity mode direction, which improves the detection of the superradiant emission.

In order to understand how superradiance is established, a formalism that offers a visual representation of the system will be introduced: the Bloch sphere picture. The mathematical formalism can be found in textbooks [13], therefore, it will not be presented in detail here.

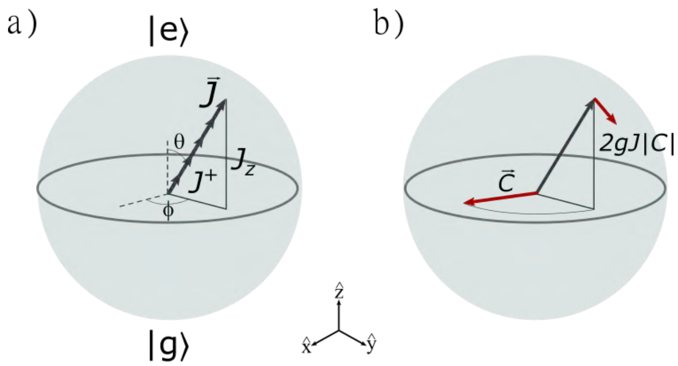

FIGURE 1.3: Representation of an ensemble of many atoms in the collective Bloch sphere. a) The collective Bloch vector, $\vec{J}$, of a system composed of many two-level atoms. Here, J_z represents the population inversion of the state, ϕ denotes the relative phase between the $|g\rangle$ and $|e\rangle$ components, and J^+ represents the atomic coherence. b) Cavity field $\vec{C}$ generated by the atoms and the Bloch vector rotation resulting from that field. C is expressed in units of the amplitude of a single photon.

A single atom can be described as a two-level system, the state of which is represented by a vector on a Bloch sphere of radius $1/2$. If the atom is in the ground state $|g\rangle$, the vector points to the south pole of the sphere. If it is in the excited state $|e\rangle$, the vector points to the north pole. When the atom is in a mixed state, the vector will point somewhere between the two poles, with superposition states lying on the sphere's surface and statistical mixtures inside the sphere. When considering an ensemble of atoms, it is necessary to introduce a collective Bloch vector, $\vec{J}$, which is the sum of the individual Bloch vectors of all atoms.

As is commonly done, $\vec{J}$ can be described in terms of its projections. The J_z component represents its vertical projection, with a value of $N/2$ when at the north pole, $-N/2$ when at the south pole, and zero when in the equatorial plane. The other projections are shown in Figure 1.3 a) and are defined as

$$J_x = J \sin\theta \cos\phi, \tag{1.1}$$

$$J_y = J \sin\theta \sin\phi, \tag{1.2}$$

$$J^+ = J_x + iJ_y. \tag{1.3}$$

We tune the cavity's fundamental mode, TEM00, to be perfectly resonant with the atomic transition. The field of this mode is described by the vector $\vec{C}$, which originates from the center of the collective Bloch sphere. The phase of each atom's Bloch vector is defined relative to the phase of an imagined laser that is perfectly on resonance with the atomic transition and, consequently, to the cavity mode TEM00.

Now, considering the case where $\vec{C}$ is generated by the atoms themselves, it lies in the equatorial plane of the Bloch sphere, as it remains resonant with the atomic transition. Due to this field, the Bloch vector rotates about $\vec{C}$ at a frequency of $2g|\vec{C}|$, as illustrated in Figure 1.3 b).

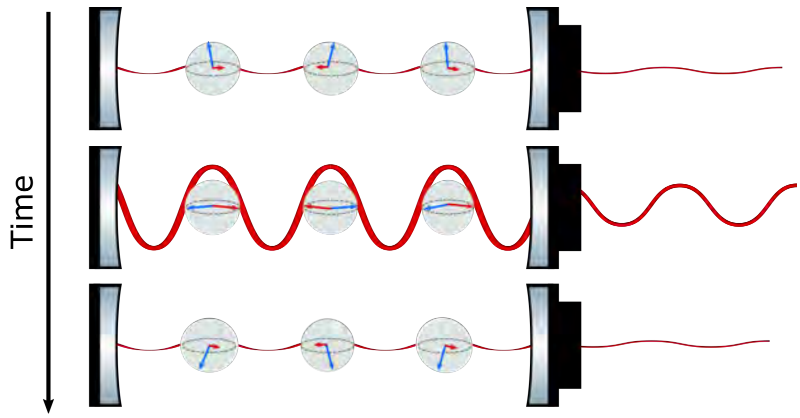

FIGURE 1.4: Representation of a superradiant pulse mechanism using the Bloch sphere picture. Blue arrow represents the Bloch vector and the red arrow represents the cavity field vector.

Consider N atoms in the upper level placed inside the cavity. Due to vacuum fluctuations, one of the atoms begins to decay, generating a resonant field in the cavity. This field then induces emission in the other atoms with just the correct phase for all emitted fields to constructively add up, further amplifying the cavity field. As a result, the Bloch vector rotation is enhanced by a factor of N, because each atom experiences radiation emitted by all the others. In general, when atoms interact with a field that they collectively generate, their interaction rate increases because each atom experiences radiation emitted by all the others. As the atoms states pass through the equator of the Bloch sphere, they transition to the ground state, and the self-generated cavity field extinguishes. This entire process gives rise to a superradiant pulse, which can be detected through cavity transmission. In reality, this is a collective effect because the cavity couples the atoms. Vacuum fluctuations will not start the emission of a single atom, but emission of the collective dipole of all atoms.

This phenomenon has been demonstrated by several research groups. James Thompson's group at JILA demonstrated pulsed superradiance using a rubidium Raman transition [14], as well as superradiance from the millihertz transition of strontium [15]. Meanwhile, Jan Thomsen's group observed the effect on the kilohertz transition of strontium [16, 17], and Andreas Hemmerich's group demonstrated it using calcium on its $379\,\mathrm{Hz}$ transition [18].

1.3 A superradiant clock laser

Despite the exciting achievements mentioned, the pulsed nature of these experiments still limits frequency stability, and the linewidth remains Fourier-limited. To harness this effect for metrological purposes, one promising approach is to achieve steady-state condition leading to continuous-wave emission, which could significantly improve short-term frequency stability.

The device discussed so far is a superradiant laser, whose frequency stability is governed by the radiation field emitted by the ensemble of atoms. This is an important distinction from a standard laser, which derives its frequency stability from the stability of the cavity length.

When using narrow transitions, the gain profile linewidth is significantly narrower than the one of the optical cavity, placing such a device in the so-called bad-cavity regime. In this regime, the lasing frequency is much less sensitive to shifts caused by changes in the optical cavity length, which is one of the main limiting factors of current state-of-the-art optical atomic clocks.

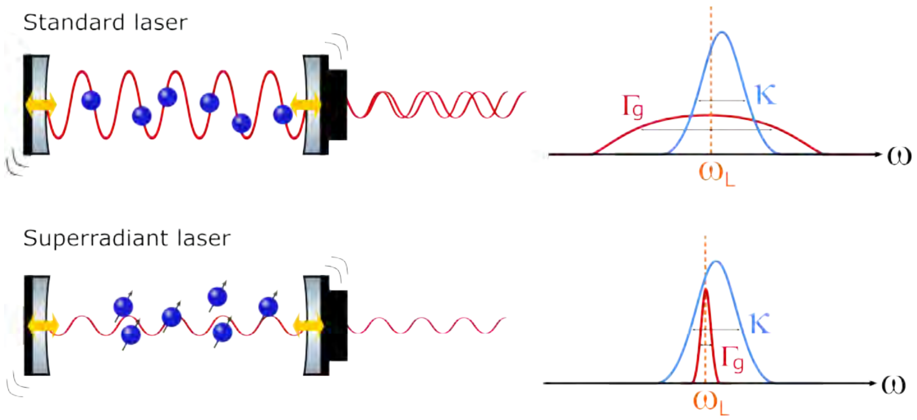

FIGURE 1.5: Comparison between a standard laser and a superradiant laser operating in the bad-cavity regime, where the cavity linewidth κ is larger than the gain medium linewidth Γ_g , in contrast to the standard laser, which operates in the good-cavity regime, $\kappa \gg \Gamma_g$. In a superradiant laser, the laser frequency ω_L is mainly determined by the spin ensemble.

In order to achieve continuous-wave lasing, we revisit the picture presented in the previous section (Figure 1.4) and implement a mechanism to maintain a constant self-generated field in the cavity. One way to achieve this is by continuously replenishing the cavity with new atoms in the upper lasing state while removing those that have already emitted a photon and decayed to the ground state.

This can be realized by introducing a continuous atomic beam that crosses the cavity, ensuring that the atoms have enough time to interact with the cavity field before emission. This process maintains a stable field within the cavity at all times.

In a continuously operating system, the laser linewidth could be reduced to values below the natural linewidth of the transition. These properties make superradiant systems particularly attractive for next-generation optical clocks [19, 20, 21, 22].

1.4 Thesis outline

The remainder of this thesis is organized as follows: Chapter 2 provides a summary of the theoretical foundation underlying the apparatus developed in this work, with a particular focus on key concepts from [21], the paper that inspired the experimental design. Chapter 3 details the design and upgrades made to the experimental apparatus. Chapter 4 presents the characterization of the updated system, including measurements of the new cavity linewidth and the observation of strong coupling between atoms and the cavity mode. Chapter 5 describes the method used for real-time optimization of ground- and excited-state atoms coupled to the optical cavity. Chapter 6 discusses the challenges encountered when applying standard optical cooling techniques and the solutions implemented to address these issues. Chapter 7 highlights the first major experimental results, including significant light amplification from atoms in the upper lasing state coupled to the cavity. Chapter 8 presents the initial observations of collective emission in the system, specifically in the form of optical pulses. Finally, Chapter 9 concludes this work and outlines potential future directions for advancing this research.

Chapter 2

A hot beam superradiant laser

Experimental efforts have been made to study the phenomenon of superradiance [10, 15, 17, 23]. In recent years, there has been a push towards achieving the continuous superradiant regime [24, 25]. However, it has shown to be technically challenging as a result of the reliance on cold atom systems. In 2020, a new proposal introduced a significantly simpler approach: a superradiant laser based on a hot atomic beam traversing an optical cavity [21]. This study is the fundamental basis for the apparatus presented in this thesis.

The proposed system consists of a dense atomic beam that travels through an optical cavity. It is assumed that all atoms have a uniform velocity along the cavity axis (z-axis). In steady state, the mean number of intracavity atoms is given by $N \equiv \Phi\tau$, where Φ is the number of atoms that transit the cavity mode per unit time, and τ is the transit time.

The atoms are treated as dipoles and pumped into a metastable state before entering the cavity mode. The cavity resonance frequency ω_c is assumed to be close to the atomic transition frequency ω_a. The coupling between the atomic dipoles and the cavity is described by the Tavis-Cummings Hamiltonian

$$\hat{H}(t) = \frac{\hbar g}{2} \sum_j \eta \left[\mathbf{x}_j(t)\right] (\hat{\sigma}_j^+ \hat{a} + \hat{a}_\dagger \hat{\sigma}_j^-). \tag{2.1}$$

The summation runs over all the atoms in the beam, $\eta\left[\mathbf{x}_j(t)\right]$ represents the cavity mode function evaluated at the position $\mathbf{x}_j(t)$ of atom j at time t. Here, g denotes the Rabi vacuum frequency at a cavity antinode. The dipole raising and lowering operators are defined as $\hat{\sigma}_j^+ = (\hat{\sigma}_j^-)^\dagger = |e\rangle_j \langle g|_j$, where $|g\rangle$ and $|e\rangle$ represent the atomic ground and excited states, respectively. The photon annihilation and creation operators for the cavity field mode are denoted by $\hat{a}$ and $\hat{a}^\dagger$.

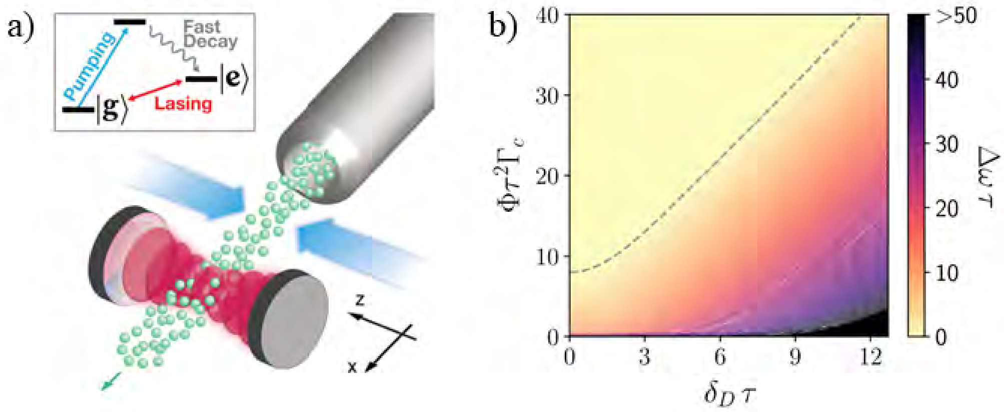

FIGURE 2.1: (a) Proposed architecture of the hot-beam superradiant laser. An effusive oven produces an atomic beam. The atoms are prepared in the excited state of the lasing transition by optical pumping lasers (blue arrows) before entering the cavity. The inset illustrates the minimal atomic structure required for operation. Lasing (red) occurs on the long-lived $|g\rangle \leftrightarrow |e\rangle$ transition. (b) Laser linewidth in units of the transit time broadening $1/\tau$, as a function of the Doppler width $\delta_D\tau$ and $\Phi\tau^2\Gamma_c$ determined by mean-field calculations. The black dashed line represents the phase transition threshold for achieving steady-state superradiance. Figures reproduced from [21]

The cavity photon loss rate is given by κ. The bad-cavity regime occurs when κ is significantly larger than the transit time broadening $1/\tau$, the collective coupling strength $\sqrt{N}g$, and the Doppler width $\delta_D = k\Delta v_z$, where $k = 2\pi/\lambda$, λ is the wavelength of the atomic transition, and Δv_z represents the velocity spread of a single atom along the cavity axis.

In this regime, the collective atomic dipole governs the behavior of the light field. New atomic dipoles entering the cavity become synchronized with the existing collective dipole because of the atom-cavity interaction. The collective linewidth $N\Gamma_c$, which is the rate at which an atom spontaneously emits into the cavity in the presence of another atom, is defined as $N\Gamma_c$, with $\Gamma_c = \mathcal{C}\Gamma$, where $\mathcal{C} = g^2/\kappa\Gamma$ is the cavity cooperativity parameter and Γ is the spontaneous emission rate in free space.

An interesting feature of this scheme is that even though it is based on a hot atomic beam, the broadening mechanisms vanish when $N\Gamma_c >> \delta_D, 1/\tau$. The resulting laser linewidth $\Delta\omega$ is then defined by two parameters: δ_D and Φ. The condition for superradiance emission is obtained when $\Phi\tau^2\Gamma_c > 8$. Until this condition is met, no superradiance is observed even for absense of Doppler broadening $\delta_D\tau << 1$. This happens because the unsynchronized atoms are introduced into the cavity too quickly for the collective dipole to be stabilized.

In this study, it is also shown that the minimum achievable laser linewidth is Γ_c, which is much smaller than the dominant broadening in the system, the transit-time broadening. The narrow linewidth of superradiant emission occurs when the atoms fly through the cavity moving less than $\lambda/2$ along the cavity axis during τ. In addition, the optical phase is stored in the collective dipole for much longer than the time that an individual atom spends in the cavity.

As mentioned previously, the main feature of superradiant emission is the enhanced emission rate, which scales as N^2. For $\delta_D\tau \sim 0.2\pi$ and $\Phi\tau^2\Gamma_c = 2\pi^2$, the maximum power is found numerically to reach a value of $0.7\hbar\omega\Phi$, where ω is the center frequency of the output field. This corresponds to each atom emitting on average 0.7 photons into the cavity mode. This makes superradiance particularly useful when using narrow transitions, where the emission rates are typically on the second time scale.

Additionally, the design suppresses environmental noise effects, such as vibrations or thermal drifts, which typically affect cavity-stabilized lasers [26]. Since phase information is primarily stored in the atomic medium rather than in the cavity resonance, the cavity pulling factor is greatly suppressed. This factor is defined as $\mathcal{P} = (\omega - \omega_a)/(\omega_c - \omega_a)$, which describes the fractional change in laser frequency when the cavity resonance changes with respect to the atomic transition. Analytical analysis shows that $\mathcal{P} \propto 1/\kappa\tau$. Consequently, the superradiant laser maintains narrow linewidths and significant output power even in nonlaboratory settings, making it particularly promising for field applications.

In order to build such a superradiant laser, the following conditions must be fulfilled:

$$\Phi\tau^2\Gamma_c > 8, \tag{2.2}$$

$$\delta_D\tau > \pi. \tag{2.3}$$

These requirements are achieved through an interplay between the atomic beam flux, determined by the oven design, and the cavity parameters. The cavity finesse must be carefully chosen to minimize cavity pulling while maintaining a reasonable output power. To reduce Doppler broadening along the cavity axis, laser cooling is necessary. Importantly, optical pumping must be performed outside the cavity to avoid parasitic heating.

Chapter 3

Experimental Apparatus

In this chapter, the chosen atomic element, strontium-88 (^{88}Sr), is introduced. The working principles of the experimental apparatus are then described, followed by a discussion of the upgrades implemented. Due to technical challenges and limitations encountered with the initial version of the setup, two critical components were modified: the oven and the optical cavity. Additionally, new laser and optical systems were developed to provide the necessary optical power for preparing a high-flux atomic source. This chapter presents a detailed discussion of these components and their improvements.

3.1 The toolkit: strontium

Strontium has four naturally occurring isotopes, of which three are bosonic — ^{84}Sr, ^{86}Sr, and ^{88}Sr — while ^{87}Sr is fermionic. Bosonic isotopes have zero nuclear spin, $I = 0$, leading to the absence of a hyperfine structure. In this work, the isotope ^{88}Sr is used due to its natural abundance of 82.58%.

Neutral Sr atoms contain 38 electrons, of which two are valence electrons. The electronic states of strontium can be classified as singlet or triplet, depending on the spin symmetry of the electrons. The ground state of bosonic isotopes is the singlet state $^1S_0$, which has zero magnetic dipole moment, $J = 0$, which makes it insensitive to magnetic fields.

The transition from the ground state to $^1P_1$ has a linewidth of $\gamma/2\pi = 32\,\text{MHz}$, making it ideal for laser cooling atoms that are initially very hot . In contrast, the transition from the ground state to the triplet state $^3P_1$ is forbidden by dipole selection rules, but an admixture of the $^1P_1$ state allows it, resulting in a much narrower linewidth of $\gamma/2\pi = 7.5$ kHz, which is the lasing transition of interest in this work.

Other triplet states are forbidden by the total angular momentum, the quantum number J, and the selection rules. However, for ^{87}Sr, the nuclear magnetic moment makes the $^1S_0 -^3 P_0$ transition weakly allowed, with a linewidth of $1\,\mathrm{mHz}$. In contrast, for ^{88}Sr, this same transition can be opened by applying a strong external magnetic field. This transition in both isotopes is used as a clock transition in state-of-the-art optical lattice clocks [5].

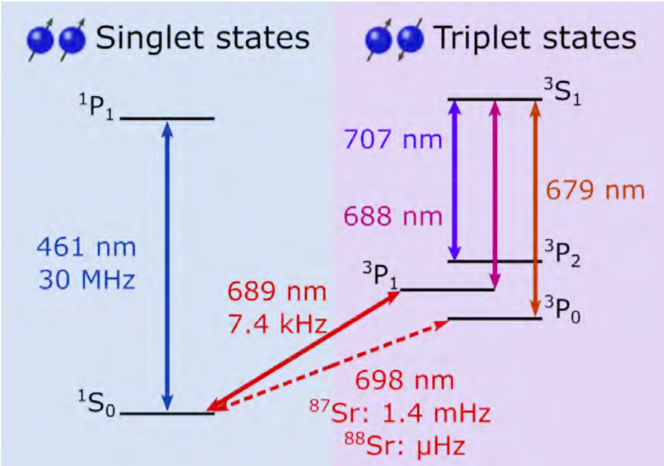

FIGURE 3.1: Simplified energy level diagram of strontium, including the transitions used in the experimental apparatus. The clock transition is shown as a dashed red line, along with the corresponding linewidths for the isotopes ^{87}Sr and ^{88}Sr.

3.2 Design overview

Figure 3.2 illustrates the working principle of the apparatus. An oven emits an atomic beam of ^{88}Sr atoms through a nozzle. Beyond the heating shields (not shown in the figure), a pre-collimation beam at $461\,\mathrm{nm}$ is constantly on, helping to shift the velocity distribution along the cavity axis (z-axis), and allowing more atoms to interact with the subsequent collimation beam, which also addresses the $^1S_0$-$^1P_1$ transition and alternates in time with the velocity-selection beam, pushes the atoms toward zero velocity along the z-axis.

When the collimation beam is off, the velocity selection beam, composed of a mixture of $689\,\mathrm{nm}$ and $688\,\mathrm{nm}$ light, interacts with the atoms in an x-velocity range around $1.5\,\mathrm{m\,s^{-1}}$. From $^1S_0$, the atoms are pumped to $^3P_1$ with the laser at $689\,\mathrm{nm}$, and then to $^3S_1$ with the laser beam at $688\,\mathrm{nm}$. From there, the atoms will decay into all the ^3P states. The $^3P_{0,2}$ states act as storage states, ensuring that the atoms remain within a narrow velocity range for further manipulation. Atoms in $^3P_1$ are again pumped to $^3S_1$ or decay to the ground state. The cooling mechanism employed in the apparatus is discussed in detail in Chapter 6.

FIGURE 3.2: Working principle of the apparatus. Cooling beams along the y-direction are not shown in this representation. Figure adapted from a design by S.A. Schaffer [27].

In the y-direction, also not shown in the figure, there is a pair of counter-propagating $461\,\mathrm{nm}$ beams directly above the heat shields that remain constantly on. Further upwards, at the same height as the second collimation and velocity-selection beam, there are two additional pairs of counter-propagating beams, which are time-synchronized with the collimation beam. These y-axis beams serve to compress the atomic cloud, increasing the number of atoms funneled into the cavity volume.

Afterwards, atoms in the ground state are accelerated along x, and thereby Doppler shifted out of resonance, by a resonant $461\,\mathrm{nm}$ cleaning beam. Just before the atoms enter the cavity mode, they interact with an excitation beam, composed of $679\,\mathrm{nm}$, $707\,\mathrm{nm}$, and $688\,\mathrm{nm}$ light, which pumps the atoms to the upper lasing state, $^3P_1, m_j = 0$. The excitation scheme will be described in the following subsection.

Once the atoms enter the cavity mode, they can be probed by $689\,\mathrm{nm}$ light, which is coupled to the fundamental TEM_{00} mode of the cavity. The transmitted light is then detected, either through heterodyne detection or by using an avalanche photodetector (APD).

3.2.1 The excitation scheme

The magnetic field in the cavity region is controlled using three pairs of magnetic coils arranged in a Helmholtz configuration. Each pair independently adjusts the magnetic field along one of the three axes of the apparatus (x, y, and z). These coils are necessary to cancel external magnetic fields, such as those generated by the ion pump, and to define the quantization axis in the cavity region, which is set along the x-axis. The magnetic field in the cavity is set to $3.2\,\mathrm{G}$, leading to a Zeeman splitting of $3.2\,\mathrm{MHz}$ between the m_j states of the $^3P_1$ level. The $m_j = 0$ sublevel is the target state, as it remains insensitive to first-order magnetic field fluctuations, thereby ensuring enhanced stability and coherence in the output field.

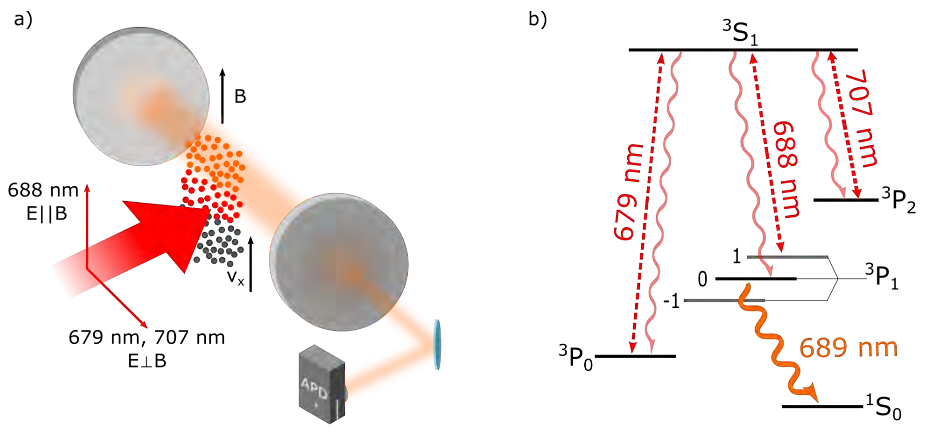

FIGURE 3.3: a) Geometry of the excitation step. As the atoms travel upward along the x-direction with velocity v_x, they interact with the excitation beam below the cavity volume. b) Energy level scheme of ^{88}Sr, illustrating the repump transitions (dotted arrows), spontaneous decay channels (red wavy arrows), and lasing transition (orange wavy arrow) at $689\,\mathrm{nm}$.

The excitation beam is responsible for incoherently populating the target state. It consists of three repump lasers (dotted arrows in Figure 3.3 b)), which co-propagate and are oriented perpendicular to the cavity axis to prevent imparting velocity to the atoms along this axis. The $688\,\mathrm{nm}$ light is polarized parallel to the magnetic field to drive the $\Delta m_j = 0$ transitions between ${}^3P_1, m_j = \pm 1$ and ${}^3S_1, m_j = \pm 1$. Meanwhile, the $679\,\mathrm{nm}$ and $707\,\mathrm{nm}$ beams are polarized perpendicular to the magnetic field and serve to repump atoms that have decayed into the ${}^3P_0$ and ${}^3P_2$ states. This process ensures that these atoms return to the ${}^3S_1$ state, providing another opportunity for decay to the ${}^3P_1, m_j = 0$ level. Since the atoms reach the target state through spontaneous decay, the phase of the repump lasers is not imprinted onto the lasing light.

As the atoms travel upward and enter the cavity volume, they are expected to undergo superradiant emission at $689\,\mathrm{nm}$ and decay to the ground state ${}^1S_0$, provided that all necessary conditions are met.

3.3 The vacuum system

Figure 3.4 a) shows the design of the vacuum system, which uses a CF100 4-way cross as its central element. The bottom section houses the oven and atomic source. Above it follows a region with four windows, which allow optical access to the atomic beam. Just above it is the cavity section, which rests on the acoustic isolation stack. Each of these sections will be described in detail in the following sections.

3.3.1 Dissassembling

The system had been operational for two years, during which the oven was kept at temperatures between $773.15\,\mathrm{K}$ and $873.15\,\mathrm{K}$. Over time, a layer of strontium accumulated on the interior surfaces of the vacuum chamber, including partial coverage of the vacuum windows because of a direct line of sight from the oven nozzle. Additionally, the oven nozzle was found to be partially clogged at its center, significantly reducing the atomic flux in the cavity region, below the required levels for the currently used cavity. Given these issues, it was decided to replace the critical components, namely the cavity and the oven, while retaining the rest of the setup.

The replacement process begins by partially disassembling the optical systems around the vacuum chamber to allow for direct access. This includes removing the upper breadboard to allow removal of the upper flange that holds the acoustic isolation stack. During this time, the oven temperature is slowly increased to room temperature, followed by the disconnect of all control electronics. The ion pump is then turned off and

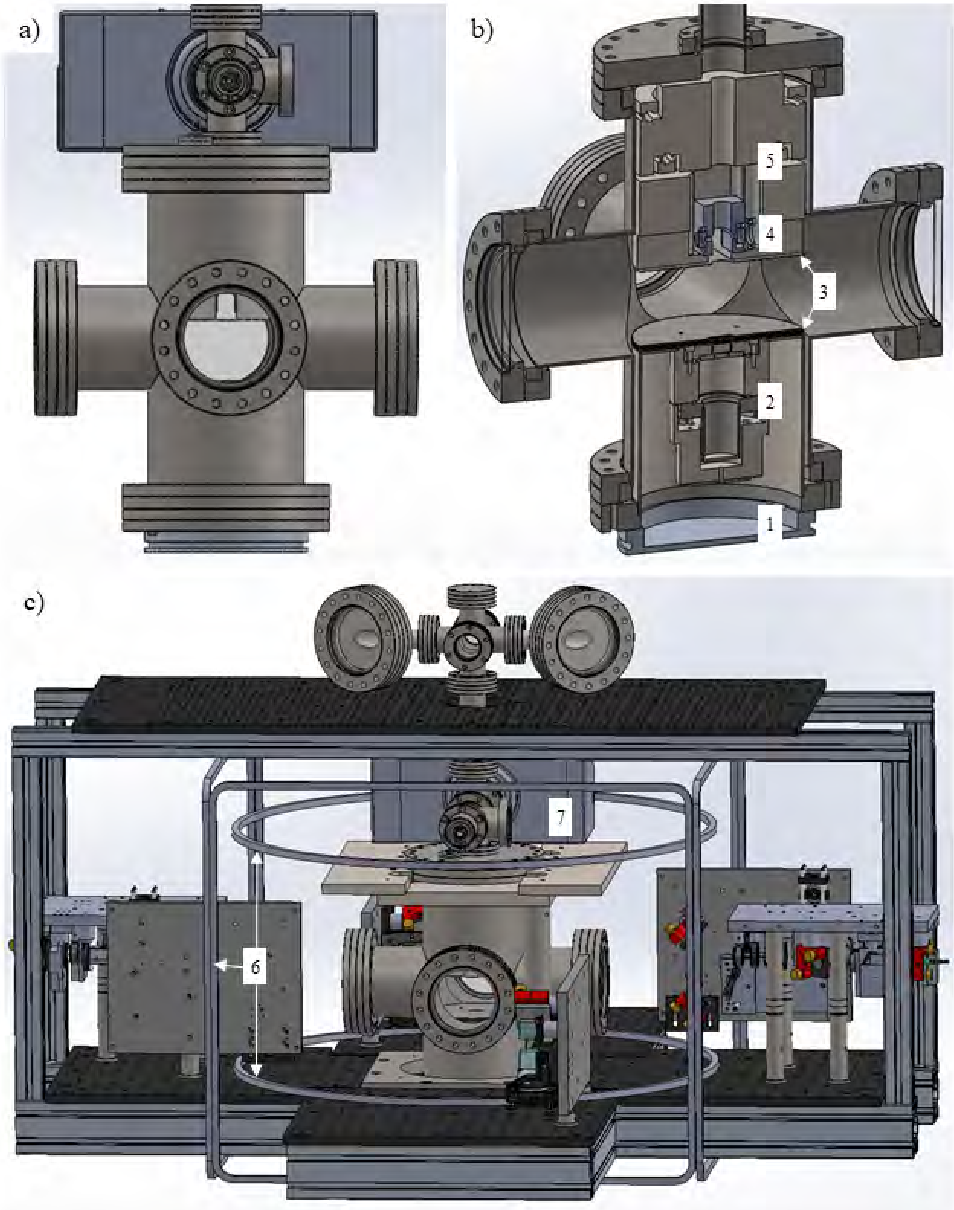

FIGURE 3.4: a) Vacuum chamber design external view. b) Transverse cross-section showing the internal components: 1) cooling plate; 2) oven and reservoir; 3) heat shields; 4) cavity; 5) acoustic isolation stack. c) The vacuum system and supporting framework include some optical system components, such as for optical cooling, cavity lock and cavity output detection. Additional elements: 6) magnetic field coils; 7) ion pump. The additional windows on the top breadboard are not relevant to the scope of this thesis.

the vacuum is broken. Because of the reactive nature of strontium with oxygen, this step is conducted with caution to avoid rapid oxidation. Within a few minutes, a white layer of strontium oxide (SrO) forms on the internal surfaces of the chamber, as shown in Figure 3.5. Once SrO formation stops, the window seals are removed by unscrewing them.

The acoustic isolation stack consists of two aluminum blocks. The upper block weighs 6.1 kg, while the lower block, where the cavity is seated, weighs 6.8 kg. To lift this entire assembly, aluminum profiles are placed between the upper flange and the cross that connects to the ion pump (which has already been removed). The entire section is lifted using a forklift and placed on a support on the optical table.

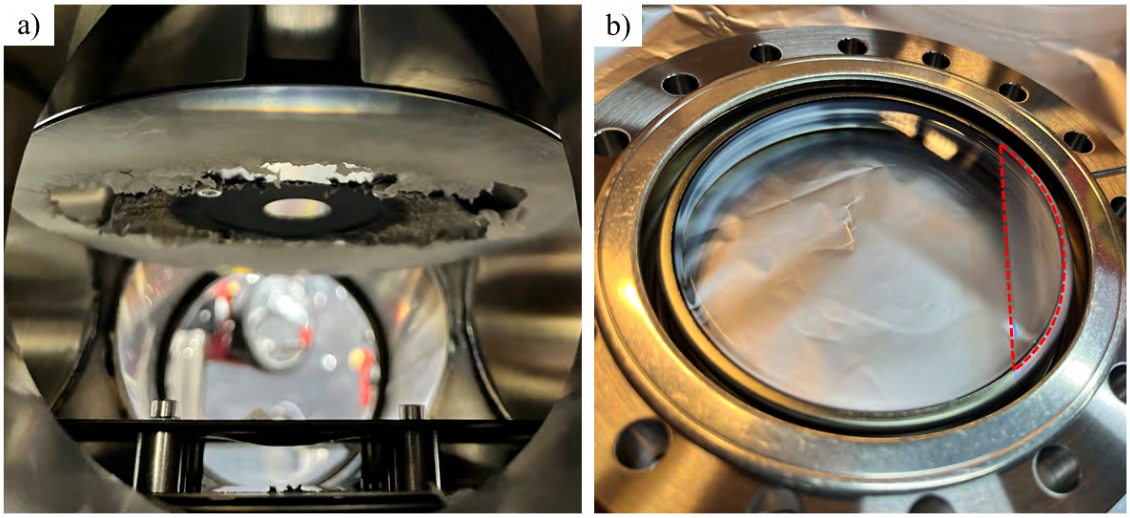

FIGURE 3.5: a) SrO formation on the cavity heat shield. b) The red dashed region indicates the strontium coating on one of the vacuum chamber windows.

The framework, including the vacuum chamber, in then forklifted sideways off the optical table, to allow sufficient access for the removal of the oven from below. The procedure is followed by removing the cooling plate and removing the insulating glass wool from the space between cooling plate and oven reservoir. The thermocouples that are used to measure the oven's temperature are detached and set aside for use in the new oven version. All other cables are disconnected, and the oven assembly is unscrewed and removed from the vacuum chamber.

All parts of the vacuum chamber intended for reuse, excluding the windows, were thoroughly cleaned with ethanol until no visible SrO or other residues remained. New copper, nickel and silver gaskets are prepared and cleaned in advance for reassemblement. The disconnected electronics, including oven temperature control, monitoring systems, and cavity locking components, are carefully labeled after disconnection to ensure easy identification and future use.

3.4 Optical cavity

The optical cavity is one of the key components of the setup. The initial target is a cavity with a linewidth ten times narrower than the previous one, which would proportionally lower the atomic threshold as needed, thereby making the requirements for the final goal more attainable. In the previous version, the apparatus operated in the deep bad-cavity regime, with a cavity linewidth of $2\,\pi \times 55\,\mathrm{MHz}$ and finesse $\mathcal{F}$ of ~ 100. In the new configuration, the system operates in the cross-over regime, where the cavity linewidth is comparable to the atomic transit time, on the order of a few MHz.

The new cavity keeps the design of the old one, but the reflectivity of both mirrors is increased. This decision is influenced by the availability of a cavity spacer identical to the original one and an acoustic isolation stack tailored for it.

The optical cavity spacer is machined from Ohara Clearceram CCZ-HS, a material known for its ultralow thermal expansion and good machinability. The cavity is mounted on an acoustic isolation stack, which is suspended from a DN160 CF flange within the vacuum system. The isolation stack is designed to attenuate and prevent environmental mechanical vibrations from being transmitted to the optical cavity. It consists of two aluminium blocks of different sizes and masses, mounted on a ring with $8\,\mathrm{mm}$ diameter Viton balls for damping. The stack is supported by three M6 stainless steel threaded rods. A heat shield, made of $0.5\,\mathrm{mm}$ thick stainless steel, is mounted at the bottom of the isolation stack using wavy stainless steel washers to provide an offset to the isolation stack while keeping thermal conductance low. It minimizes radiation from the oven and has a hole diameter of $17\,\mathrm{mm}$ to allow the atomic beam to pass through to the cavity region. The full design can be seen in Figure 3.6.

The optical cavity consists of two concave mirrors, each with a radius of curvature R = $100\,\mathrm{mm}$, positioned opposite each other and separated by a distance L = $65.65\,\mathrm{mm}$.

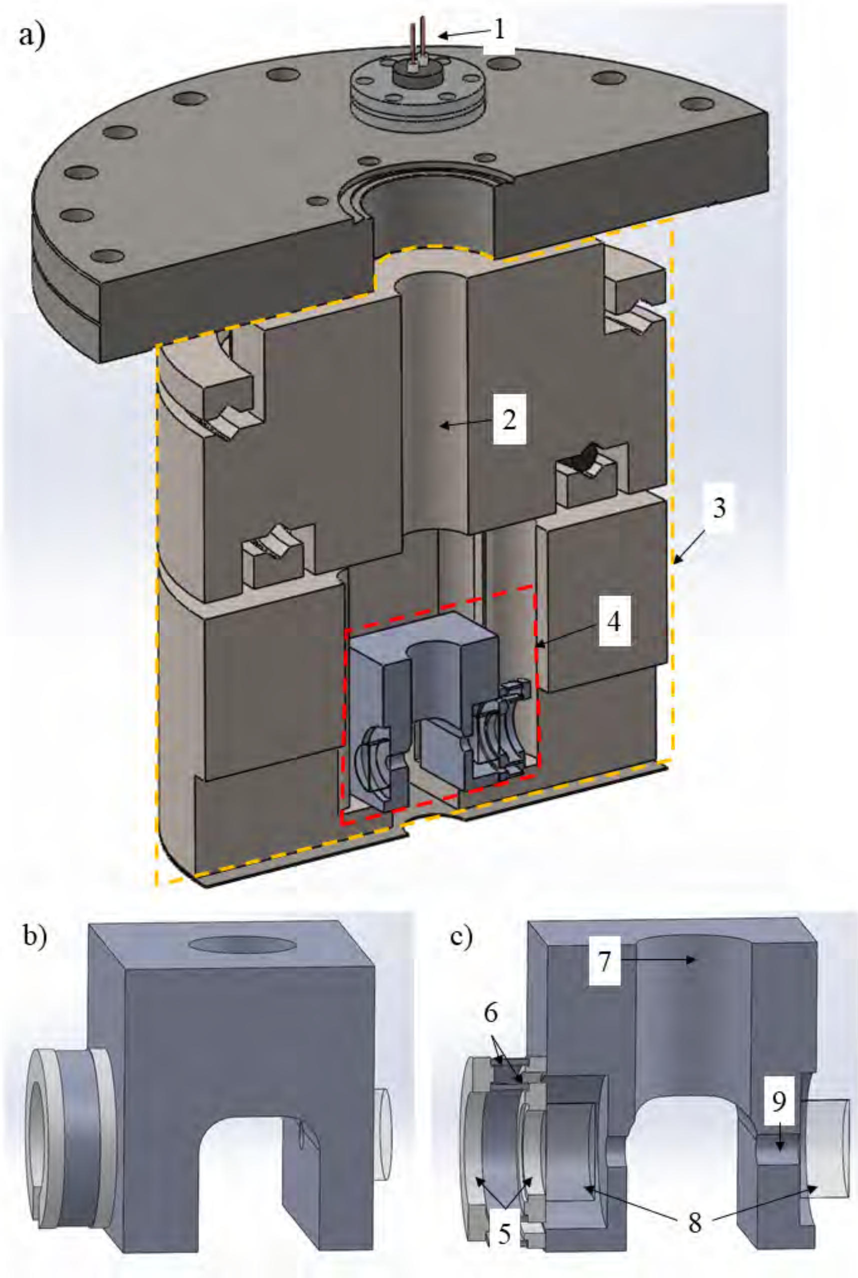

FIGURE 3.6: Details of the cavity and acoustic isolation system design. a) Elements: 1) Feedthrough for piezo control; 2) Clearance for vacuum pumping; 3) Acoustic isolation stack; 4) Optical cavity. b) Optical cavity design featuring the piezo stack and cavity spacer. c) Detailed view of the optical cavity: 5) Marcor rings; 6) Piezo elements; 7) Clearance for the atomic beam path and vacuum pumping; 8) Mirrors; 9) Clearance for the cavity optical axis access.

In this configuration, to determine if our cavity meets the stability criteria for a linear resonator, it is necessary to introduce the g-parameter for the cavity mirrors [28]:

$$g_i = 1 - \frac{L}{R_i}, i = 1, 2 \tag{3.1}$$

The inequality then defines the stability condition:

$$0 < g_1 g_2 < 1 \tag{3.2}$$

This condition ensures that an optical ray remains confined within the resonator and parallel to the optical axis after multiple reflections. Figure 3.7 illustrates this concept and indicates where our cavity lies within this stability condition.

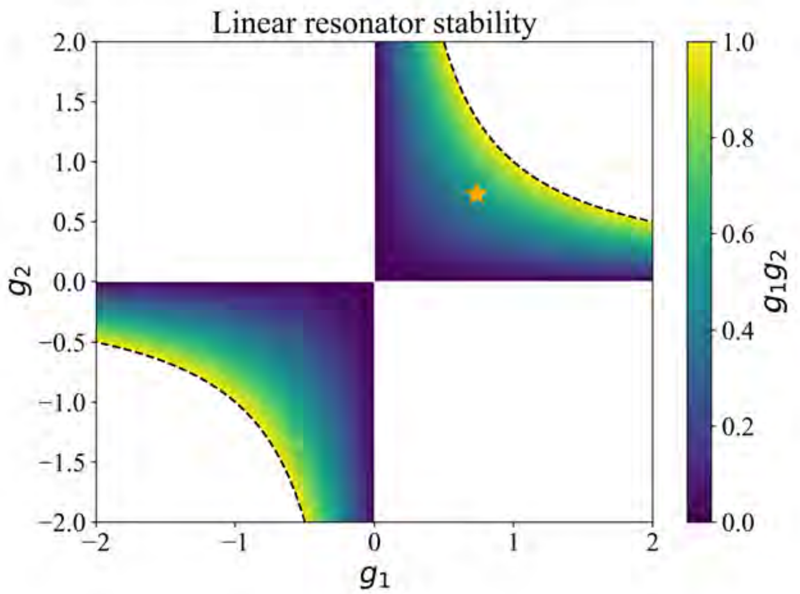

FIGURE 3.7: Linear resonator stability condition. For our cavity parameters we have $g_1 = g_2 = 0.7335$.

The cavity mirrors are bought from FiveNine Optics, with the following specifications: a diameter of $12.7\,\mathrm{mm}$, a thickness of $6.35\,\mathrm{mm}$, and a $100\,\mathrm{mm}$ radius of curvature. The mirrors are fabricated from super-polished fused silica substrates with a wedge angle of less than $15'$. The coating specifications are as follows: for one of the surfaces, a partial reflectivity (PR) coating optimized for the $660\,\mathrm{nm}$ to $710\,\mathrm{nm}$ range with a power transmission of T = $0.3\% \pm 0.025\%$; for the other surface, an anti-reflective (AR) coating in the $660\,\mathrm{nm}$ to $710\,\mathrm{nm}$ range with power reflectivity R $< 0.15\%$. With these specifications, the target is to achieve a finesse $\mathcal{F} = 1000$. The following section outlines the step-by-step assembly procedure for this cavity.

3.4.1 Assembly

The assembly begins with the setup of the piezoelectric stack, which controls the cavity length since it must remain actively stabilized to maintain resonance with the atomic transition. The piezo stack consists of two concentric piezoelectric actuators, aligned and placed together using rings made of Corning Macor machineable glass-ceramic (Macor). This configuration enables tuning the cavity to resonance with the desired Gaussian TEM mode, while also providing fine control over both slow and fast drifts in the cavity length.

All components of the piezoelectric stack are assembled using MasterBond EP21TCHT-1, a two-component adhesive with a 10:6 mix ratio by weight. This adhesive is selected for its ability to cure at ambient temperatures within 24 hours, simplifying the assembly process and preventing displacement due to changes in viscosity or temperature fluctuations. Additionally, it is electrically insulating, resistant to high temperatures, and suitable for high-vacuum applications, according to the manufacturer's specifications.

Each piezo and Macor ring is cleaned with ethanol, along with the workspace, to ensure a contaminant-free environment. The piezos and Macor rings are then assembled, with adhesive applied at three distinct points along the junctions of the surfaces. This method ensures that no adhesive layer forms between the surfaces, which could lead to uneven heights in the overall stack.

Once all components are glued together, the assembly is secured using a small clamp and a Viton ring of the same diameter as the outer piezo, to ensure everything is held in place, as shown in Figure 3.8 a). The assembly is left to cure for over 24 hours at room temperature to ensure complete curing.

It is necessary to solder copper wires to the piezos, which are also cleaned with ethanol. A vacuum-compatible solder (Allectra) is used, along with wires of $0.12\,\mathrm{mm}$ diameter. This task is performed by Johan Mozes, a member of the electronic workshop at the UvA.

Afterwards, a viton ring, matching the diameter of the piezo stack, is placed beneath it, and the assembly is held in position using two small mirror mount clamps placed on opposite sides. The wires remain free from contact with the holder surface, ensuring there is no risk of breakage.

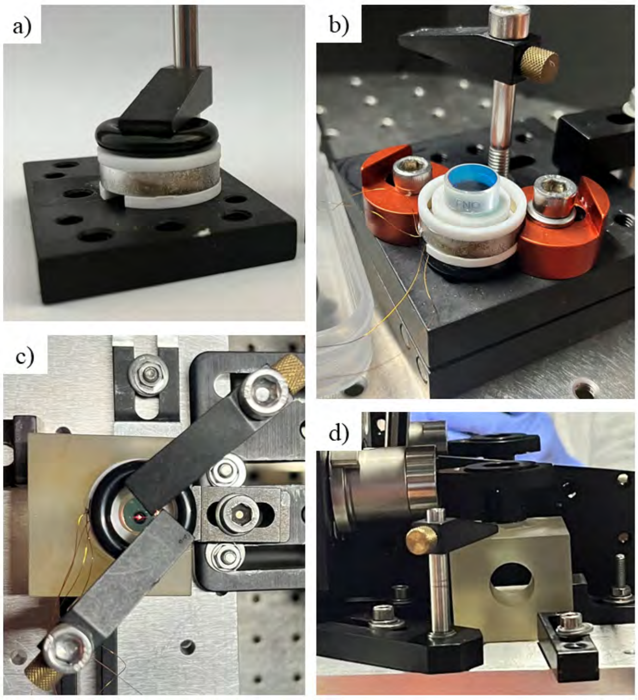

FIGURE 3.8: a) Piezo stack during the curing process. b) Preparing to glue a mirror onto the piezo stack. c) Piezo stack with a mirror secured to the spacer. d) Alignment of the second mirror with the spacer.

The mirror is aligned concentrically with the piezo stack, and the same adhesive and method are applied to bond them together. A $1/2''$ mirror mount with an internal Viton ring holds the mirror in place, which is clamped from the top to secure the mirror into the piezo stack. The assembly is also left to cure at room temperature for 24 hours.

The next step involves bonding the mirror-piezo stack to the cavity spacer. The optical setup used for its alignment is shown in Figure 3.9 a) consisting of a $689\,\mathrm{nm}$ light source delivered through an optical fiber, a $10\,\mathrm{mm}$ fiber collimator (1), iris (2,5), a lens of focal length f = $100\,\mathrm{mm}$ (3) and mirrors (4,6). The system is first aligned in the horizontal plane to ensure the optical beam remains within the plane and the retro-reflected beam overlaps with the incoming beam path.

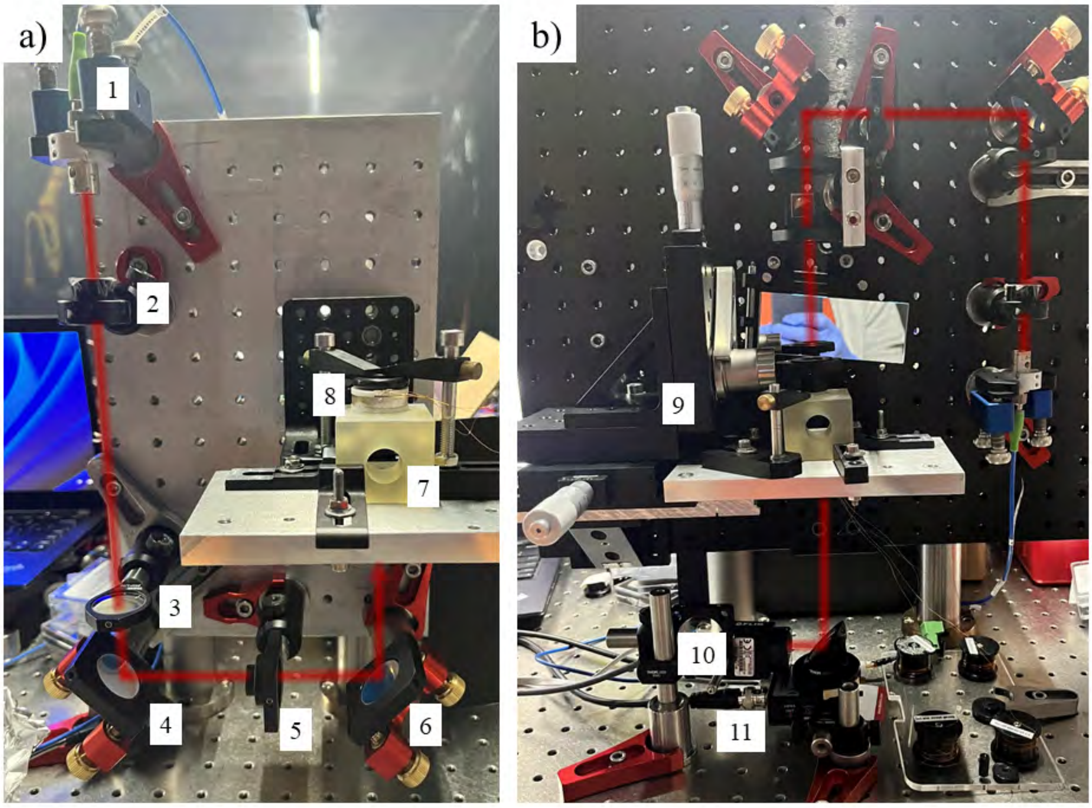

FIGURE 3.9: a) First mirror optical alignment setup consisting of the following elements: 1) Optical fiber delivering the 689 nm light; 2,5) Iris for beam alignment reference; 3) Lens with a focal length f = 100 mm; 4, 6: Mirror mounts for beam alignment; 7) Cavity spacer; 8) Piezo stack with attached mirror. Red arrow to illustrate 689 nm beam path. b) Second mirror optical alignment setup with the added elements: 9) fine adjustment translation mounts; 10) FLIR camera; 11) Photodetector. The red lines illustrate the 689 nm beam path.

Once the horizontal alignment is achieved, the optical setup breadboard is positioned vertically, and a platform is added to secure the cavity using clamps. This approach leverages the gravitational force to assist in aligning the mirror-piezo stack on the cavity spacer. The mirror-piezo stack is now carefully adjusted horizontally until the retro-reflected beam overlaps with the incoming beam. However, it is observed that, to achieve this alignment, the mirror and spacer holes are not concentric. This misalignment may result from either the spacer faces not being perfectly parallel and/or slight variations in the height of the piezo stack. Despite these geometric inconsistencies, the decision is made to bond the mirror-piezo stack to the cavity spacer at the position where the retro-reflected and incoming beams are properly overlapped.

Once this is achieved, the assembly is clamped from above using a Viton ring to hold it in place, as shown in Figure 3.9 a). The adhesive is then applied at the junction between the piezo stack and the cavity spacer while the retro-reflection is monitored.

After the curing process, the more challenging task of aligning and bonding the second mirror is undertaken. This step requires care, as it is crucial to achieving the desired cavity performance. To facilitate this, the optical setup shown in Figure 3.9 a) is modified as shown in b) for better precision in mirror alignment and for monitoring the cavity modes coupled during the process.

For precise alignment, the XYZ translation stage (Thorlabs PT3/M) is used to adjust the mirror in the xy-plane while the one along the z-axis is used to clamp the mirror once the proper alignment is reached. The larger piezo is driven by a voltage generator capable of tuning to and scanning across the cavity resonances. A photodetector (Thorlabs PDA10 and a FLIR camera are placed on the transmission side of the cavity. The photodetector is used to optimize the coupling of light into the cavity, while the camera ensures that the targeted mode, the TEM_{00} mode, is the one being optimized.

Once maximum coupling is achieved by aligning the second mirror using the translation mounts, the mount along the z-axis is utilized to secure the mirror in place. The bonding process is then performed again, ensuring that the mirror remains properly aligned throughout.

During the curing process, the piezo is kept scanning across the TEM_{00} mode and $15\,\mathrm{MHz}$ sidebands are applied to the $689\,\mathrm{nm}$ light using a fiber electro-optic modulator (EOM). The transmitted signal is recorded and analyzed to estimate the finesse of the cavity in air, allowing verification of whether it approaches the target value of 1000.

The recorded signal is presented in Figure 3.10. For analysis, it is fit a sum of three Lorentzian functions, each defined as:

$$f(x) = \frac{A}{\pi}\frac{\Gamma/2}{(x-x_0)^2+(\Gamma/2)^2} \tag{3.3}$$

The full width at half maximum (FWHM), denoted by Γ, is obtained from the fit of the central peak. Given that the frequency separation between the carrier and the sidebands is $15\,\mathrm{MHz}$, the x-axis is converted to a frequency scale, allowing us to extract the linewidth from the fit. Using the designed mirror spacing $L = 65.65\,\mathrm{mm}$ the cavity finesse $\mathcal{F}$ can be estimated. For the air cavity, the measured line width of the cavity is

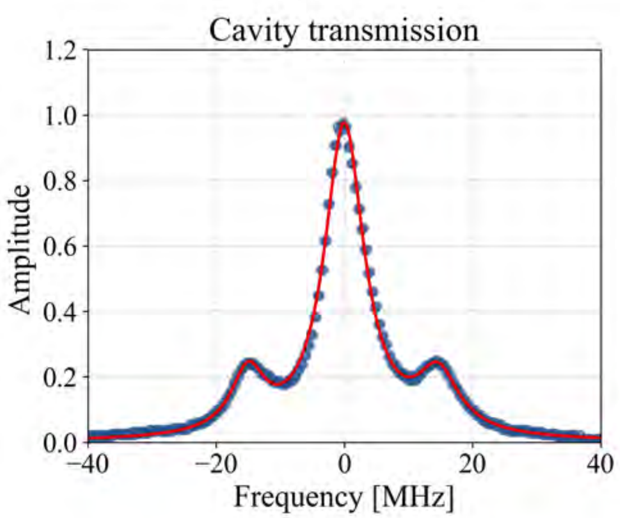

FIGURE 3.10: Cavity transmission of the TEM_{00} mode, with sidebands at 15 MHz.Blue dots represent data points, while the red line corresponds to a fit using three Lorentzian functions.

$\Gamma_c = 7.51\,\mathrm{MHz}$, which results in $\mathcal{F} \sim 750$, which is expected to increase slightly once the cavity is placed under vacuum.

3.4.2 Insertion of cavity into vacuum chamber

Once the cavity is fully assembled, tested and operational, the next step is to insert it into the vacuum chamber. This procedure involves multiple steps to ensure proper installation and alignment within the system. Figure 3.11 a) shows the cavity placed inside one of the aluminum blocks of the isolation stack. The block is thoroughly cleaned with ethanol prior to cavity insertion. The cavity is secured using Viton balls positioned near its corners, ensuring stability. The mirrors are aligned with the side of the block that has clearance for optical coupling.

Afterwards, the block containing the cavity is carefully lifted and attached to the rest of the isolation stack, which has also been cleaned. With the entire assembly resting on a sturdy mount on the optical table, as shown in Figure 3.11 b), the final adjustment of the acoustic isolation stack is performed. Threaded screws are used to connect the blocks, and to ensure proper alignment between them, a calliper is employed to measure the gap distance. Adjustments to the screws are made until uniformity in the gap is achieved throughout the attachment.

The piezo wires are then soldered to the feedthrough using vacuum-compatible solder. This step is to enable the control of the cavity length via a high-voltage driver. Once all connections are finalized and the components are cleaned again, the entire assembly is lifted with a forklift and carefully positioned above the vacuum chamber. A DN160 copper gasket is placed on the top flange of the vacuum chamber's central four-way cross. The alignment of the cavity assembly is verified to ensure that the cavity mirrors are centered with respect to the vacuum chamber windows. Once aligned, the forklift slowly lowers the assembly until the top flange secure rests on the gasket. Afterwards, the forklift and any additional supports are removed.

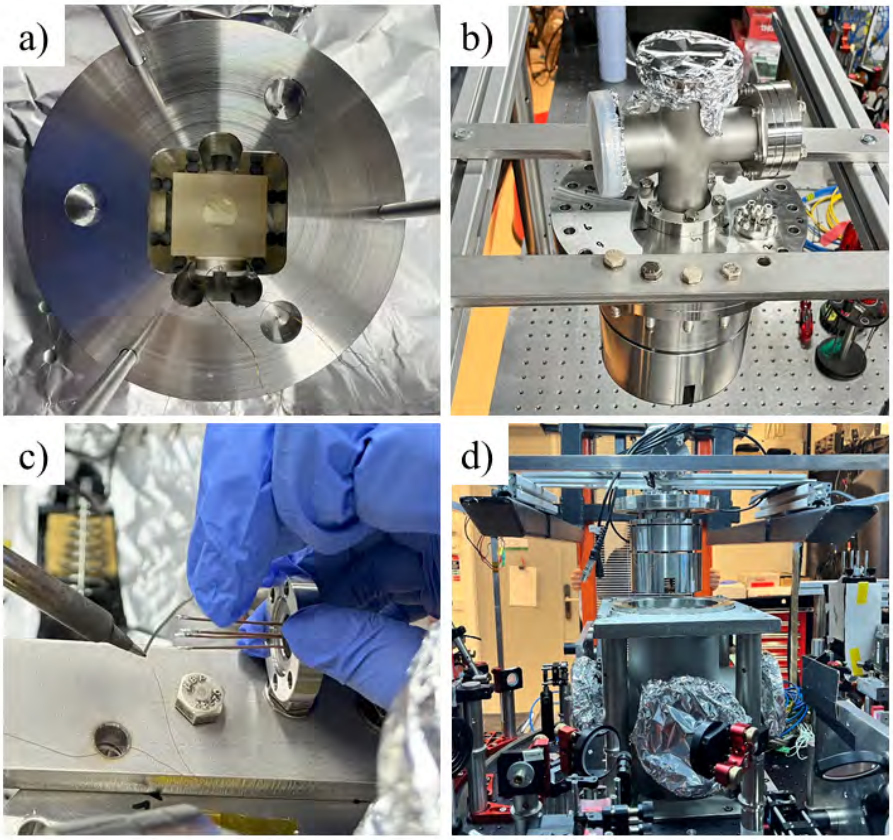

FIGURE 3.11: a) The cavity is inserted into one of the blocks of the isolation stack. b) Fully assembled cavity and isolation stack attached to the top flange of the vacuum chamber. c) Piezo wires being soldered to the feedthrough. d) Placement preparation of the cavity and isolation stack inside the vacuum chamber.

3.5 High flux oven source

In this section, the design of the replacement effusive oven, which produces the atomic beam, will be presented. This oven was designed and constructed in collaboration with Daan Giesen, a design engineer from the Technology Center of UvA.

3.5.1 Design

The oven is constructed from 316L stainless steel, a material chosen for its low carbon content, weldability, high-temperature corrosion resistance, and its proven performance in previous vacuum chamber constructions by the Technology Center engineers at our Institute of Physics. These properties ensure the oven's durability and reliability for high-temperature operations in a vacuum.

The oven is designed to operate at temperatures up to $973.15\,\mathrm{K}$ and produce a collimated beam of strontium atoms. It is divided into two main parts: the reservoir and the nozzle. The nozzle features an array of stainless steel microtubes, each $8\,\mathrm{mm}$ long with an inner diameter of $305\,\mu\mathrm{m}$ and an outer diameter of $414\,\mu\mathrm{m}$. These tubes are arranged in a region with an area of $4.75\,\mathrm{mm}^2$, held in place by a wedge system. On the inner side, a flange is placed against the nozzle region with a clearance region measuring $12 \times 2\,\mathrm{mm}$, sealing the assembly against the strontium reservoir and allowing gas flow through the selected microtubes, known as the active region. This region is designed to maximize the number of atoms passing through the cavity mode volume.

As shown in Figure 3.12 b), the outer top part of the oven, highlighted in blue and marked by number three, features five radiation shields, each made of $0.5\,\mathrm{mm}$ thick sheets of 316L stainless steel and separated by $0.5\,\mathrm{mm}$ gaps using ceramic rings. These shields feature apertures aligned with the nozzle region and are bent at the edges, with a length of $51\,\mathrm{mm}$, to act as a protective lid. This design prevents the atomic beam from having a direct line of sight towards the chamber windows and minimizes the chance of atoms rebounding between the shields and ultimately hitting the windows and producing an unwanted coating. This shielding also helps reduce thermal radiation and maintains temperature stability.

The reservoir is attached to the inner part of the oven assembly, as highlighted by the dashed line in Figure 3.12 b). In addition, a copper plate is affixed to the bottom

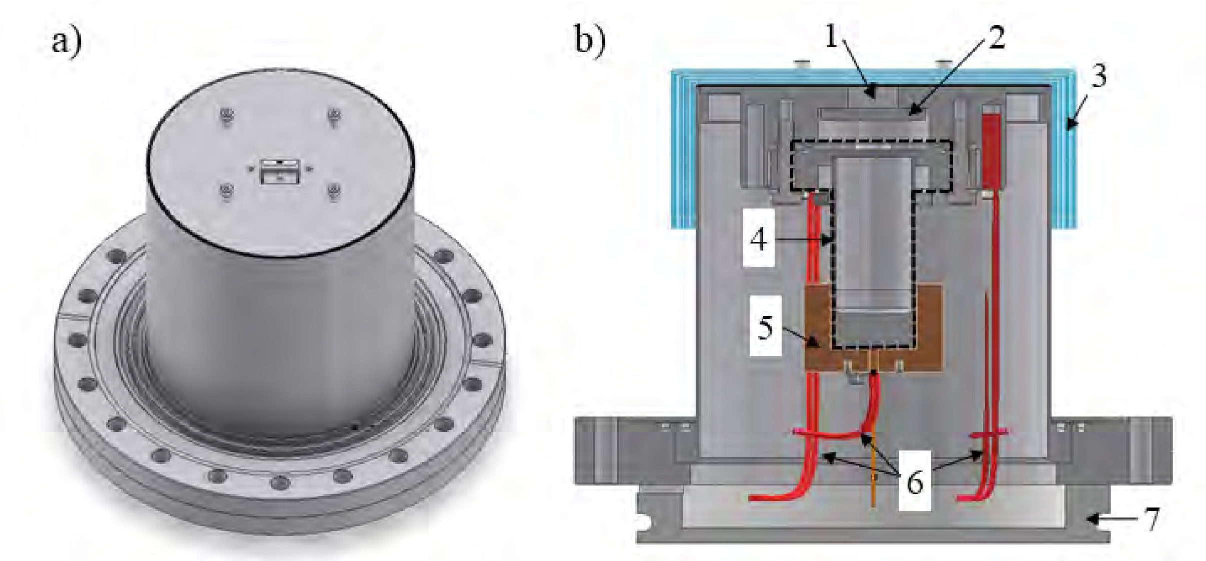

FIGURE 3.12: a) External view of the oven design. b) Transverse cross-section showing oven components: 1) Nozzle with microtubes array; 2) Nozzle cap defining the active region; 3) Heat shields; 4) Dashed line indicating the reservoir sections; 5) Copper heating plate; 6) Heating elements; 7) Cooling plate.

of the reservoir. The high thermal conductivity of copper ensures a uniform temperature distribution across the base since the strontium crystals sit at the bottom because of gravity. This uniform heating helps to maintain consistent evaporation rates and ensures a steady atomic beam.

Heating is generated by two sets of independent cartridge heaters (Omega CSH-101100/120V), each capable of delivering $100\,\mathrm{W}$ at $120\,\mathrm{V}$. One set is embedded in the nozzle heater, while the other set is placed in the reservoir heater. The heating elements are designed to maintain the nozzle temperature $323.15\,\mathrm{K}$ above the reservoir temperature, with the possibility of achieving even higher temperature differences.

The oven is insulated with Kaowool to minimize heat loss through both radiation and convection. K-type thermocouples (TCdirect 405-002/004) are used to accurately monitor temperatures. One sensor is placed as close as possible to the center of the larger side of the nozzle to ensure precise temperature readings and prevent the nozzle from cooling more than the reservoir. Another sensor is positioned slightly farther away, while two others monitor the nozzle's flange. Lastly, one thermocouple is placed on the copper plate of the reservoir. These sensors have electrically isolated measuring points and can be bent without affecting their thermal properties. In addition to

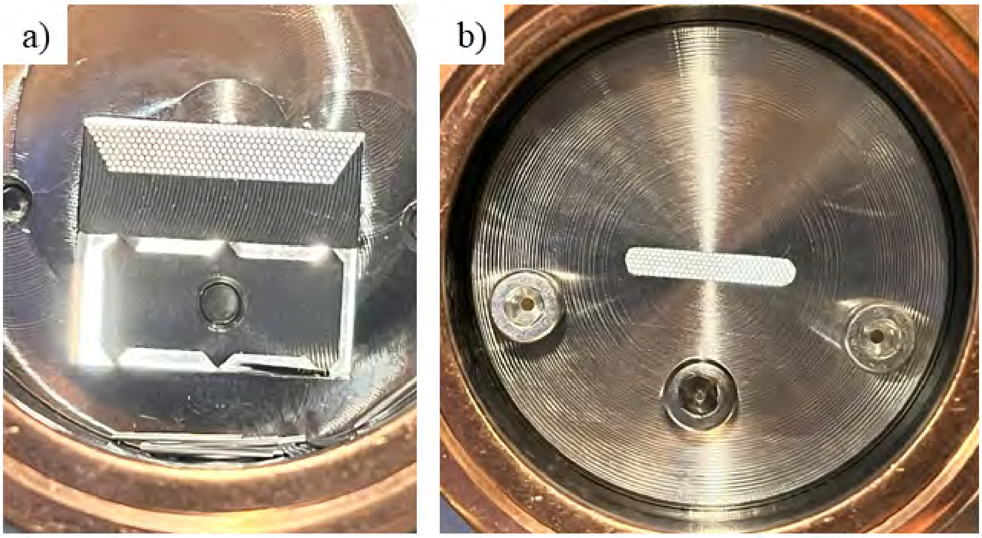

FIGURE 3.13: a) Microtube arrays assembled in the nozzle region and illuminated from behind. b) Active nozzle region.

these, homemade thermocouples are used to monitor the cooling plate and the vacuum chamber cross, further aiding in thermal management.

The aluminum cooling plate also helps with heat management. It is fitted with water-cooled pipes and bolted to the base of the flange (Figure 3.12 b, element 7), dissipating excess heat.

3.5.2 Assembly

All parts are also properly cleaned before and after assembly. The process starts by positioning the oven chamber in a diagonal orientation. An acrylic cap is placed on the external face to hold the microtubes in place. To ensure that the array is properly aligned, a lamp and a mirror are used to provide a clear view during assembly. Once the nozzle clearance is filled with microtubes, the wedge piece is tightened, securing the array. Afterwards, the nozzle flange is installed. Figure 3.13 shows both the assembled nozzle array and the active nozzle region.

The next step involves assembling the reservoir (without strontium) and positioning the heaters and thermocouples. The insulation is applied using several layers of laser-cut Kaowool with varying thicknesses, ensuring uniform coverage throughout the oven. These layers are carefully fitted to maintain even insulation, with pre-cut openings to accommodate the necessary wires for the heaters and thermocouples. This arrangement helps to achieve uniform temperature distribution while minimizing heat loss through radiation and convection.

Afterwards, the empty oven assembly is placed in the vacuum system. The system is pumped down using a primary pump to achieve low vacuum conditions. Once the desired vacuum level is reached, the oven is heated to $400\,^{\circ}\mathrm{C}$ to test its heating and cooling characteristics. This test ensures that the oven's heating elements, temperature control, and insulation function as expected while also serving as a fast baking process to improve vacuum quality. The heating ramp is monitored, and the cooling process is observed to verify uniformity and functionality before the oven is loaded with strontium.

After the test has been completed and the optical cavity has been inserted into the vacuum chamber, as described in the next section, the oven is carefully installed. Proper alignment of the oven nozzle with the cavity's longitudinal axis is critical for optimal performance. To achieve this alignment, $689\,\mathrm{nm}$ light is first coupled into the cavity. Using this beam as a reference, a second beam is aligned in the same vertical plane but at a lower height. This second beam is directed downward towards the nozzle region (see Figure 3.14), which is then used as a reference to align the oven with the longitudinal axis of the cavity. This ensures that the atomic beam is centered within the cavity mode.

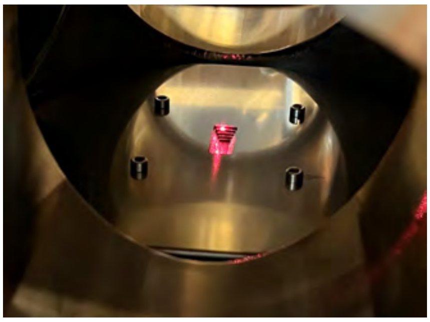

FIGURE 3.14: Method used to align the oven nozzle with respect to the cavity axis: The red light is first coupled to the cavity's TM_{00} mode and then lowered vertically until it reaches the nozzle. Using this light as a reference, the oven position is finely adjusted until the nozzle's longest side is aligned and centered with the red beam.

After attaching and sealing all components of the vacuum chamber, except the oven reservoir, $5\,\mathrm{g}$ of strontium (Alpha Aesar 99.95%) are loaded into the oven reservoir, which is then sealed. A primary pump is activated to begin the vacuum process, and once the pressure reaches 10^{-3} mbar, the ion pump is engaged to further reduce the pressure. Since trapping atoms is not the focus of this setup, ultra-high vacuum levels are not required, and the target pressure is 10^{-3} mbar, which is maintained and may fluctuate with oven temperature. The oven is then heated to $200\,^{\circ}\mathrm{C}$ and left at this temperature for two days to remove any residual water molecules within the chamber, while the ion pump manages to bring the pressure down to the target.

3.6 Laser system

Proceeding with the experimental setup, this section describes the laser systems built to provide the required optical power for collimating the atomic beam, velocity-selection and storage, cleaning and excitationof the high-flux atomic source. Detailed specifications of the laser frequencies, power requirements, and stabilization techniques will be discussed to highlight how they meet the experimental demands.

In Section **??**, the two main transitions of ^{88}Sr, $^1S_0$ -$^1P_1$ and $^1S_0$- $^3P_1$, are briefly described. The first transition is used for optical collimation/cooling of the atomic beam, which requires high optical power due to the high oven temperature ($\sim$773.15 K). The second transition is used for velocity-selection and detection purposes. Additionally, the $^3S_1$-^3P_j were already present.

All the lasers presented in this setup are based on optical diodes and are built in-house, including their current and temperature controllers for stabilization. With the exception of the external cavity diode lasers (ECDLs) used for repumping transitions, all lasers are frequency stabilized using the injection locking technique [29].

In the following subsection, it is recommended that the reader refers to Figure 3.15 while following the description of the blue laser system, since it consists of multiple interconnected optical breadboards.

3.6.1 Blue laser system

The $^1S_0$-$^1P_1$ transition wavelength is 460 nm, commonly referred to as the blue transition. In one of the laboratories within the Strontium BEC group at UvA, Doppler-free absorption spectroscopy [30] is used to stabilize a reference diode laser to this transition via the Pound-Drever-Hall (PDH) technique [31].

The stabilized light from the reference laser is then used to optically seed an Injection Diode Lasers (IDL), which is injection-locked to the reference. Acting as an optical amplifier, the injection-locked laser preserves the spectral properties of the seed light while increasing its power. The amplified output is distributed through polarization-maintaining optical fibers to serve as seed light for three different experimental apparatuses.

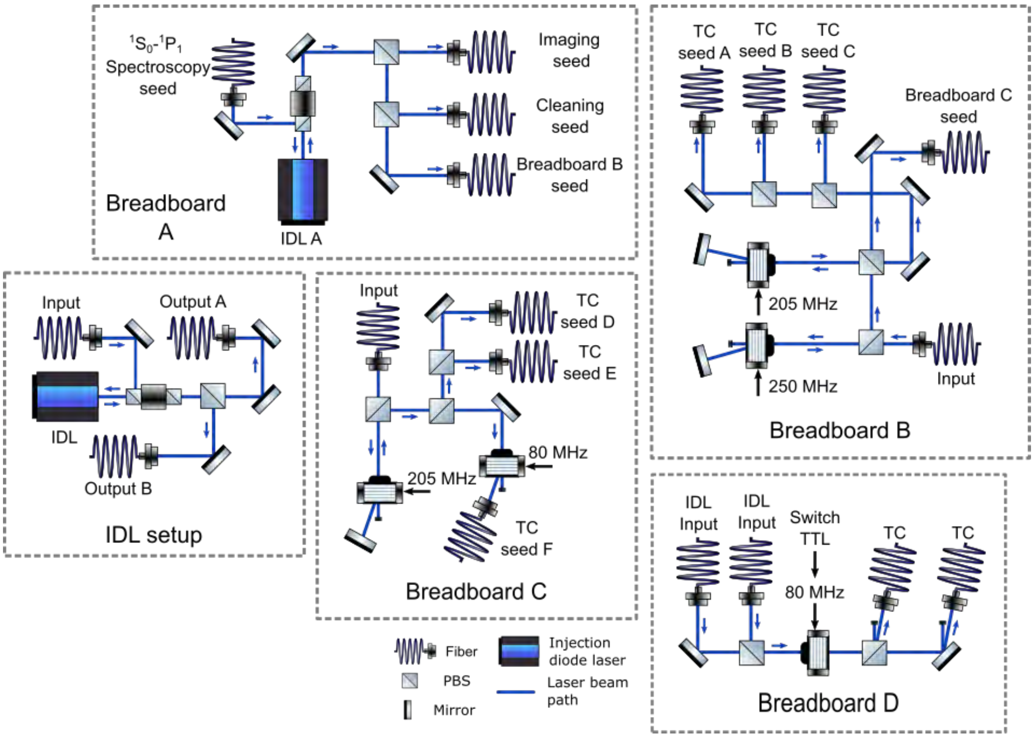

FIGURE 3.15: Blue laser system simplified representation.

The seed light is generated on Breadboard A, which is used to frequency-lock IDL A, a high-power blue diode laser (Nichia NDB4916E). The output of IDL A supplies the necessary power to seed two additional IDLs, "Imaging" (Nichia NDB4216) and "Cleaning," both of which serve as sources of resonant light. The Imaging IDL provides light for fluorescence imaging, while the Cleaning IDL is used to frequency-detune atoms that are in the ground state before they enter the cavity volume. Additionally, IDL A also supplies light for the breadboard B.

Breadboard B is used to frequency-shift the output of IDL A. Initially, the light is shifted by $-500\,\mathrm{MHz}$ using a double-pass acousto-optic modulator (AOM) setup. The total power is then split, with one path directed to a second double-pass AOM, which shifts the light by $410\,\mathrm{MHz}$, resulting in a net shift of $-90\,\mathrm{MHz}$ relative to the atomic resonance. This frequency-shifted light is then used to seed three additional high-power IDLs.

Two IDL setups have their total power directed to only one of their outputs, namely output A, as shown in the IDL setup breadboard. This output is then sent to Breadboard D, where the two inputs are combined, shifted by an additional $80\,\mathrm{MHz}$, and coupled to an optical fiber to serve as the collimation beam, which is responsible for transverse cooling the atoms along the cavity axis and it is time modulated. The third IDL has its output directed through a single-pass AOM, shifted by $80\,\mathrm{MHz}$, and fiber-coupled for use as pre-collimation beam.

The breadboard C receives light from breadboard B that is shifted $500\,\mathrm{MHz}$ below resonance. This input is then double-passed through an AOM, resulting in a final frequency shift of $-90\,\mathrm{MHz}$. A portion of the power is split to feed two other IDL setups, whose outputs are shifted by $80\,\mathrm{MHz}$ and used as counterpropagating middle cooling beam, perpendicular to the cavity axis, and are time-synchronized with the collimation beam.

The remaining light from breadboard C passes through a single-pass AOM, where it is shifted by $80\,\mathrm{MHz}$, yielding a final tunable detuning of $-15\,\mathrm{MHz}$. This light is used to feed the IDL setup that generates the cooling beams orthogonal to the cavity axis, which are positioned above the oven nozzle and remain constantly on.

The complete blue laser system comprises eight high-power blue lasers, each capable of delivering up to $500\,\mathrm{mW}$ of optical power, and one low-power blue laser with a maximum output of $100\,\mathrm{mW}$.

3.6.2 Red laser system

The ${}^1S_0$-${}^3P_1$ transition occurs at a wavelength of $689\,\mathrm{nm}$ and is here referred to as the red transition. As with the blue transition, a reference laser using spectroscopy is frequency-locked to this transition. The stabilized light from the reference laser is then used to seed another laser, which is detuned by $+80\,\mathrm{MHz}$ from the resonance frequency and divided between two experiments.

The stabilized reference light is fed into a low-power red diode (Hitachi VHLG67-38MG), with a portion of its power directed to a high-power diode (Ushio HL69001DG) capable of delivering up to $220\,\mathrm{mW}$. This laser is used for several tasks: it generates the light used to lock the cavity length, provides the velocity-selection beam, and optically feeds the $689\,\mathrm{nm}$ IDL. The cavity lock setup will be discussed later, and for the velocity-selection beam, the light is shifted by $-80\,\mathrm{MHz}$, resonating with the transition.

The $689\,\mathrm{nm}$ IDL is used as a local oscillator (LO) for beat measurements and also provides probing light for the experiment. Initially, the IDL's frequency is set $+80\,\mathrm{MHz}$ above resonance. To use it as the LO, a single-pass AOM shifts the light between $10\,\mathrm{MHz}$ to $40\,\mathrm{MHz}$ below resonance. The portion of the light used for probing first passes through a $+80\,\mathrm{MHz}$ single-pass AOM, followed by a double-pass AOM that shifts the light by a total of $140\,\mathrm{MHz}$. This configuration enables scanning the light by $32\,\mathrm{MHz}$ around the resonance frequency.

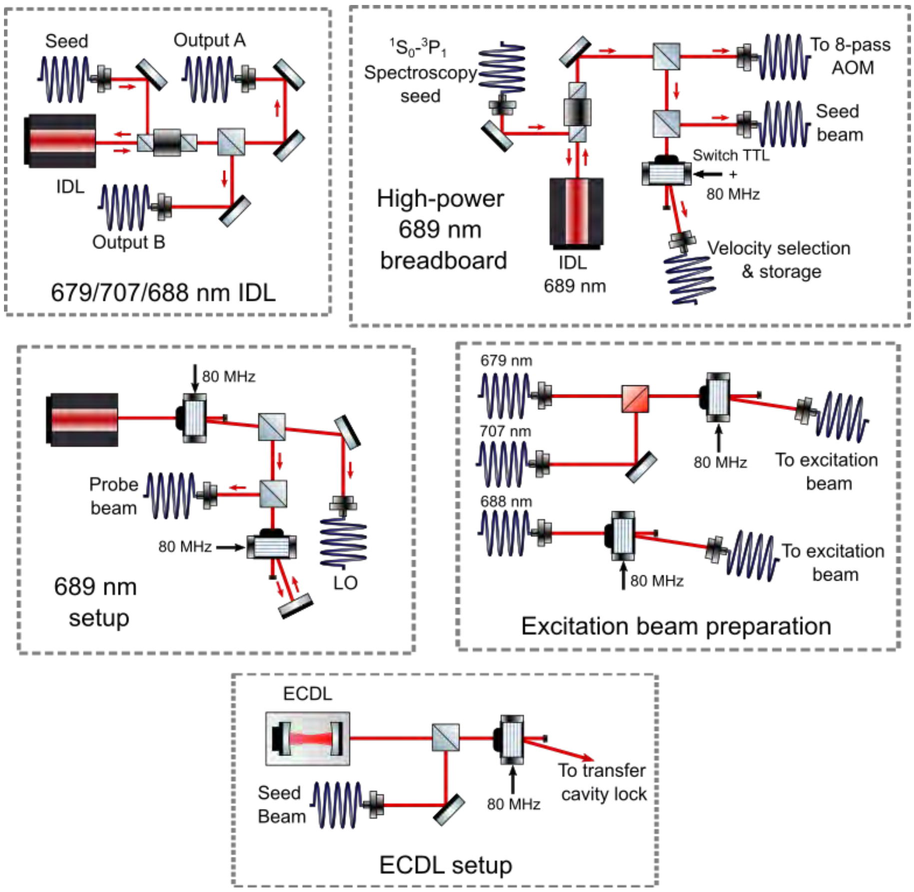

FIGURE 3.16: Red laser system simplified representation.

To address the $^3S_1$-^3P_j transitions, three homemade ECDLs are used, operating at $679\,\mathrm{nm}$, $688\,\mathrm{nm}$, and $707\,\mathrm{nm}$. These ECDLs, along with their current and temperature drivers, are built in-house. The laser design incorporates a wavelength filter that forms an external cavity with an additional mirror. The coarse wavelength tuning is achieved by adjusting the filter, which selects the wavelength fed back into the diode. After this initial alignment, fine control of the frequency is accomplished by locking the piezo-mounted external mirror to a transfer cavity, which itself is locked to the $689\,\mathrm{nm}$ reference laser.

Each ECDL is locked to a transfer cavity $80\,\mathrm{MHz}$ below the resonance. The output light is divided into three different experiments and is used as reference seeds to optically feed IDLs. In this setup, $679\,\mathrm{nm}$ and $707\,\mathrm{nm}$ IDL each seed an additional red diode (Hitachi HL6750MG), which can produce up to $50\,\mathrm{mW}$ output power. The outputs are frequency-shifted using a single-pass AOM setup, allowing flexibility to tune the light up to a few MHz to the red or blue of the transition. Both the $679\,\mathrm{nm}$ and $707\,\mathrm{nm}$ beams are combined and coupled into the same fiber, serving as the excitation beam.

For the $688\,\mathrm{nm}$ laser, higher power is necessary as it is used for both, velocity selection and pumping. The setup follows the same configuration as the $679\,\mathrm{nm}$ and $707\,\mathrm{nm}$ laser setup, but includes an additional follower laser to satisfy the increased power requirement.

For the velocity-selection beam, the output of the first $688\,\mathrm{nm}$ follower is frequency shifted by $-80\,\mathrm{MHz}$ using a single-pass AOM and then coupled to the same fiber as the $689\,\mathrm{nm}$ beam designated for velocity selection. Meanwhile, the second $688\,\mathrm{nm}$ follower is tuned to resonance through a separate single-pass AOM setup, after which its beam is combined with the $679\,\mathrm{nm}/707\,\mathrm{nm}$ excitation beam.

Chapter 4

Apparatus characterization

With all components of the experimental setup functioning correctly and integrated into the apparatus, the next step is to characterize them. This chapter presents measurements of the cavity linewidth, the corresponding values of parameters that depend on it, and the method used for cavity frequency stabilization. Subsequently, the achieved atom number within the cavity mode is discussed.

4.1 Optical cavity

To achieve superradiance in the optical domain, it is essential to couple the atoms to each other through a single mode of an optical cavity. If alternatively many atoms were placed in a volume smaller than the emission wavelength, they would experience decoherence, preventing the phenomenon from occurring. In this sense, the optical cavity is a key component of the experimental apparatus, making it crucial to characterize its properties, as it defines the boundaries and regimes in which the apparatus operates.

In cavity quantum electrodynamics (QED) the single atom cooperativity quantifies the interaction strength between an optical cavity mode and an ensemble of atoms. It quantifies how efficiently the cavity mediates interactions between atoms relative to losses through atomic or cavity decay. Higher cooperativity indicates enhanced atom-cavity coupling, enabling collective atomic interactions through the shared cavity field and enhancing coherence among the atoms [32]. This coupling can lead to phenomena such as superradiance [19].

The single atom cooperativity, $\mathcal{C}$, is determined by the geometrical parameters of the cavity, which characterize the absorptive, emissive, or dispersive coupling of an atom to the cavity mode. It can be expressed as

$$\mathcal{C} = \frac{6\mathcal{F}\lambda^2}{\pi^3 w_0^2}, \tag{4.1}$$

where $\mathcal{F}$ is the finesse of the cavity, λ is the wavelength of the coupled radiation, and w_0 is the waist of the Gaussian TEM_{00} mode. The estimate of $\mathcal{C}$ for the constructed cavity is presented in Table 4.1.

Another important parameter to define is the single-atom coupling g, which is given by [33]

$$g = \frac{-\hat{\varepsilon} \cdot \vec{d}}{\hbar} \sqrt{\frac{\omega}{2\epsilon_0 \hbar V}}, \tag{4.2}$$

where $\hat{\varepsilon}$ is the polarization of the cavity field, $\vec{d}$ is the atomic transition dipole matrix element, ω is the transition frequency, and V is the cavity mode volume. Experimentally, g mainly depends on the cavity geometry and the driving transition.

Although our cavity parameters place the system in a weak coupling regime, it is essential to consider that a continuous atomic beam interacts with the optical cavity, placing many atoms into the cavity mode and potentially shifting the system into a different regime. Consequently, a collective cooperativity parameter is also defined as

$$N\mathcal{C} = \frac{\Omega^2}{\kappa\gamma}, \tag{4.3}$$

where $\Omega = 2g\sqrt{N}$ denotes the collective vacuum Rabi frequency. Using these parameters, the collective decay rate Γ_c can be defined as

$$\Gamma_c = \mathcal{C}\gamma. \tag{4.4}$$

This expression reveals that $\mathcal{C}$ directly influences the collective decay rate. Specifically, if $\mathcal{C} < 1$, the collective decay rate Γ_c can be reduced below the natural linewidth of the individual atoms in the system.

Another important parameter, given the target goal of achieving continuous lasing, is the fractional cavity pulling parameter, $\mathcal{P}$, which quantifies the effect of the cavity on the lasing frequency. It can be defined as [34]

$$\mathcal{P} = \frac{2\gamma_\perp}{2\gamma_\perp + \kappa}, \tag{4.5}$$

where $\gamma_\perp$ represents the effective decay rate from the excited to ground state, defined as $\gamma_\perp = \gamma/2 + 1/T_2$. Here, γ is the natural linewidth of the transition and $1/T_2$ accounts for additional decoherence mechanisms in the system.

If the system linewidth is predominantly governed by the natural linewidth, this expression simplifies to $\mathcal{P} = \gamma/(\gamma + \kappa)$. However, in cases where additional decoherences (T_2) or inhomogeneous broadening are significant, these effects can dominate the effective decay rate, modifying $\gamma_\perp$ accordingly.

In our system, transit-time broadening primarily dictates the effective linewidth, as atoms travel across the cavity waist. For atoms that move at approximately $400\,\mathrm{m\,s^{-1}}$ and a cavity waist of $86\,\mu\mathrm{m}$, the effective linewidth γ is estimated at $2.33\,\mathrm{MHz}$. The resulting value of $\mathcal{P}$, calculated based on these considerations, is presented in Table 4.1. Since $\mathcal{P} < 1$, the influence of the cavity on the lasing output frequency in this system is limited, meaning that the atoms will primarily determine the output frequency.

Parameter	Symbol/Equation	New cavity	Previous cavity
Length	L	$26.65\,\mathrm{mm}$	$27.38(1)\,\mathrm{mm}$
Waist	w_0	$86.82\,\mu\mathrm{m}$	$86.9(2)\,\mu\mathrm{m}$
Linewidth	$\kappa/2\pi$	$6.3(2)\mathrm{MHz}$	$53.9(2)\,\mathrm{MHz}$
Decay rate	$\tau = 1/\kappa$	$0.158(2)\mu\mathrm{s}$	$0.0166(9)\,\mu\mathrm{s}$
Free-Spectral-Range	$\Delta\nu_{FSR} = c/2L$	$5.62\,\mathrm{GHz}$	$5.479(3)\,\mathrm{GHz}$
Finesse	$\mathcal{F} \approx \Delta\nu_{FSP}/\kappa$	$889.6(4)$	$101.6(8)$
Single-atom cooperativity	$\mathcal{C} = 6\mathcal{F}\lambda^2/(\pi^3 w_0^2)$	$10.8(3) \times 10^{-3}$	$1.24(1) \times 10^{-3}$
Cavity pulling	$\mathcal{P} \equiv 2\gamma_\perp/(2\gamma_\perp + \kappa)$	$0.4(2)$	$0.2(3) \times 10^{-3}$
Single-atom coupling	$g/2\pi = \frac{-\hat{\varepsilon}\cdot\vec{d}}{\hbar}\sqrt{\frac{\omega}{2\epsilon_0\hbar V}}$	$23.7\mathrm{kHz}$	$22.4(3)\,\mathrm{kHz}$

TABLE 4.1: Summary of the cavity parameters for the new and the previous cavity. Values without uncertainty are estimated through the cavity design.

4.1.1 Cavity linewidth and other parameters

With the oven operating around $473\,°\mathrm{K}$, which results in a vacuum system pressure of $1\times10^{-7}\,\mathrm{mbar}$ and ensures that there are barely any Sr atoms in the cavity, another cavity linewidth measurement is performed to establish a reference for the finesse achieved for the cavity under vacuum.

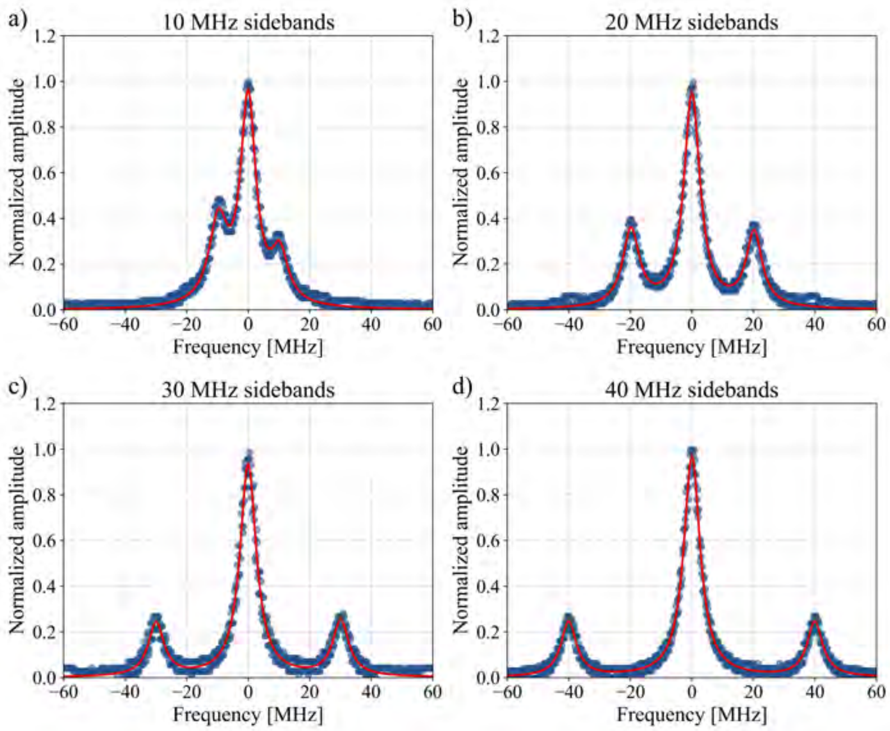

FIGURE 4.1: In vacuum cavity transmission for different sidebands frequency. Blue dots represent data points, while the red line corresponds to a fit using three Lorentzian functions. Linewidth values obtained through fit: a) $6.05 \pm 0.04\,\mathrm{MHz}$; b) $6.32 \pm 0.02\,\mathrm{MHz}$; c) $6.45 \pm 0.02\,\mathrm{MHz}$; d) $6.45 \pm 0.01\,\mathrm{MHz}$.

The measurement follows the same method as the one used to produce Figure 3.10. Sidebands are applied to the carrier while the piezo scans the cavity length, and the transmitted signal is recorded using a photodiode. The data were then fitted using a three-Lorentzian model. By converting the x-axis to frequency, based on the known separation between sidebands, the carrier linewidth can be determined in the correct units. This procedure is performed using four sideband values: $10\,\mathrm{MHz}$, $20\,\mathrm{MHz}$,

$30\,\mathrm{MHz}$, and $40\,\mathrm{MHz}$. The linewidth values obtained from these fits are used to calculate an average final linewidth and its associated uncertainty.

Based on the fitting results shown in Figure 4.1, the cavity linewidth and its uncertainty are defined as the average of the measured values, which are shown in Table 4.1.

4.1.2 Frequency stabilization

Stabilization of the optical cavity frequency is achieved using the Pound-Drever-Hall (PDH) technique [35], which locks the length of the cavity by applying feedback to the piezo stack to maintain resonance with a transverse electromagnetic mode (TEM) of the optical cavity.

It is necessary to lock the cavity to a TEM mode that is also resonant with the ${}^3P_1$-${}^1S_0$ atomic transition. However, resonant light should not be used, as it would drive the atoms. Instead, a transverse mode, such as the TEM01 or TEM02, could be reached, which are far detuned in frequency but accessible with an AOM. This is achieved by detuning a resonant $689\,\mathrm{nm}$ light beam using a setup which is assembled using a single AOM at $350\,\mathrm{MHz}$, with which the optical beam interacts eight times, a setup inspired by [36].

The locking light is provided by the high power $689\,\mathrm{nm}$ breadboard, as shown in Figure 3.16, and directed to the input of the 8-pass AOM breadboard, shown in Figure 4.2. The light is shifted by a total of $2.56\,\mathrm{GHz}$ and is resonant with the TEM02 mode, which, with such a frequency separation from the atomic resonance, ensures that the atoms in the ${}^3P_1$ state do not interact with the photons of the cavity locking light. The 8-pass AOM setup includes a telescope formed by two lenses with focal lengths of $f = 150\,\mathrm{mm}$, spaced at a distance equal to the sum of their focal lengths, with the AOM positioned at the midpoint between them. Additionally, two periscopes are arranged so that the optical beam can pass through the AOM multiple times. The top and side views of the optical setup, including the optical beam path, are shown in Figure 4.2. The total optical efficiency achieved in this setup is approximately 23%, and the AOM can be scanned around its central frequency in a range of $20\,\mathrm{MHz}$, providing a total tuning range of $160\,\mathrm{MHz}$ for fine optimization.

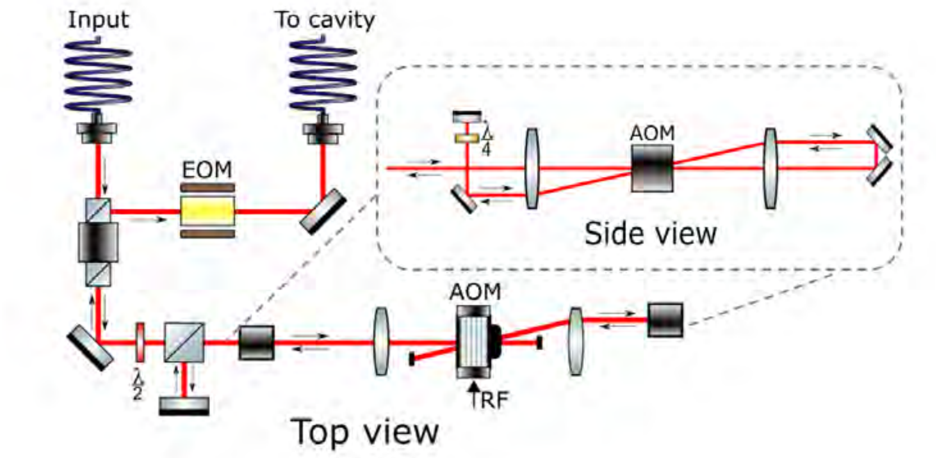

FIGURE 4.2: An 8-pass AOM setup employed to achieve a total frequency shift of 2.56 GHz from the resonance of the $^3P_1$-$^1S_0$ transition.

After the 8-pass AOM, the output light passes through a homemade electro-optical modulator (EOM), is fiber-coupled, and is directed for coupling into the optical cavity. An additional breadboard contains the optics and electronics necessary for a standard PDH lock, which generates a feedback signal sent to the piezo stack, responsible for adjusting the cavity length. The sidebands are generated by the EOM at 56.26 MHz, and the reflected light is detected using a Thorlabs PDA. The detected signal is subsequently mixed down, demodulated and sent to a Red Pitaya, which provides a PID controller with adjustable parameters accessible through a user interface.

The resulting error signal from the setup is shown in Figure 4.3 a). This signal is used to calibrate the x-axis in terms of frequency, which is then applied to analyze the frequency deviation of the error signal while the lock is engaged. Figure 4.3 b) displays the analysis, showing two distributions: one centered around 1.36 kHz and the other around 1.57 kHz, the origins of which were not investigated. The total distribution width is 0.35 kHz, which is considered stable enough for its intended application.

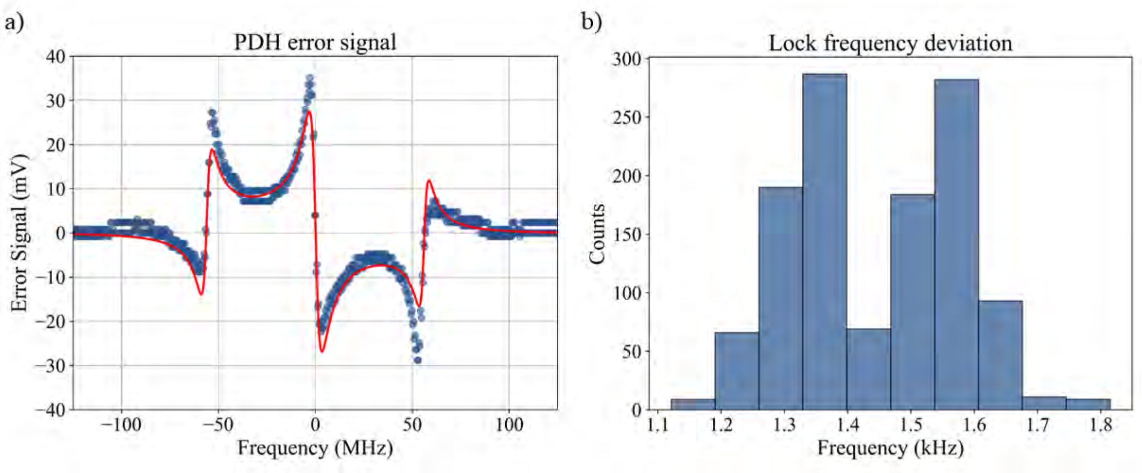

FIGURE 4.3: a) Cavity PDH error signal. b) Histogram of frequency deviations of the error signal while the cavity remains locked. Blue represent the experimental data, and the red line corresponds to the fit.

4.2 Normal Mode Splitting

This section describes a method for estimating the number of atoms within the cavity mode, based on the phenomenon known as Normal Mode Splitting (NMS) or vacuum Rabi splitting. Although this splitting reveals the quantum nature of the electromagnetic field [37], it can also be understood through a classical model of linear absorption and dispersion [38]. This phenomenon has been widely studied on various platforms, from single atoms coupled to optical cavity modes [39], to systems of Rydberg atoms and Bose-Einstein condensates, as well as in optomechanical systems and chip-integrated cavities [40, 41, 42].

4.2.1 Strong coupling regime

The strong coupling regime is defined by the condition $\mathcal{C} > 1$, indicating a situation in which the atomic dipole is no longer simply driven by the unperturbed incident field. Instead, the emitted field from the atom, circulating within the cavity, must be self-consistently included in the total driving field. Consequently, for $\mathcal{C} > 1$, the back-action of the cavity field generated by the oscillating atomic dipole on that same dipole becomes significant and cannot be ignored.

When there is an ensemble of N_0 atoms within the cavity mode, each atom contributes to the overall interaction strength. Atoms in the antinodes of the cavity mode couple strongest to the cavity, whereas atoms in the nodes do not couple. We take this into account by using the mean intracavity atom number $N = N_0/\sqrt{2}$ in the following. The collective coupling strength scales with the square root of the mean intracavity atom number and is given by

$$\bar{g} = 2g\sqrt{N}, \tag{4.6}$$

where g is the single-atom coupling strength. In a large ensemble, this collective coupling can reach the strong-coupling regime, even if each atom individually has a weak interaction with the cavity mode.

The collective Rabi frequency of the system, defined as $\Omega = 2g$, represents an enhanced rate of coherent energy exchange between the atomic ensemble and the cavity mode. When Ω exceeds both the cavity decay rate κ and the spontaneous atomic emission rate γ, the system exhibits strong collective coupling. This regime leads to a split in the energy spectrum [13], known as collective vacuum Rabi splitting, or NMS, and can be used to estimate the atomic population of the system, resulting in two new energy levels that correspond to collective Rabi splitting. The Hamiltonian for an ensemble of N atoms coupled to a single mode of the cavity can be expressed as

$$H = \hbar \sum_{i=1}^{N} \omega_0 \sigma_i^\dagger \sigma_i + \hbar\omega a^\dagger a + \hbar \sum_{i=1}^{N} \bar{g}(\sigma_i^\dagger a + \sigma_i a^\dagger), \tag{4.7}$$

with ω_0 being the atomic transition frequency, ω the frequency of the cavity mode, $\sigma^{(\dagger)}$ the atomic raising (lowering) operators and $a^{(\dagger)}$ the cavity mode creation (annihilation) operator.

In a system where an ensemble of atoms interacts strongly with an optical cavity mode, collective energy states and dressed states emerge due to the coherent interaction between the ensemble and the quantized electromagnetic field of the cavity.

The ensemble of atoms forms a single, collective state that couples to the cavity field. This state can be considered to behave as a single two-level system but with an enhanced coupling strength. The collective state is entangled with the cavity mode, and the system's energy states are divided into two dressed states because of the strong interaction. These states are combinations of the ensemble and cavity mode states, reflecting the shared excitation between the atoms and the cavity field.

To observe this collective vacuum Rabi splitting, a probe laser is scanned across the resonance frequency of the cavity. Instead of a single transmission peak at the natural resonance of the cavity, two peaks appear, separated by the collective Rabi frequency Ω. The separation between these peaks is a direct measure of the collective coupling strength and is a clear indication of strong coupling in an atomic ensemble.

In real-world systems, atoms in the ensemble may have slightly different resonance frequencies because of inhomogeneous broadening caused by Doppler shifts, Zeeman shifts, or other effects. This broadening can reduce the effective cooperativity of the ensemble by diminishing the coherence of the collective coupling. However, if the collective coupling strength Ω remains larger than the broadening, the Rabi vacuum splitting will still be observable, although potentially with reduced contrast or broadened peaks.

4.2.2 Measurement of steady-state vacuum Rabi splitting

When vacuum Rabi splitting occurs, the modes are separated by $\Omega = 2g\sqrt{N}$. Resolving the two modes indicates that the coherent interaction rate exceeds the decay rates present in the system. Typically, achieving Ω greater than the atomic transition linewidth is more feasible for narrow transitions. However, achieving Ω larger than the cavity decay rate for such transitions is significantly more challenging and requires the use of high-finesse cavities.

Additionally, when narrow transitions are used, the coherent interaction rates are comparatively slower, making it more challenging to overcome decoherence effects, such as Doppler shifts. For these reasons, the observation of vacuum Rabi splitting in the experimental apparatus presented is possible only for atoms in the $^1S_0$ ground state.

In order to observe it, the atomic beam is prepared as usual, with cooling methods applied, as the atoms propagate vertically through the vacuum chamber while the oven is kept at $783.15\,^{\circ}\mathrm{K}$. A π-polarized, resonant $689\,\mathrm{nm}$ probe light is coupled to the cavity TEM00 mode and scanned through resonance. Considering the saturation intensity of the transition, $\mathrm{Isat} = 2.95\,\mu\mathrm{W\,cm^{-2}}$, the intracavity intensity due to the probe light is approximately $2.6\ \mathrm{I_{sat}}$.

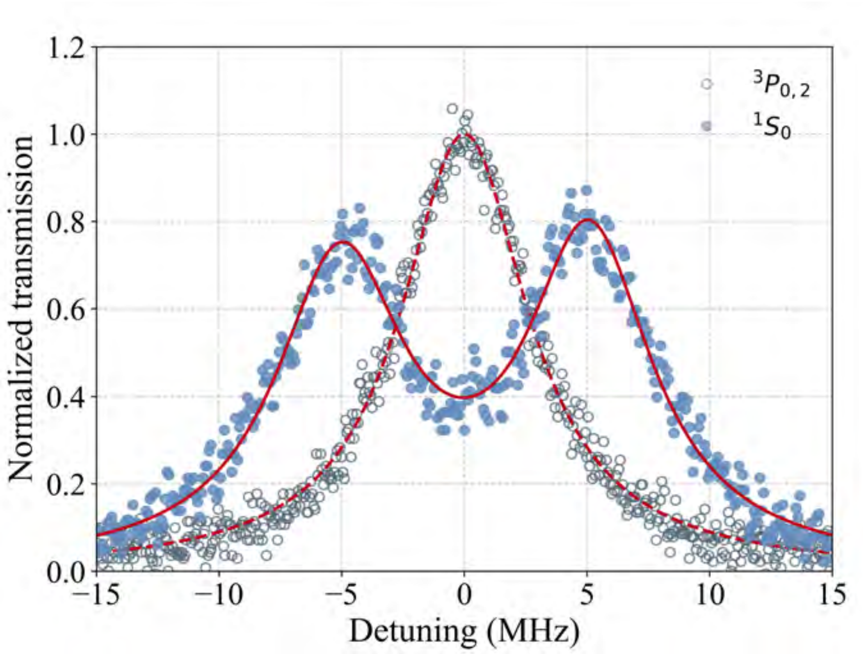

FIGURE 4.4: The NMS spectrum demonstrating the strong coupling regime for ground-state atoms, represented by the blue dot dataset. The orange dots corresponds to an 'empty cavity' signal. Both datasets are normalized to the maximum amplitude of the empty cavity signal. The red dashed curve represents a single-Lorentzian fit to the reference (empty cavity) data, while the solid red curve represents a two-Lorentzian fit to the spectrum with ground-state atoms, from which the splitting value is extracted.

To measure the NMS spectrum, the data are first acquired by pumping the atoms into the $^3P_{0,2}$ metastable states, which mimics an empty cavity signal as those atoms barely interact with the cavity mode. Scanning the probe light $30\,\mathrm{MHz}$ symmetrically across the resonance results in the orange data shown in Figure 4.4. This serves as the reference signal. Subsequently, data is recorded for a transversally cooled beam of ground state atoms. To prepare this beam, the atoms are optically pumped to $^3P_1$ several cm below the cavity mode, which enables most atoms decay to the $^1S_0$ ground state before entering the cavity mode. These atoms then interact with the probe beam in the cavity, resulting in the blue data. The fit to the data reveals a splitting of $10.1(5)\,\mathrm{MHz}$. Using this value and the single-atom coupling constant listed in Table 4.1, this corresponds to a mean intracavity atom number of 9.14×10^4 ground-state atoms strongly interacting with the cavity field in steady-state for the mentioned oven temperature.

Chapter 5

A qualitative method for real-time atom number optimization

This chapter introduces the concepts of frequency modulation (FM) spectroscopy in the presence of an optical resonator, a technique also known as cavity enhanced FM spectroscopy [43]. In this work, it is used as a qualitative method to optimize the apparatus by directly observing a real-time atomic signal. However, it is not used to extract quantitative parameters.

5.1 Frequency Modulation Spectroscopy

Frequency Modulation Spectroscopy (FMS) is a laser-based spectroscopic technique that uses the principles of frequency modulation to achieve high sensitivity in detecting atomic or molecular absorptions [44]. The core mechanism involves modulating the frequency of a laser, typically in the MHz range, and analyzing the resulting modulation of the transmitted or reflected signal as it interacts with a sample. The description begins by considering a laser beam with an electric field given by

$$\mathbf{E}(t) = \mathbf{E}_0 e^{i\omega 0t} + c.c., \tag{5.1}$$

where ω_0 is the angular frequency of the laser and $\mathbf{E}_0$ is the amplitude of the electric field. When the laser beam is modulated by a frequency Ω, the resulting field is expressed as

$$\mathbf{E}_m(t) = \mathbf{E}_0 \exp\left[i\omega_0 t + iM\sin(\Omega t)\right] + c.c., \tag{5.2}$$

where M is the modulation index. By expressing above equation in terms of Bessel functions and considering the case where $M << 1$, the field $\mathbf{E}_m(t)$ can be approximated to first order in M as [45]:

$$\mathbf{E}_m(t) \approx \mathbf{E}_0 \left\{ e^{i\omega_0 t} + \frac{M}{2} \left[e^{i(\omega_0+\Omega)t} - e^{i(\omega_0-\Omega)t} \right] \right\}. \tag{5.3}$$

The resulting signal consists of a carrier at frequency ω_0, along with lower and higher sidebands shifted by $\pm\Omega$, respectively. Once the light interacts with an atomic ensemble, any resonances cause the field's amplitude and phase to change independently, which can be described by the functions $\alpha(\omega)$ and $\phi(\omega)$. The transmitted signal is

$$E_T(t) \sim \alpha(\omega_0)e^{i\omega_0 t}e^{i\phi(\omega_0)} + \frac{M}{2} \left[\alpha(\omega_0+\Omega)e^{i(\omega_0+\Omega)t}e^{i\phi(\omega_0+\Omega)} - \alpha(\omega_0-\Omega)e^{i(\omega_0-\Omega)t}e^{i\phi(\omega_0-\Omega)} \right]. \tag{5.4}$$

A photodetector can be used to measure the intensity of the transmitted field, which is given by $V_T(t) \sim |E_T(t)|^2$. After extensive trigonometric calculations, the detected signal can be written as

$$V_T(t) \sim \alpha(\omega_0) \left[1 + \frac{M}{2} \left(\Delta\alpha \cos(\Omega t) + \Delta\phi \sin(\Omega t) \right) \right], \tag{5.5}$$

where

$$\Delta\alpha \equiv \alpha(\omega_0 - \Omega) - \alpha(\omega_0 + \Omega), \tag{5.6}$$

$$\Delta\phi \equiv \phi(\omega_0 + \Omega) + \phi(\omega_0 - \Omega) - 2\phi(\omega_0). \tag{5.7}$$

Within the above definitions and equation 5.5, the acquired signal consists of an interference envelope whose amplitude encodes the frequency-dependent absorption and dispersion functions. To extract these functions, one can mix $V_T(t)$ with a tunable phase signal $\sin(\Omega t + \phi)$. Then, by applying a low-pass filter to the mixed signal, one gets

$$\Delta\alpha \sin(\theta) + \Delta\phi \cos(\theta). \tag{5.8}$$

Studying absorption or dispersion requires the proper adjustment of the phase θ. Either $\Delta\alpha$ and $\Delta\phi$ have zero crossings when the laser frequency matches a resonance.

5.2 Cavity-Enhanced FM Spectroscopy

This technique has been extensively studied and applied in various fields, from frequency standards to trace gas detection [43, 46, 47, 48]. Placing an optical cavity around the atomic ensemble increases the length of the light-atom interaction by $2\mathcal{F}/\pi$, which enhances absorption contrast and directly improves detection sensitivity.

The FM spectroscopy is partially modified by applying the sidebands at an FRS away from the carrier frequency, ensuring that the FM triplets are transmitted through the cavity identically. As a result, they are equally affected by frequency-to-amplitude noise conversion, making this approach a "noise-immune" technique [49].

Additionally, the cavity builds up intracavity power, enabling the use of low-power light inputs and consequently generating a low-power output. This makes it particularly suitable for use with an APD. Furthermore, the cavity ensures that only frequencies that match the resonance condition are amplified, reducing background noise. This amplifies weak spectroscopy signals while also preserving the benefits of FM spectroscopy.

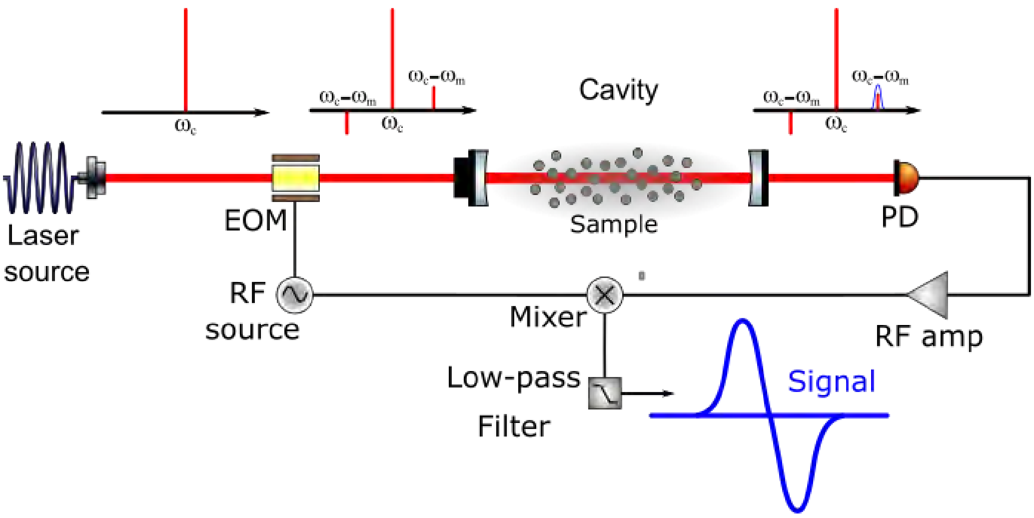

FIGURE 5.1: Basic principle and setup for a cavity enhanced FM spectroscopy. For the setup used in the experimental apparatus present here, the carrier and sidebands lay within the same cavity mode.

5.3 Experimental realization

In our setup, sidebands are applied to the probe beam at $7.1\,\mathrm{MHz}$, allowing them to couple to the same mode as the carrier while being scanned in frequency, rather than separated by a free spectral range, as is commonly done. Since the cavity linewidth is $6.3\,\mathrm{MHz}$, the probe beam is scanned over a total range up to $12\,\mathrm{MHz}$ to effectively map the cavity dispersion feature.

In order to distinguish the dispersion signal of the cavity from the one of the atoms, we pump the atoms from the $^3P_{0,2}$ states to the $^3P_1$ or $^1S_0$ state at a frequency of $f_{\mathrm{m,at}} = 2\,\mathrm{kHz}$. Only the optically pumped atoms interact significantly with the cavity mode. The dispersion signal caused by the atoms can then be measured via the beat signal with the probe's sidebands at $7.098\,\mathrm{MHz}$ and $7.102\,\mathrm{MHz}$, i.e. $f_{\mathrm{m,at}}$ away from the beat signal that also exists without modulating the atomic state. Measurements can be taken from either ground- or excited-state atoms, depending on the vertical position of the excitation beam. If the excitation beam is positioned $1\,\mathrm{cm}$ below the cavity mode, the atoms have enough time to almost all decay to the ground state. Conversely, if the beam is positioned as close as possible to the cavity mode, $^3P_1$ state atoms interact with the probe beam.

The probe is scanned over the frequency range within $10\,\mathrm{s}$. The output light is detected using an APD, and the signal is visualized with a spectrum analyzer. To observe amplitude variations, the spectrum analyzer is centered on the atomic signal frequency of $7.098\,\mathrm{MHz}$ with its span set to zero. Throughout this measurement, the cavity is kept locked and resonant with the TM_{00} mode.

The signal obtained from the spectrum analyzer is shown in Figure 5.2. First, as a reference, the absolute value of the cavity dispersion signal, corresponding to the beat signal at $7.1\,\mathrm{MHz}$, is recorded, as shown by the dark blue curve. The probe light is adjusted until the cavity dispersion signal has a maximum of approximately $-30\,\mathrm{dBm}$. Then the center frequency of the spectrum analyzer is set to $7.098\,\mathrm{MHz}$ to map the dispersion caused by the atomic signal (orange curve). The alignment, power, and frequency of the laser beams are adjusted to optimize this signal until the highest amplitude is observed. This signal is also used to align the excitation beam: if the beam fully overlaps with the cavity mode, the feature is not observed, whereas if it is positioned too low, only ground-state atoms are probed.

During daily optimization, the highest amplitude of the atomic signal relative to the

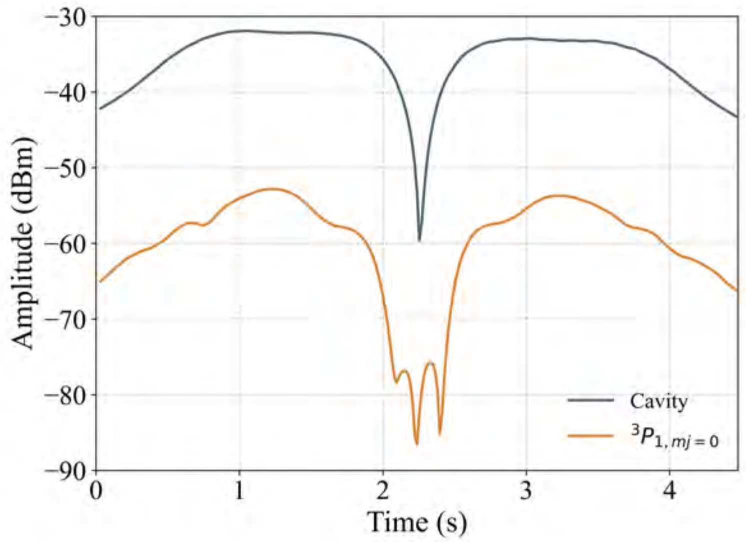

FIGURE 5.2: Cavity-enhanced frequency modulation spectroscopy. The laser frequency is scanned over $16\,\mathrm{MHz}$ in a triangular fashion with a $5\,\mathrm{s}$ period. The figure shows the amplitude of the beat note at $7.1\,\mathrm{MHz}$ (dark blue), representing the cavity dispersion, and the beat note at $7.098\,\mathrm{MHz}$, mapping the atomic dispersion. The signal was obtained at an oven temperature of $803.15\,°\mathrm{K}$.

cavity signal is typically around $-20\,\mathrm{dBm}$. The central feature observed in the atomic signal is attributed to atomic saturation caused by the high probe intensities within the cavity.

Chapter 6

A new approach to optical cooling

This chapter introduces the concept of optical molasses, a standard cooling technique widely used in atomic physics. Following this, the challenges encountered with its application in the earlier version of the apparatus are presented. Finally, a novel approach to cooling the atoms is shown, specifically developed for the current version of the experimental apparatus described in this thesis.

6.1 Laser cooling

Laser cooling is a commonly employed technique in which a moving atom interacts with a laser field with a frequency near the atomic resonance and experiences a reduction in its kinetic energy. When a laser is tuned slightly below the atomic resonance frequency (red-detuned), the Doppler shift increases the probability that atoms moving opposite to the laser beam's propagation direction absorb photons. This interaction slows the atoms, effectively reducing the temperature of the atomic gas.

The radiation pressure exerted by the red-detuned laser acts as a strong damping force on the atomic motion, enabling rapid cooling. The minimum achievable temperature is fundamentally limited by the energy width of the resonant transition.

In a configuration with six counterpropagating laser beams, atoms experience quasi-confinement within three dimensions. The velocity of the atoms is rapidly damped, confining their motion to short distances within the damping time. As the atoms are also accelerated in random directions by the spontaneous emission of the scattered photons, their motion resembles Brownian motion.

The term optical molasses comes from the viscous damping of the atomic motion. Although typically associated with the six-beam configuration, the term can also describe strong cooling accompanied by diffusive motion in one or two dimensions [50].

6.2 Radiation pressure force

Consider a two-level atom with a transition frequency ω_0 between the ground and excited states and a natural linewidth Γ. The atom is irradiated by a laser beam with frequency ω and wavelength λ. The detuning of the laser frequency from the atomic resonance is defined as $\Delta = \omega - \omega_0$.

The strength of the laser-induced coupling between the ground and excited states is characterized by the Rabi frequency Ω. On resonance, the atomic transition saturates at the saturation intensity

$$I_s \equiv \frac{\pi h c}{3\lambda^3 \tau}. \tag{6.1}$$

The laser intensity in units of the saturation intensity is the on-resonance saturation parameter

$$s_0 \equiv \frac{I}{I_s}, \tag{6.2}$$

which is related to the on-resonance Rabi frequency as

$$s_0 \equiv \frac{2\left|\Omega\right|^2}{\Gamma^2}. \tag{6.3}$$

Taking the laser detuning into account the saturation parameter becomes

$$s \equiv \frac{s_0}{1 + \left(\frac{2\Delta}{\Gamma}\right)^2}, \tag{6.4}$$

In steady state the excitation rate and the decay rate are equal, and the total scattering rate γ_p of light from the laser field is given by

$$\gamma_p = \frac{\Gamma}{2} \frac{s_0}{1 + s_0 + \left(\frac{2\Delta}{\Gamma}\right)^2}. \tag{6.5}$$

At high intensities, $s_0 >> 1$, this equation can be rewritten as

$$\gamma_p = \left(\frac{s_0}{1 + s_0}\right) \left(\frac{\Gamma/2}{1 + \left(\frac{2\Delta}{\Gamma'}\right)^2}\right). \tag{6.6}$$

Here, $\Gamma' = \Gamma\sqrt{1 + s_0}$, is the power-broadened linewidth of the transition.

The average force from absorbing many photons is given by

$$F_{\text{sp}} = \hbar k \gamma_p, \tag{6.7}$$

where $\hbar k = \hbar 2\pi/\lambda$ is the momentum of a photon. After absorbing each photon the atom emits a photon in a random direction. The momentum kicks from these spontaneously emitted photons averages out.

Increasing the absorption rate by increasing the intensity beyond the saturation intensity primarily enhances the rate of stimulated emission, with momentum transfer occurring in the exactly opposite direction to that of absorption. This leads to the saturation of F_{sp} at its maximum value of $\hbar \text{k}\Gamma/2$.

6.3 Optical molasses

Atoms moving slowly inside the volume of two counter-propagating, slightly red-detuned laser beams experience a net slowing force proportional to their velocity. For sufficiently small velocities, this force is approximately proportional to the velocity, resulting in viscous damping, which gives the technique its name, "optical molasses."

Neglecting the effects of stimulated emission and accounting for the Doppler shift ω_D caused by the atomic velocity, the optical forces exerted by two counter-propagating laser beams are described by

$$F_{\pm} = \pm \hbar k \frac{\Gamma}{2} \frac{s_0}{1 + s_0 + \left[\frac{2(\delta \mp \omega_D)}{\Gamma}\right]^2}, \tag{6.8}$$

where the index $\pm$ indicates the travel direction of the laser beams. The sum of the forces exerted by the two laser beams on the atom, in first-order approximation in v, becomes

$$F_{OM} \simeq \frac{8\hbar k^2 \delta s_0}{\Gamma \left[1 + s_0 \left(\frac{2\delta}{\Gamma}\right)^2\right]^2} v \equiv -\alpha v, \tag{6.9}$$

where α is the damping coefficient. With the basic concepts and equations established, the following section presents the challenges encountered when using an optical molasses in the previous setup.

6.4 Optical molasses setup

In the previous version of the apparatus, the standard optical molasses technique on the broad ($30\,\mathrm{MHz}$ linewidth) blue $^1S_0$- $^1P_1$ transition, was used to transversely collimate the atomic beam over a vertical distance of $5\,\mathrm{cm}$. The beams perpendicular to the cavity axis, in the y direction, although not critical, were expected to contribute to an increase in the number of atoms within the volume of the cavity mode. Meanwhile, beams along the z-axis played a crucial role in reducing Doppler spread along the cavity axis, which is essential to establish phase coherence.

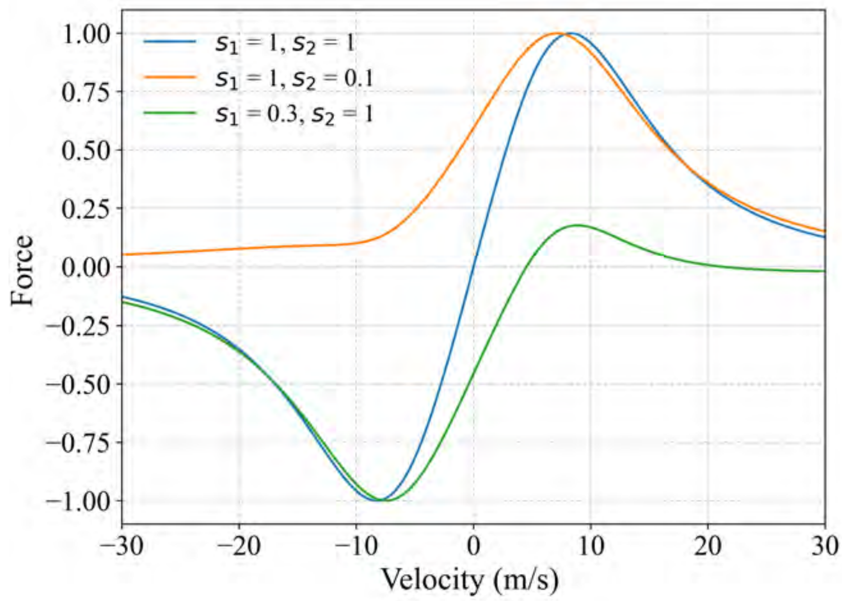

FIGURE 6.1: Normalised optical force as a function of the atomic velocity. The chosen detuning is half of the transition linewidth to better match the experimental parameters, and the force is normalized. The curves represent the imbalanced situation (orange and green) and the perfectly balanced case (blue).

The beams along the y-axis were detuned from resonance by $-14\,\mathrm{MHz}$ and operated at an intensity of $1.8I_s$. Meanwhile, the beams along the z-axis were detuned by $-16\,\mathrm{MHz}$ with an intensity of $5I_s$. The saturation intensity for this transition is $I_s = 41\,\mathrm{mW\,cm^{-2}}$. When the oven operated at temperatures around $820\,°\mathrm{K}$, the z-axis molasses beams experienced significant absorption due to the high optical density of the atomic beam, which could reach 70% to 90% depending on atom flux, i.e. oven temperature. As a result of the differential absorption between the counterpropagating beams, the forces exerted on the atoms became position-dependent, leading to a Doppler distribution broader than expected for a balanced system.

Figure 6.1 shows the cooling force as a function of atom velocity. The blue curve represents the case of balanced beams, where the force is zero at $0\,\mathrm{m\,s^{-1}}$. The orange curve corresponds to the case where the counterpropagating beams are unbalanced, with one beam being 90% weaker than its counterpart. In this scenario, no cooling occurs, as the force remains nonzero even at zero velocity, pushing the atom further away from the target velocity range value of $\pm 1\,\mathrm{m\,s^{-1}}$.

The green curve represents the case where one of the beams is 70% weaker. Here, the force is minimal or zero for several velocities, around $5\,\mathrm{m\,s^{-1}}$ and from $20\,\mathrm{m\,s^{-1}}$ to $30\,\mathrm{m\,s^{-1}}$, meaning that no cooling occurs for atoms at those velocities. Outside this range, the atoms are further accelerated, similar to the behavior observed in the case of the orange curve.

When considering the atomic beam's spatial distribution, at its center, the molasses cooling beams are intensity balanced, and the atoms are cooled towards zero velocity along the cavity axis. Moving away from the center, the molasses beams are imbalanced, leading to cooling into a finite velocity class. The further away from the center, the higher that velocity class. If the beam imbalance gets too high the atom is purely accelerated, as discussed above. On the left and right side from the center, the sign of the velocity class into which the molasses beams cool is opposite. For an absorption of 70%, this implies that the total velocity spread along the cavity axis is twice the velocity at the zero crossing shown in the figure. This spread is significantly larger than the Fourier linewidth of atoms crossing the cavity and exceeds the limit imposed by the condition that atoms should not move from one antinode to the neighboring one while traversing the cavity. The effects of such imbalanced optical cooling in the system were thoroughly studied in [27].

Small angles between the atomic beam and the x-axis within the cavity plane were observed through velocity shifts in the cavity mode. These shifts were attributed to tilts in the oven nozzle and an imbalance in the optical molasses. High oven temperatures were required to achieve the target intracavity atom number. However, operating at such high temperatures led to significant absorption of the molasses beams, making it even more challenging to correct the atomic beam angles. In this context, a new approach to the cooling method was conceived and is presented in the following section.

6.5 Electron-shelving cooling

To improve power efficiency and cooling performance, the proposed approach, named *Electron-shelving cooling*, utilizes a single blue laser that is activated periodically, rather than keeping two optical molasses beams continuously on. The idea is to allow the atoms to interact with the blue laser for a short period, during which atoms are pushed toward zero velocity along the cavity axis. After this initial interaction, the blue beam is turned off and a second beam, consisting of $689\,\mathrm{nm}$ and $688\,\mathrm{nm}$ light, is activated. This beam optically pumps atoms that are within the $\pm 1\,\mathrm{m\,s^{-1}}$ velocity range to the metastable states ${}^3P_{0,2}$, which act as storage states, preventing the atoms from further interacting with the blue beam. After a short while, the blue beam is briefly switched on again. This process is carried out repeatedly as the atoms traverse both beams upward (x-axis) towards the cavity volume.

To evaluate the feasibility and advantages of this method compared to that of standard optical molasses, some estimations can be performed. First, considering a typical vertical velocity of $v_x = 400\,\mathrm{m\,s^{-1}}$ and the oven microtubes of diameter $\varnothing = 0.305\,\mathrm{mm}$ and length $l = 8\,\mathrm{mm}$, the radial velocity of the atoms out of the oven nozzle can be estimated as

$$v_r = v_x \varnothing / l = 15.25\,\mathrm{m\,s^{-1}}. \tag{6.10}$$

Given that the available vertical distance for laser cooling is $5\,\mathrm{cm}$, the corresponding available time for cooling to be performed is $125\,\mathrm{\mu s}$. The desired velocity range along the cavity axis results in a Doppler spread of around $\pm 2\,\mathrm{MHz}$. This corresponds to a Fourier-limited time of $0.46\,\mathrm{\mu s}$. Taking into account this value and the vertical velocity v_x, the available distance for a single optical pumping pulse is $0.184\,\mathrm{mm}$.

Assuming a laser detuning of 0.5Γ and a beam intensity of $1I_s$ for the blue transition, the acceleration experienced by an atom can be estimated using Equation 6.8 as approximately $3 \times 10^5\mathrm{m\,s^{-2}}$. For the target radial velocity range, the time it takes for the blue beam interacting with the atom is $3\,\mathrm{\mu s}$. This corresponds to a distance of $1\,\mathrm{mm}$ and allows for approximately 33 interaction stages as the atom travels upward. The blue interaction stages will be called *push stage* now on. After the mentioned stage, there should be a change in the radial velocity of a maximum $\Delta v_r^{max} \sim 33\,\mathrm{m\,s^{-1}}$. Meanwhile, using optical molasses the maximum radial velocity changed would be $\sim\ 38\,\mathrm{m\,s^{-1}}$, which is very similar. During the interaction time in the optical molasses, each atom scatters approximately 8000 blue photons. In contrast, using the proposed approach, the number of blue photons scattered per atom during the push stage is approximately 1700. This corresponds to an efficiency improvement of ~ 4.5 times. The reason for that large difference is that atoms that are molasses cooled to zero velocity continue to scatter photons at a high rate, whereas they are pumped to states that don't scatter photons when using the Electron-shelving cooling.

The new approach is shown to be more efficient and provides a reasonable safety margin for achieving the target radial velocity, even for atoms with higher initial velocities, and considering potential imperfections in the cooling and storage process.

6.6 Implementation

Due to constraints in physical space and optical components, as well as the need for improved power efficiency, the blue push beam is configured with dimensions of $0.1 \times 1.5\,\mathrm{cm}$, with its longer side aligned along the x-axis. In this configuration, the interaction space and time are reduced. However, as shown in Figure 6.2, the cooling remains efficient. For example, atoms starting with a velocity along the cavity axis of $15\,\mathrm{m\,s^{-1}}$ reach the end of the push stage with approximately $1.3\,\mathrm{m\,s^{-1}}$.

In the Electron-shelving cooling setup, the counter-propagating beam relative to the push beam is the velocity-selective optical pumping and storage beam, referred to as the *storage stage*. The push and storage beams are spatially overlapped, but not temporally.

A disadvantage of the electron-shelving cooling is that it only makes use of atoms that are initially close to zero velocity or counter-propagating the push beam along the cavity axis. However, this challenge can be partially solved. A conceptually simple way would be to tilt the oven nozzle. We didn't choose this method, as it would require a modification of the vacuum setup. Instead, an additional blue beam is introduced, referred to as the pre-collimation beam. This beam is placed just after the oven heating shield and propagates in the opposite direction of the push beam. The pre-collimation beam is constantly on, and its role is to shift the atomic distribution by

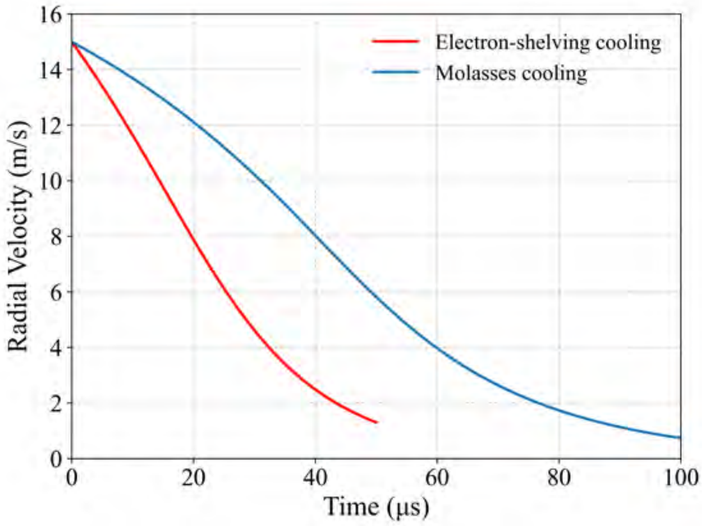

FIGURE 6.2: Comparison between the optical molasses and the electron-shelving cooling. The change in radial velocity after the push stage is calculated based on a vertical velocity of $400\,\mathrm{m\,s^{-1}}$, an initial radial velocity of $15.25\,\mathrm{m\,s^{-1}}$, and a push beam intensity of $2.5I_s$. The red curve represents the velocity over time using the new cooling configuration, while the blue curve shows to change in velocity experienced by the atom under the optical molasses configuration, using the same parameters as stated above for each molasses beam. The electron-shelving cooling demonstrates greater effectiveness, reducing the radial velocity of the atoms to $2\,\mathrm{m\,s^{-1}}$ in less than $40\,\mathrm{\mu s}$, whereas the standard molasses requires more than $60\,\mathrm{\mu s}$ to achieve the same result.

frequency (velocity) after the oven, allowing a larger number of atoms to interact with the push beam.

In the next chapter, the continuous amplification of a $689\,\mathrm{nm}$ seeding beam coupled to the cavity TM00 mode will be discussed in detail. For simplicity, this amplification is also referred to as optical gain and serves as both a diagnostic tool and an optimization parameter for the apparatus, providing insights into the atoms in the upper lasing state.

To determine the optimal frequency and duty cycle, these parameters were systematically scanned while measuring the gain response. The resulting data are presented in Figure 6.3. For this dataset, the oven temperature was maintained at $813\,°\mathrm{K}$ and the intensity of the seed beam was kept at $1\,\mathrm{mW\,cm^{-2}}$ to ensure a good SNR. The power used for all other beams was optimized beforehand using the FM spectroscopy

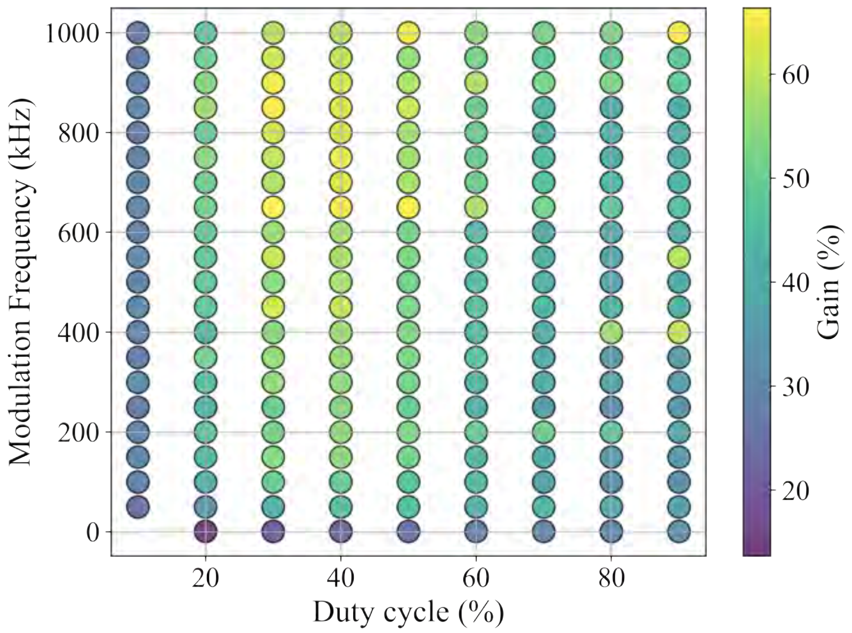

FIGURE 6.3: Scan of the parameter space for the electron-shelving cooling as a function of atomic optical gain.

method, presented in chapter 5. The $688\,\mathrm{nm}$ light remained on throughout the sequence with an intensity of $13.75\,\mathrm{mW\,cm^{-2}}$, while the $689\,\mathrm{nm}$ light alternated with the $461\,\mathrm{nm}$ beam, with respective intensities of approximately $145\,\mathrm{mW\,cm^{-2}}$ and $223\,\mathrm{mW\,cm^{-2}}$, respectively. A duty cycle of 10% means that the storage beam is on for 10% of the corresponding modulation period, while the remaining 90% corresponds to the push beam being active.

Figure 6.3 shows the gain in dependence of modulation frequency and duty cycle. We can identify a region of high gain for duty cycles between 30% and 40%, and within the frequency range of $500\,\mathrm{kHz}$ to $950\,\mathrm{kHz}$. For this dataset, the highest gain observed was 66.4% in $650\,\mathrm{kHz}$ with a duty cycle of 30%. However, it was later observed that when operating with a lower seed beam intensity, on the order of nW, the optimal parameters shift to $500\,\mathrm{kHz}$ and a duty cycle 40%.

Chapter 7

Continuous light amplification

The primary objective of the construction of the apparatus is to achieve continuous emission of light from Sr atoms on the $^1S_0$-$^3P_1$ transition. In the process of pursuing this goal, it is necessary to verify whether excited atoms are interacting with the cavity mode. To quantify this interaction, a π-polarized seed beam is coupled to the resonant cavity mode, and the atomic response is observed through the transmitted light. When most of the atoms that enter the cavity mode are in the $^3P_1$ state, an amplification of the output signal compared to the input signal is observed, called optical gain. In this section, two different approaches are presented to quantify this mechanism.

7.1 A simple picture

The optical gain obtained in the experimental setup can be understood as analogous to injection locking in lasers, a widely known and used frequency stabilizing technique [29, 51, 52, 53]. In this process, a laser beam from a source is injected into a gain medium. Once some conditions are met, such as optical mode matching and sufficient injection power, the gain medium acts as an amplifier for its seeding source.

In the setup presented here, the gain medium is not a conventional laser diode but rather an atomic beam traveling through an optical cavity. The cavity serves as an enhancement mechanism, allowing the atoms to interact with the injected (seeding) light multiple times.

A method of quantifying the optical gain is to compare the atomic signal to the bare cavity response. To achieve this, the atoms are initially stored in metastable states $^3P_{0,2}$, so they do not interact with the seed $689\,\mathrm{nm}$ light while it is scanned through the cavity resonance. The transmitted signal, I_0, is recorded using an APD and is used as a reference as well as a normalization signal, represented as gray circles in Figure 7.1.

Alternatively, the atomic beam can be prepared in the upper lasing state by applying the storage, cleaning, and excitation stages to populate the $^3P_1, m_j = 0$ state.

The cavity transmission for the inverted atomic sample I_e reveals the presence of optical gain. The relative gain is defined as $(I_e - I_0)/I_0$. A relative gain of 443.25% is observed for an intracavity seeding intensity of $0.01I_s$ and a oven temperature of $818\,°\mathrm{K}$. The fit indicate the excited-state transmission has a linewidth of $1.7(7)\,\mathrm{MHz}$ revealing a narrowing in the transmitted spectrum.

This type of gain measurement also provides an effective method for real-time monitoring of the quantity of atoms in the upper lasing state. This approach is one of the primary tools for optimizing the experimental apparatus, such as cooling parameters, e.g., duty cycle and frequency, as presented in Figure 6.3.

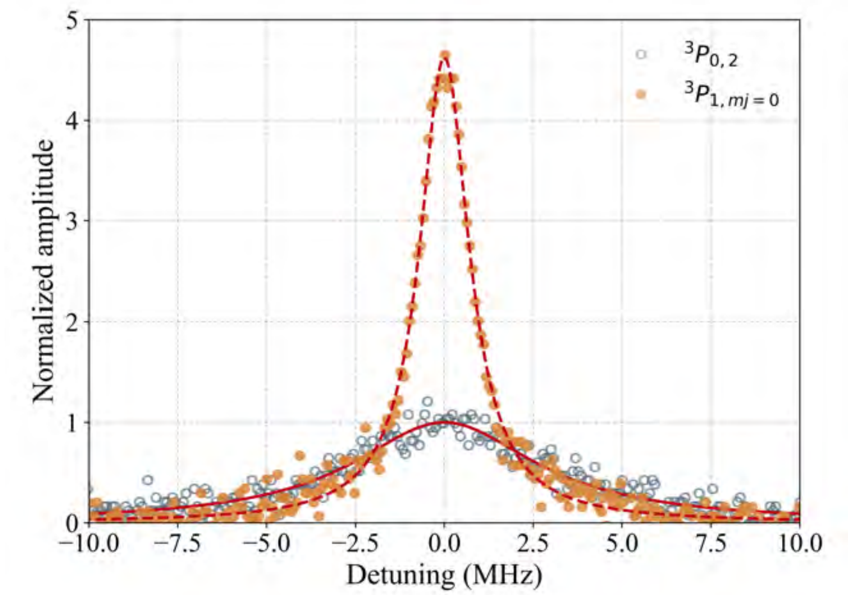

FIGURE 7.1: Amplification of $689\,\mathrm{nm}$ light by atoms interacting with the cavity field. Empty gray circles represent the empty cavity signal, while the orange dots corresponds to atoms arriving in the cavity mode while in the upper lasing state $^3P_1, m_j = 0$. The transmitted signals are normalized by the maximum amplitude of the empty cavity signal.

7.2 Transient overshoot in amplified signal

To explore the system's response under different conditions, particularly for low optical signals below 1 nW, we implement a separate detection method capable of resolving these weak signals.

For amplitudes below 1 nW, the signal is below the noise level of the APD, making direct detection difficult. To overcome this issue, an experimental sequence is implemented in a way that can be repeated up to thousands of times while the time trace of the detected signal is averaged using an oscilloscope to record the data.

As a debugging tool for the system, we use a time sequence in which the excitations and seed beams can be turned on and off in a controlled and repeated manner, either synchronized or independently. This also gives another method for detecting and quantifying the atomic amplification of seed light.

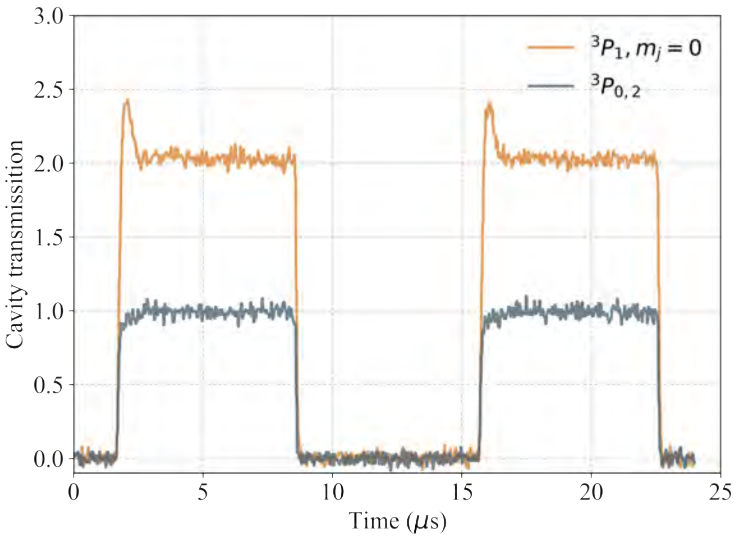

FIGURE 7.2: Transient overshoot in the amplification signal. For the orange data, the seed beam is time-modulated while the excitation beam remains on, ensuring that atoms are transferred to the upper lasing state before entering the cavity volume. For the gray data, the seed beam remains modulated while the excitation beam is off, so the atoms cross the cavity while in the $^3P_{0,2}$ states. Both curves are normalized to the maximum amplitude of the gray curve.

To investigate this behavior, we apply a synchronized temporal modulation to both the excitation and seed beams. This leads to an unexpected and intriguing result: an overshoot in amplitude at the onset of modulation when the atoms are in the excited state. This effect is illustrated in Figure 7.2, with the orange curve. For comparison, the gray curve represents the transmission when probing atoms in the metastable $^3P_{0,2}$ states, where the excitation beam is turned off. This serves as a reference to quantify the amplification achieved when the atoms are prepared in the upper lasing state.

The data in the figure shows that the number of cavity photons approximately doubles when the excitation beam is applied, compared to when the atoms are in the $^3P_{0,2}$ states. Since the intensity of the light exiting the cavity is directly proportional to the number of photons inside, the observed increase in photon count must be attributed to the emission from the $^3P_1$ atoms.

A possible explanation for the overshoot, as illustrated in Figure **??**, is that initially, the cavity mode is fully populated with atoms in the excited state, which have a high probability of emitting photons. However, once the system reaches a steady state, the atoms at the top of the cavity mode have already had significant opportunities to emit photons. Consequently, the $^3P_1$ population in the cavity mode decreases, leading to a reduction in the available gain. In Sec. 7.4.9, we present a simulation of light amplification that accurately reproduces this overshoot behavior.

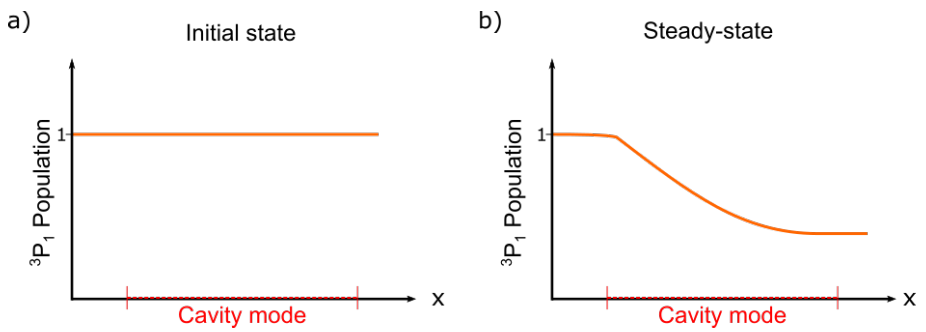

FIGURE 7.3: Representation of the atomic population in the cavity mode along the vertical direction (x-axis) during the gain overshoot behavior (a) and during steady-state gain (b).

A subtle aspect of this measurement is that some atoms may decay from $^3P_1$ to $^1S_0$ before entering the cavity mode, and these atoms will absorb photons. As a result, the additional photons provide insight into the number of atoms in the $^3P_1$ state, minus the number of atoms that have decayed to the $^1S_0$ state due to the excitation beam.

Another subtlety in this measurement is that the initial preparation of atoms in the $^3P_{0,2}$ states may not be perfect. Some atoms will remain in the $^1S_0$ state and will initially absorb photons from the cavity mode. However, if these atoms have a high velocity along the cavity axis, they will quickly move to a neighboring antinode, where their dipole is 180 degrees out of phase with the field, leading to the reemission of the photon. As a result, these atoms should, on average, not change the number of photons in the cavity. We expect that most atoms remaining in the $^1S_0$ state after the electron-shelving cooling have a high velocity along the cavity axis. To ensure this, we use the blue cleaning beam, which is supposed to accelerate any remaining slow $^1S_0$ atoms. To verify the effectiveness of this process, we compare the transmission of the seed beam through the cavity with the oven at low temperature ($523\,°\mathrm{K}$, essentially no atomic beam) and without the excitation beam. The results are similar, indicating that the preparation stage does not leave a significant number of slow $^1S_0$ atoms in the atomic beam entering the cavity mode.

7.3 Estimation of lasing threshold

The goal of our experiment is not merely to amplify light, but to achieve lasing. To estimate how close we are to the lasing threshold, we can use amplification data, such as the one shown in Figure 7.2. To determine this threshold, we first consider that the atoms contribute photons to the cavity mode, driven by the photons already present in that mode. Importantly, the atoms do not distinguish between photons originating from the seed field or those emitted by previously excited atoms. A key assumption in this model is that, for a given total number of photons in the cavity, the fraction of a photon contributed by a single atom remains constant, regardless of the photon's origin. Additionally, the number of photons added by the atoms is directly proportional to the number of atoms present in the cavity.

For the amplification shown in Figure 7.2, half of the cavity photons come from the seed and half from $^3P_1$ atoms. Now, consider a scenario where the total number of photons in the cavity mode is kept constant by simultaneously reducing the seed power while increasing the atomic flux appropriately. To arrive at the lasing threshold, all photons originally provided by the seed have to come from $^3P_1$ atoms and no photons should come from the seed. For the situation of Figure 7.2, this means the number of photons coming from the atoms has to double, i.e. approximately twice as many atoms are required to sustain the given photon number in the absence of any seed field. If the atomic flux is increased slightly beyond this threshold, the number of photons in the cavity increases, leading to an enhancement in the fraction of photons contributed per atom, ultimately resulting in the onset of lasing. This threshold is inherently unstable: A slight reduction in the number of atoms leads to a collapse of the lasing process, whereas a small increase results in a quadratic enhancement of the photon number.

We here define gain as $g = P_a/P_s$, where P_s represents the number of cavity photons originating from the seed (blue region in the signal) and P_a denotes the number of photons contributed by the atoms (orange data). Since the emission from the atoms is stimulated by the total intracavity photon number $P_s + P_a$, we assume that P_a increases linearly with the atomic flux if P_s is reduced such that the total intracavity photon number remains constant. Experimentally we would simply keep the light intensity coming out of the cavity constant, as this intensity is proportional to the intracavity photon number.

If all seed photons P_s are replaced by additional photons P_a from the atoms, the system reaches the lasing threshold, meaning the atoms alone sustain the intracavity field. To be more precise, the effective gain is provided by the difference in atoms in $^3P_1$ and $^1S_0$. Therefore, to reach the lasing threshold, the population difference between the excited state N_e and the ground state N_g has to be increased by:

$$m = \frac{P_s + P_a}{P_a} = 1 + \frac{P_s}{P_a} = 1 + \frac{1}{g}, \tag{7.1}$$

where P_s and P_a are taken from a gain measurement. For the data presented above, we find $m = 1.84$. However, the highest gain observed in the system is $g = 4.43$, for which $m = 1.23$. This suggests that we are, at most, a small factor away from achieving lasing in terms of N_e - N_g . A further reduction in the decoherence mechanisms could bring the system even closer to the lasing threshold.

7.4 A mean-field approach

Our theory collaborator Simon B. Jäger developed a mean-field description of the apparatus to analyze the emission [54, 55, 56, 57, 58]. This theoretical framework will be presented here for a more in-depth discussion. In addition, a code based on the theory outlined in the following, developed by him, was used to simulate the behavior observed in the apparatus.

First, it is assumed that the atomic ensemble has a homogeneous density distribution and that the atoms move ballistically across the waist of the driven optical cavity. The laser frequency is given by ω_L and the cavity-laser detuning is defined as $\Delta_c = \omega_c - \omega_L$, while the atom-laser detuning is given by $\Delta_a = \omega_a - \omega_L$. The cavity mode function is represented by $\eta(\mathbf{x})$, and g denotes the cavity vacuum Rabi frequency at the maximum of its mode. Additionally, Ω represents the Rabi frequency of the laser that drives the cavity. Considering the Hamiltonian for the atom-cavity interaction in the rotating frame

$$\hat{H} = \sum_j \left[\frac{\hat{\mathbf{p}}^2}{2m} + \hbar\Delta_a \hat{\sigma}_j^+ \hat{\sigma}_j^- + \frac{\hbar g}{2}\eta(\hat{\mathbf{x}}_j)(\hat{a}^\dagger \hat{\sigma}_j^- + \hat{\sigma}_j^+ \hat{a}) \right] + \hbar\Delta_c \hat{a}^\dagger \hat{a} + \frac{\Omega}{2}(\hat{a}^\dagger + \hat{a}), \tag{7.2}$$

with the first term on the left-hand side describing the kinetic energy, where $\sum_j$ runs over all atoms in the beam and $\hat{\mathbf{p}}_j$ is the momentum operator. The operators $\hat{\sigma}_j^{+(-)}$ represent the atomic raising (lowering) operators, which describe the internal energy of the atoms relative to the driving laser. The coupling of the cavity to the atoms is evaluated at the position operator $\hat{\mathbf{x}}_j$. The annihilation (creation) operators of the cavity field are denoted by $\hat{a}^{(\dagger)}$.

The cavity linewidth, κ, is also introduced, and the following master equation describes the dynamics of the atoms and the cavity:

$$\frac{\partial \hat{\rho}}{\partial t} = \frac{1}{i\hbar}\left[\hat{H}, \hat{\rho}\right] - \frac{\kappa}{2}(\hat{a}^\dagger \hat{a}\hat{\rho} + \hat{\rho}\hat{a}^\dagger \hat{a} - 2\hat{a}\hat{\rho}\hat{a}^\dagger), \tag{7.3}$$

where the second term describes the cavity photon loss. To simulate the dynamics governed by the master equation, first, the Heinsenberg-Langevin equations are derived and then used as semiclassical analogs, which are

$$\frac{d\alpha}{dt} = -\left(i\Delta_c + \frac{\kappa}{2}\right)\alpha - i\frac{g}{2}J - i\frac{\Omega}{2} + \sqrt{\kappa}\mathcal{N}, \tag{7.4}$$

$$\frac{ds_j}{dt} = -i\Delta_a s_j + \frac{ig}{2}\eta(\mathbf{x})s_j^z \alpha, \tag{7.5}$$

$$\frac{ds_j^z}{dt} = ig\eta(\mathbf{x})(\alpha^* s_j - s_j^* \alpha), \tag{7.6}$$

$$\frac{dx_j}{dt} = \frac{p_j}{m}. \tag{7.7}$$

The quantum operators $\hat{\sigma}_j$, $\hat{\sigma}_j^z$, and $\hat{a}$ are replaced by the classical spin components s_j and s_j^z, and the field α. Additionally, classical noise is introduced as $\mathcal{N}$. The collective dipole is given by

$$J = \sum_j \eta(\mathbf{x}_j) s_j. \tag{7.8}$$

7.4.1 Mean-field equations

By considering the mean-field theory, we disregard all the noise terms in equation (7.4). We solve the dynamical equation for the atom and spin densities

$$f = \sum_j \delta(\mathbf{x} - \mathbf{x}_j)\delta(\mathbf{p} - \mathbf{p}_j), \tag{7.9}$$

$$s = \sum_j s_j \delta(\mathbf{x} - \mathbf{x}_j)\delta(\mathbf{p} - \mathbf{p}_j), \tag{7.10}$$

$$s^z = \sum_j^z \delta(\mathbf{x} - \mathbf{x}_j)\delta(\mathbf{p} - \mathbf{p}_j), \tag{7.11}$$

which leads to

$$\frac{d\alpha}{dt} = -\left(i\Delta_c + \frac{\kappa}{2}\right)\alpha - i\frac{g}{2}J - i\frac{\Omega}{2}, \tag{7.12}$$

$$\frac{\partial s}{\partial t} + \frac{\mathbf{p}}{m} \cdot \nabla_x s = -i\Delta_a s + \frac{ig}{2}\eta(\mathbf{x}) s^z \alpha, \tag{7.13}$$

$$\frac{\partial s^z}{\partial t} + \frac{\mathbf{p}}{m} \cdot \nabla_{\mathbf{x}} s^z = ig\eta(\mathbf{x}(\alpha^* s - s^* \alpha), \tag{7.14}$$

$$\frac{\partial f}{\partial f} + \frac{\mathbf{p}}{m} \cdot \nabla_{\mathbf{x}} f = 0. \tag{7.15}$$

Using the density formalism, the collective dipole is expressed as

$$J = \int d\mathbf{x} \int d\mathbf{p}\eta(\mathbf{x})s(\mathbf{x}, \mathbf{p}). \tag{7.16}$$

It is commonly assumed that the distribution function f is homogeneous in space and time-independent. Under this assumption, equation (7.15) is automatically satisfied.

7.4.2 Adiabatic elimination of the cavity

We consider the regime where the cavity linewidth κ is larger than any other frequency in the model. Under this condition, the cavity field can be adiabatically eliminated, yielding

$$\alpha = -i\left[\frac{\Omega_c}{g} + \frac{\Gamma_c J}{g}\right]\cos(\chi_c)e^{-i\chi_c}. \tag{7.17}$$

Here, the following parameters are used.

$$\Gamma_c = \frac{g^2}{\kappa}, \tag{7.18}$$

$$\Omega_c = \frac{g\Omega}{\kappa}, \tag{7.19}$$

and

$$\tan(\chi_c) = \frac{\Delta_c}{\kappa/2}, \tag{7.20}$$

$$\cos(\chi_c) = \frac{1}{\sqrt{1 + \left[\frac{\Delta_c}{\kappa/2}\right]^2}}. \tag{7.21}$$

7.4.3 Stationary solution

Now, the stationary solution is derived to describe the mean-field behaviour of the atoms at long timescales. To aid in this process, we define the conserved quantity.

$$\frac{d}{dt}\left[(s^z)^2 + 4|s|^2\right] = 0, \tag{7.22}$$

with

$$\frac{d}{dt} = \frac{\partial}{\partial t} + \frac{\mathbf{p}}{m}\frac{\partial}{\partial x}. \tag{7.23}$$

Equation (7.22) comes from the fact that we do not include spontaneous emission or additional dephasing of the dipoles. This means that the individual dipoles all point to the Bloch sphere surface. The equation represents the conservation of the individual spin length.

Now, a parameterization is taken:

$$s^z = s_0^z \cos(K), \tag{7.24}$$

$$s = \frac{s_0^z}{2}\sin(K)e^{-i\psi}, \tag{7.25}$$

where s_0^z represents a momentum-dependent measure of coherence introduced into the cavity, and ψ denotes a phase that depends on position, momentum, and time. Using the dynamical equation for s, the differential equations for K and ψ can be derived and are expressed as

$$\frac{dK}{dt} = g\alpha_0\eta(\mathbf{x})\cos(\psi - \phi), \tag{7.26}$$

$$\frac{d\psi}{dt} = \Delta_a - g\alpha_0\eta(\mathbf{x})\cot(K)\sin(\psi - \phi), \tag{7.27}$$

where we used

$$\alpha = -i\alpha_0 e^{-i\phi}, \tag{7.28}$$

with $\alpha_0 \in \mathbb{R}$. It is possible to define

$$\Psi = \sin(K)\sin(\psi - \phi), \tag{7.29}$$

which results in

$$\frac{d\Psi}{dt} = \Delta_a \sin(K)\cos(\psi - \phi). \tag{7.30}$$

With these definitions and equation (7.17), one can derive

$$g\alpha_0 = [\Omega_c + \Gamma_c J]\cos(\chi_c)e^{i(\phi-\chi_c)} \tag{7.31}$$

$$= \Omega_c \cos(\chi_c)e^{i(\phi-\chi_c)} + \frac{\Gamma_c \cos(\chi_c)}{2}\int d\mathbf{x}\int d\mathbf{p}\eta(\mathbf{x})s_0^z \sin(K)e^{i(\phi-\chi_c-\psi)}. \tag{7.32}$$

From the above, two more equations are derived:

$$g\alpha_0 = \Omega_c \cos(\phi) + \frac{\Gamma_c}{2g\alpha_0}\int d\mathbf{x}\int d\mathbf{p}\frac{dK}{dt}s_0^z \sin(K), \tag{7.33}$$

$$g\alpha_0 \tan(\chi_c) = \Omega_c \sin(\phi) - \frac{\Gamma_c}{2}\int d\mathbf{x}\int d\mathbf{p}\eta(\mathbf{x})s_0^z\Psi. \tag{7.34}$$

Now the challenge lies in finding $g\alpha_0$ and ϕ self-consistently such that the two equations above, along with Eqs. (7.26) and (7.27), are satisfied.

7.4.4 A realistic model approach

We now consider the momentum distribution

$$f(p_x, p_z) = f_x(p_x)f_z(p_z), \tag{7.35}$$

$$f_x(p_x) = \frac{\beta_x p_x}{m}e^{-\beta_x\frac{p_x^2}{2m}}, \tag{7.36}$$

$$f_z(p_z) = \sqrt{\frac{\beta_z}{2\pi m}}e^{-\beta_z\frac{p_z^2}{2m}}, \tag{7.37}$$

and assume a homogeneous distribution in position. Additionally, we consider a Gaussian beam profile and a standing-wave cavity mode.

$$\eta(\mathbf{x}) = \cos(kz)e^{-\frac{x^2}{w^2}}. \tag{7.38}$$

7.4.5 Relevant physical quantities

Several important physical quantities are defined using this mode profile and velocity distribution. Previously, the waist of the cavity beam w, the wave number $k = 2\pi/\lambda$, and the temperatures $1/\beta_x$ (along the atomic beam) and $1/\beta_z$ (along the cavity axis) were introduced. It is assumed that $\beta_x \neq \beta_z$ due to the nozzle distribution and the cooling and preparation process. The Doppler width δ_D, defined along the cavity axis z, is expressed as

$$\delta_D = \frac{k\sqrt{\langle p_z^2\rangle}}{m} = \sqrt{\frac{k^2}{m\beta_z}}. \tag{7.39}$$

Another important quantity is the mean velocity $\bar{v}$ of the atoms along the beam direction x, defined as

$$\bar{v}_x = \frac{\langle p_x\rangle}{m} = \sqrt{\frac{\pi}{2m\beta_x}},. \tag{7.40}$$

With the above expression, the transit time is defined as

$$\tau = \frac{2w}{\bar{v}_x} = \sqrt{\frac{8w^2 m\beta_x}{\pi}}. \tag{7.41}$$

It is now possible to express the Doppler width in terms of inverse transit time

$$\delta_D\tau = \sqrt{\frac{32\pi w^2}{\lambda^2}\frac{\beta_x}{\beta_z}}. \tag{7.42}$$

For $\beta_x = \beta_z$, $\delta_D\tau$ is found to become independent of β but remains dependent on kw.

7.4.6 The zero detuning result

The resonant case, where $\Delta_c = \Delta_a = 0$, is now considered. As a consequence, $\psi = 0$ and $\phi = 0$. The objective is to calculate the collective dipole, given by

$$J = \int d\mathbf{x} \int d\mathbf{p}\, \eta(\mathbf{x}) \frac{s_0^z}{2} \sin(K), \tag{7.43}$$

which can subsequently be used to calculate the cavity field. This is achieved by integrating

$$\frac{dK}{dt} = g\alpha_0 \eta(\mathbf{x}). \tag{7.44}$$

By explicitly defining $K(t) = K\left[\frac{p_x}{m}t, z_0 + \frac{p_z}{m}t\right]$, one obtains

$$\frac{dK(t)}{dt} = g\alpha_0 \cos\left[kz_0 + \frac{kp_z}{m}t\right] e^{-\frac{p_x^2 t^2}{m^2 w^2}}. \tag{7.45}$$

Integrating this equation gives

$$K(x, z, p_x, p_z) = g\alpha_0 \int_{-\infty}^{t} dt' \, \cos\left[kz_0 + \frac{kp_z}{m}t'\right] e^{-\frac{p_x^2 (t')^2}{m^2 w^2}} \tag{7.46}$$

$$= \frac{g\alpha_0 m}{p_x} \int_{-\infty}^{x} du \, \cos\left[kz_0 + \frac{kp_z}{p_x}u\right] e^{-\frac{u^2}{w^2}} \tag{7.47}$$

$$= \frac{g\alpha_0 m}{p_x} \int_{-\infty}^{x} du \, \cos\left[kz - \frac{kp_z}{p_x}(x-u)\right] e^{-\frac{u^2}{w^2}}. \tag{7.48}$$

We now determine the collective dipole

$$J = \int_0^{\lambda} dz \int_0^{\infty} dp_x \int_{-\infty}^{\infty} dp_z \frac{p_x}{m} \frac{s_0^z}{2g\alpha_0} \left[1 - \cos[K(\infty, z, p_x p_z)]\right], \tag{7.49}$$

where we use

$$K(\infty, z, p_x p_z) = \frac{g\alpha_0 m}{p_x} \int_{-\infty}^{\infty} du \, \cos\left[kz - \frac{kp_z}{p_x}(x-u)\right] e^{-\frac{u^2}{w^2}} \tag{7.50}$$

$$= \frac{g\alpha_0 m}{p_x} \int_{-\infty}^{\infty} du \, \cos\left[kz - \frac{kp_z}{p_x}x\right] \cos\left[\frac{kp_z}{p_x}u\right] e^{-\frac{u^2}{w^2}} \tag{7.51}$$

$$= \frac{g\alpha_0 m}{p_x} \sqrt{\pi w^2} \cos\left[kz - \frac{kp_z}{p_x}x\right] e^{-\frac{k^2 w^2 p_z^2}{4p_x^2}} \tag{7.52}$$

This leads to

$$J = \int_0^{\lambda} dz \int_0^{\infty} dp_x \int_{-\infty}^{\infty} dp_z \frac{p_x}{m} \frac{s_0^z}{2g\alpha_0} \left[1 - \cos\left(\frac{g\alpha_0 m}{p_x}\sqrt{\pi w^2} \cos\left[kz - \frac{kp_z}{p_x}x\right] e^{-\frac{k^2 w^2 p_z^2}{4p_x^2}}\right)\right] \tag{7.53}$$

$$= \lambda \int_0^{\infty} dp_x \int_{-\infty}^{\infty} dp_z \frac{p_x}{m} \frac{s_0^z}{2g\alpha_0} \left[1 - \mathcal{J}_0\left(\frac{g\alpha_0 m}{p_x}\sqrt{\pi w^2} e^{-\frac{k^2 w^2 p_z^2}{4p_x^2}}\right)\right]. \tag{7.54}$$

Now,

$$s_0^z = \frac{D}{\lambda} \rho_z \sqrt{\frac{\beta_z}{2\pi m}} e^{-\beta_z \frac{p_z^2}{2m}} \frac{\beta_x p_x}{m} e^{-\beta_x \frac{p_x^2}{2m}} \tag{7.55}$$

where D is the diameter of the atomic beam and

$$\rho_z = \frac{Z}{2wD}, \tag{7.56}$$

where $Z = N_e - N_g$ is the difference between the number of atoms N_e in the excited state and the number N_g of atoms in the ground state that are interacting with the cavity.

We can now substitute $p_x = \sqrt{m/\beta_x} u_x$ and $p_z = \sqrt{m/\beta_z} u_z$, and use the definitions in Eqs. (7.41),(7.42) and (7.56) to arrive at

$$J = Z \int_{-\infty}^{\infty} du_z \frac{1}{\sqrt{2\pi}} e^{-\frac{u_z^2}{2}} \int_0^{\infty} du_x \frac{u_x^2}{\sqrt{2\pi}} e^{-\frac{u_x^2}{2}} \frac{1}{g\alpha_0 \tau} \left[1 - \mathcal{J}_0 \left(\sqrt{\frac{\pi^2}{8}} g\alpha_0 \tau \frac{1}{u_x} e^{-\frac{\pi}{32}(\delta_D \tau)^2 \frac{u_z^2}{u_x^2}} \right) \right]. \tag{7.57}$$

This result depends on α_0, and therefore, it is needed to self-consistently solve the equation

$$g\alpha_0 = \Omega_c + \Gamma_c J. \tag{7.58}$$

7.4.7 The low-intensity limit

For the low-intensity case, it is possible to expand the Bessel functions as $J_0(x) \approx 1 - \frac{x^2}{4}$, yielding

$$g\alpha_0 \approx \Omega_c + \Gamma_c Z \int_{-\infty}^{\infty} du_z \frac{1}{\sqrt{2\pi}} e^{-\frac{u_z^2}{2}} \int_0^{\infty} du_x \frac{u_x^2}{\sqrt{2\pi}} e^{-\frac{u_x^2}{2}} \frac{1}{4 g\alpha_0 \tau} \left[\sqrt{\frac{\pi^2}{8}} g\alpha_0 \tau \frac{1}{u_x} e^{-\frac{\pi}{32}(\delta_D \tau)^2 \frac{u_z^2}{u_x^2}} \right]^2 \tag{7.59}$$

$$= \Omega_c + \frac{Z\Gamma_c \pi}{64} (g\alpha_0 \tau) \int_0^{\infty} du_x \sqrt{\frac{2\pi u_x^2}{u_x^2 + \frac{\pi(\delta_D \tau)^2}{8}}} e^{-\frac{u_x^2}{2}} \tag{7.60}$$

With that, Eqn. (7.58) takes the form

$$g\alpha_0 \tau = \frac{\Omega_c \tau}{1 - \frac{Z}{N_c}} \tag{7.61}$$

with

$$N_c^{-1} = \frac{\Gamma_c \tau \pi}{64} \int_0^{\infty} du_x \sqrt{\frac{2\pi u_x^2}{u_x^2 + \frac{\pi(\delta_D \tau)^2}{8}}} e^{-\frac{u_x^2}{2}}. \tag{7.62}$$

N_c represents the critical atom number above which the system is lasing, if the inversion is perfect. For a small Doppler width, $\delta_D \tau \ll 1$, this simplifies to

$$N_c^{-1} \approx \frac{\Gamma_c \tau \pi}{64} \int_0^{\infty} du_x \sqrt{2\pi} e^{-\frac{u_x^2}{2}} = \frac{\Gamma_c \tau \pi^2}{64}. \tag{7.63}$$

For a large Doppler width, $\delta_D\tau \gg 1$, one gets

$$N_c^{-1} \approx \frac{\Gamma_c\pi}{16\delta_D}\int_0^\infty du_x u_x e^{-\frac{u_x^2}{2}} = \frac{\Gamma_c\pi}{16\delta_D}. \tag{7.64}$$

Equation(7.61) has different implications depending on the state of the incoming atoms, and therefore depends on Z.

7.4.8 Emission

If all atoms enter the cavity while in the excited state, then $Z = N_e = N$. In this case, one should expect to observe an enhanced cavity field

$$g\alpha_0\tau = \frac{\Omega_c\tau}{1-\frac{N}{N_c}}. \tag{7.65}$$

The gain is then given by

$$\frac{\Delta I_{\mathrm{em}}}{I} = \frac{(g\alpha_0\tau)^2-(\Omega_c\tau)^2}{(\Omega_c\tau)^2} = \frac{1-\left[1-\frac{N}{N_c}\right]^2}{\left[1-\frac{N}{N_c}\right]^2}. \tag{7.66}$$

This quantity diverges at $N = N_c$, marking the breakdown of the low-intensity approximation and the onset of a lasing phase. Thus, the lasing threshold is identified, which is given by

$$1 = \frac{N}{N_c} = \frac{N\Gamma_c\tau\pi}{64}\int_0^\infty du_x\sqrt{\frac{2\pi u_x^2}{u_x^2+\frac{\pi(\delta_D\tau)^2}{8}}}e^{-\frac{u_x^2}{2}}. \tag{7.67}$$

7.4.9 Simulating the overshoot behavior

Based on his theoretical framework, Simon also developed a computational model that successfully reproduces the overshoot behavior, as shown in Figure 7.4. For this simulation, a population of 4×10^4 atoms was used, entering the cavity mode fully inverted with a velocity of $300\,\mathrm{m\,s^{-1}}$ and a Doppler broadening along the cavity axis of $2\,\mathrm{MHz}$. The cavity parameters used are presented in Table 4.1.

It is also worth noting that after the seed light (blue curve) is turned off, a slow decay of the emission is observed in the simulation, whereas this behavior is not seen

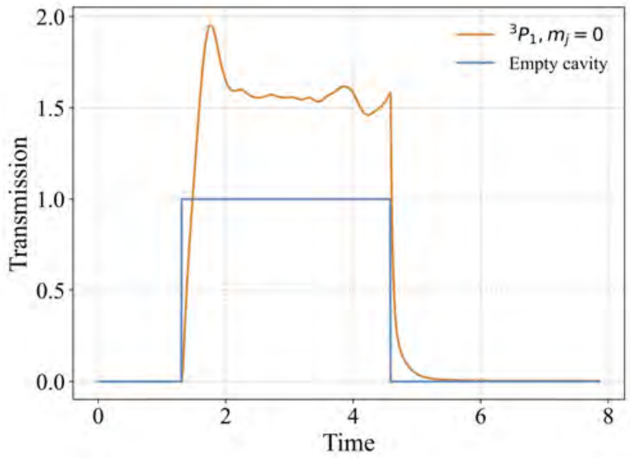

FIGURE 7.4: Simulation of the overshoot behavior. The orange line represents the amplified signal for atoms entering the cavity in the $^3P_{1,m_j=0}$ state, while the blue curve represents the seeding light without atoms in the cavity. Both signals are normalized by the maximum amplitude of the blue data.

experimentally. By incorporating experimental parameters into the model—such as a vertical atomic velocity of $\sim 400\,\mathrm{m\,s^{-1}}$ and an excited population of 4.5×10^4, corresponding to an excitation efficiency of 50%, and a Doppler broadening along the cavity axis of $2\,\mathrm{MHz}$ it is found that after the seeding beam is turned off a lasing signal is present and persists.

This provides important insights into the experiment: the absence of this emission in the actual measurements could indicate a low excitation efficiency or significant Doppler broadening along the cavity axis. Specifically, increasing the Doppler broadening from $2\,\mathrm{MHz}$ to $5\,\mathrm{MHz}$ in the simulation causes the lasing emission to disappear, while the overshoot remains present but with an increased duration. This suggests that Doppler broadening could be a significant limiting factor in the experimental setup, acting as a major source of decoherence that still needs to be mitigated.

Chapter 8

The atomic emission onset

After observing the overshoot behavior, the next step is to investigate the atomic signal in the upper lasing state without the presence of seeding light. The experimental sequence remains the same as described in the previous chapter, allowing for temporal modulation of the excitation beam. To enhance the SNR the sequence is repeated multiple times, and the data is averaged before being retrieved from the oscilloscope.

The first observable signal appeared after adjusting the detuning of the $688\,\mathrm{nm}$ light, which is part of the excitation beam, to $-4\,\mathrm{MHz}$. In this configuration, an emission pulse from the atoms is detected just after the start of the excitation pulse. However, increasing the active time of the excitation beam did not extend the emission duration, presenting a challenging puzzle to be understood.

In Figure 8.1 a), exponential fits are plotted as visual guides for both the rising and decaying parts of the emission pulse. The rising fit (blue) shows good agreement with the data, yielding a characteristic time of $25.1\,\mathrm{ns}$. The emission onset occurs approximately $84\,\mathrm{ns}$ after the start of the excitation beam. Considering that the atoms have a vertical velocity of $400\,\mathrm{m\,s^{-1}}$, during the delay time the atoms travel upward $33.6\,\mathrm{\mu m}$.

Initially, it was suspected that the delay was related to the vertical position of the excitation beam, which is adjusted using FM spectroscopy. In this scenario, lowering the beam relative to the cavity mode would delay the emission onset, corresponding to the additional time required for the atoms to travel to the cavity. However, this hypothesis was not confirmed experimentally. Instead, it was observed that lowering the excitation beam gradually reduced the pulse intensity until it eventually disappeared, without altering the onset delay time. Conversely, when the beam was moved upwards, the delay time remained unchanged until the pulse was no longer observed. This disappearance happened probably once the excitation beam was too high above the cavity mode, exciting the atoms mostly after they had already passed through the

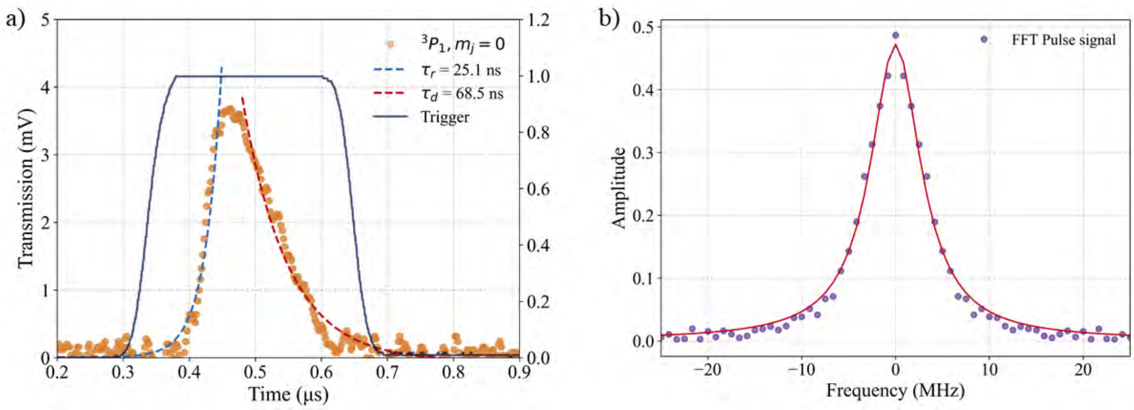

FIGURE 8.1: Onset of atomic emission. (a) Optical pulse in the time domain, where the blue dashed curve represents an exponential rising fit, while the red dashed curve represents an exponential decay. The orange data represents the emission from atoms interacting with the cavity while in the $^3P_1, m_j = 0$ state. The data is averaged over 1125 measurements. (b) Fourier-transformed data for the pulse. The red curve represents a Lorentzian fit of $6.5(5)$ MHz linewidth. For this data the oven was kept at $817.15\,°$K, and cooling method modulation of $500\,$kHz and 40% duty cycle.

cavity. It is important to note that the changes in the height of the excitation beam were less than $1\,$mm and could not be precisely quantified.

Another intriguing riddle is why the pulse ceases despite the continuous supply of atoms. As mentioned, the pulse duration does not increase even when the excitation beam is kept on continuously. Figure 8.1 a) shows the longest pulse typically observed, with a total duration of approximately $200\,$ns. The atomic emission could be shortened to the order of tens of nanoseconds but was never observed to last longer than the duration shown.

Still referring to Figure 8.1 a), the red dashed line represents an exponential decay fit, which serves more as a visual guide rather than an accurate fit, and which has a characteristic decay time of $68.5\,$ns. It is notable that, during the decay phase, certain features resemble relaxation oscillations. However, because of the lack of a theoretical model that describes pulsed emission in such continuously operating system, no definitive conclusions can be drawn at this stage.

It was found that, for the pulses to remain clearly distinguishable in each cycle, the excitation beam needed to be activated for a minimum duration of $1.4\,$μs, followed by an equal duration with the beam turned off. This results in a total interval of $2.8\,$μs between consecutive pulses. Although shorter intervals might be possible, the requirement to average a large number (>100) of pulses to improve the SNR, imposed a practical limit, making this the shortest interval at which the pulses were consistently observed in each cycle.

This raises another question: What type of process occurs that requires approximately $3\,\mu\mathrm{s}$ for the system to recover?

The atoms have a vertical speed of approximately $400\,\mathrm{m\,s^{-1}}$ and travel about $1.2\,\mathrm{mm}$ during the time the excitation beam remains off before the next pulse occurs. Intriguingly, this distance is on the same order as the width of the excitation beam. This suggests that while the excitation beam is off, new ${}^3P_{0,2}$ atoms can fully refill the cavity mode before the excitation beam is switched on again to deliver the next pulse.

It is possible that the observed pulses require a full inversion of all atoms in the cavity mode to ${}^3P_1$ in order to sustain themselves. Referring to Figure 7.3, we can visualize the following: once the system approaches steady state, not all atoms in the cavity remain in ${}^3P_1$. Atoms near the top edge of the cavity will have partially decayed to ${}^1S_0$, reducing the average ${}^3P_1$ population in steady state to approximately half of its initial value immediately after the excitation pulse is switched on. This suggests that the ${}^3P_1$ population may decrease from above to below the lasing threshold as the system transitions from excitation to steady state.

The pulses last approximately $200\,\mathrm{ns}$, during which the atoms travel about $80\,\mu\mathrm{m}$. This displacement is comparable to the size of the cavity mode, further supporting the hypothesis outlined above. Interestingly, the overshoot observed in the gain measurement immediately after switching on the seed has a similar duration to the pulses observed here and may share the same underlying mechanism.

If this hypothesis is correct, achieving steady-state lasing may require increasing $N_e - N_g$ by at most a factor of two. Alternatively, the system may already be above the lasing threshold in steady state, in which case removing a decoherence mechanism, such as stray light, could be necessary. Most likely, a combination of both improvements will be beneficial.

Figure 8.1 b) shows the Fast Fourier Transform (FFT) of the data presented in a). The red line represents a Lorentzian fit, yielding a linewidth of $6.5\,\mathrm{MHz}$. When performing an FFT of an exponential decay with a time constant of $\tau = 65\,\mathrm{ns}$ (as determined above), it results in a peak with a FWHM of $5\,\mathrm{MHz}$. For a Lorentzian spectral line given by

$\propto 1/(1 + (2\Delta/\Gamma)^2)$, the half-maximum is reached at $\Delta = \Gamma/2$, leading to a FWHM of Γ [59], which defines the characteristic width of a resonance.

The $1/e$-lifetime τ of a spontaneously decaying two-level system is related to the resonance width Γ of the same system under weak drive by $\Gamma = 1/\tau$, which for our case gives $\Gamma = 2\pi \times 2.4\,\mathrm{MHz}$. A factor of two differences is observed between this value and the value determined by FFT. However, this is not a contradiction as two distinct phenomena are being compared. In the first case, the frequency width of exponentially decaying radiation after an instantaneous inversion of the gain medium is determined by Fourier transformation. In the second case, the resonance width corresponds to a weakly driven dissipative harmonic oscillator. These two quantities need not be identical.

By performing an FFT on a $200\,\mathrm{ns}$ square pulse, an estimate of the best achievable frequency resolution is obtained, resulting in an FWHM of $4.6\,\mathrm{MHz}$. Instead of using a square pulse, if using the fitted exponential curves of Figure 8.1 a) to approximate the shape of the measured pulse, the FFT yields a width of $4.3\,\mathrm{MHz}$.

Converting the pulse envelope into a Fourier spectrum always provides a lower limit on the actual frequency resolution. This is because the calculation assumes that the sine wave of the emitted electromagnetic radiation is perfect throughout the entire pulse. Essentially, it sets the frequency resolution limit based on the finite duration of the pulse. The actual resolution could be worse if significant phase fluctuations occur during the emission.

However, no definitive conclusions can be drawn regarding the observed emission and its duration. Many promising options exist to make further progress. We can increase the atom flux, reduce the axial velocity of the atoms, improve the efficiency with which the atoms are prepared in the upper lasing state, search for and eliminate potential sources of decoherence and improve our detection efficiency. The last point would also eliminate the need for thousands of measurements to average the signal, a process that may inadvertently wash out potential random pulses.

Chapter 9

Conclusions and outlook

This thesis presents work in which a previously existing experimental apparatus was upgraded, with one of the key components built and characterized by the author. A laser system was developed, with all lasers used in the apparatus being home-built, including the electronics for temperature and current control, as well as the feedback electronics required for laser stabilization. In addition, the electron-shelving cooling method was developed and demonstrated to be effective within the requirements of the apparatus.

All the upgrades made to the apparatus proved to be worthwhile, as they led to results never before observed in this architecture. Compared to its previous version, there was an improvement of at least 40 times in the gain signal at low seeding intensities [27], and, notably, the onset of collective atomic emission was observed in the upper lasing state.

Although several aspects still need to be addressed, particularly those discussed in the last chapter regarding the unknown mechanisms causing the emission to cease, it is important to emphasize that this apparatus is unique. It serves as both a crucial pathfinder and a proof-of-principle experiment toward the realization of continuous superradiance, a phenomenon that has yet to be demonstrated.

Another important feature of this apparatus is its simplicity, as it consists of a single chamber where all stages operate continuously and are spatially separated rather than temporally. Once the apparatus reaches its goal, further engineering could enable the development of a more compact device suitable for field applications, such as probing local gravity [6].

The integration of superradiance into quantum metrology extends beyond time-keeping applications. Superradiant systems can also enhance the sensitivity in interferometric measurements, such as those used in gravitational wave detection or inertial navigation. By reducing quantum noise through collective emission, these systems could enable higher SNRs, pushing the boundaries of precision measurement. Furthermore, such devices could be used for tests of fundamental constants, detection of dark matter, and exploration of physics beyond the Standard Model [60].

Bibliography

[1] W. Markowitz, R. G. Hall, L. Essen, and J. V. L. Parry, *"Frequency of Cesium in Terms of Ephemeris Time"*, Phys. Rev. Lett. **1**, 105–107 (1958) .

[2] R. E. Beehler, R. C. Mockler, and J. M. Richardson, *"Cesium Beam Atomic Time and Frequency Standards"*, Metrologia **1**, 114 (1965) .

[3] W. D. Phillips, *"Nobel Lecture: Laser cooling and trapping of neutral atoms"*, Rev. Mod. Phys. **70**, 721–741 (1998) .

[4] M. H. Anderson, J. R. Ensher, M. R. Matthews, C. E. Wieman, and E. A. Cornell, *"Observation of Bose-Einstein Condensation in a Dilute Atomic Vapor"*, Science **269**, 198–201 (1995) .

[5] A. Aeppli, K. Kim, W. Warfield, M. S. Safronova, and J. Ye, *"Clock with 8×10^{-19} Systematic Uncertainty"*, Phys. Rev. Lett. **133**, 023401 (2024) .

[6] W. F. McGrew, X. Zhang, R. J. Fasano, et al., *"Atomic clock performance enabling geodesy below the centimetre level"*, Nature **564**, 87–90 (2018) .

[7] W. B. Cairncross, D. N. Gresh, M. Grau, K. C. Cossel, T. S. Roussy, Y. Ni, Y. Zhou, J. Ye, E. A. Cornell, et al., *"Precision Measurement of the Electron's Electric Dipole Moment Using Trapped Molecular Ions"*, Phys. Rev. Lett. **119**, 153001 (2017) .

[8] T. Bothwell, C. J. Kennedy, A. Aeppli, et al., *"Resolving the gravitational redshift across a millimetre-scale atomic sample"*, Nature **602**, 420–424 (2022) .

[9] D. Hanneke, S. Fogwell, G. Gabrielse, et al., *"New Measurement of the Electron Magnetic Moment and the Fine Structure Constant"*, Phys. Rev. Lett. **100**, 120801 (2008) .

[10] M. Gross, S. Haroche, et al., *"Superradiance: An essay on the theory of collective spontaneous emission"*, Physics Reports **93**, 301–396 (1982) .

[11] R. H. Dicke et al., *"Coherence in Spontaneous Radiation Processes"*, Phys. Rev. **93**, 99–110 (1954) .

[12] J. Chen et al., *"Active Optical Clock"*, Chin. Sci. Bull. **54**, 348–352 (2009) .

[13] D. A. Steck et al., *"Quantum and Atom Optics"*, Chin. Sci. Bull. **54**, 348–352 (2024) .

[14] J. G. Bonhnet, C. Zilong, J. M. Weiner, D. Meiser, M. J. Holland, J. K. Thompson, et al., *"A steady-state superradiant laser with less than one intracavity photon"*, Nature **484**, 78–81 (2012) .

[15] M. A. Norcia, M. N. Winchester, J. R. K. Cline, J. K. Thompson, et al., *"Superradiance on the millihertz linewidth strontium clock transition"*, Science Advances **2**, e1601231 (2016) .

[16] S. A. Schäffer, M. Tang, M. R. Henriksen, A. A. Jørgensen, B. T. R. Christensen, J. W. Thomsen, et al., *"Lasing on a narrow transition in a cold thermal strontium ensemble"*, Phys. Rev. A **101**, 013819 (2020) .

[17] S. L. Kristensen, E. Bohr, J. Robinson-Tait, T. Zelevinsky, J. W. Thomsen, J. H. Müller, et al., *"Subnatural Linewidth Superradiant Lasing with Cold* ^{88}Sr *Atoms"*, Phys. Rev. Lett. **130**, 223402 (2023) .

[18] T. Laske, H. Winter, A. Hemmerich, et al., *"Pulse Delay Time Statistics in a Superradiant Laser with Calcium Atoms"*, Phys. Rev. Lett. **123**, 103601 (2019) .

[19] D. Meiser, M. J. Holland, et al., *"Steady-state superradiance with alkaline-earth-metal atoms"*, Phys. Rev. A **81**, 033847 (2010) .

[20] D. Meiser, J. Ye, D. R. Carlson, M. J. Holland, et al., *"Prospects for a Millihertz-Linewidth Laser"*, Phys. Rev. Lett. **102**, 163601 (2009) .

[21] H. Liu, S. B. Jäger, X. Yu, S. Touzard, A. Shankar, M. J. Holland, T. L. Nicholson, et al., *"Rugged mHz-Linewidth Superradiant Laser Driven by a Hot Atomic Beam"*, Phys. Rev. Lett. **125**, 253602 (2020) .

[22] M. Matusko, M. Delehaye, et al., *"Superradiant active optical atomic clocks: motivations and current challenges"*, J. Phys. Conf. Ser. **2889**, 012045 (2024) .

[23] M. A. Norcia, J. K. Thompson, et al., *"Cold-Strontium Laser in the Superradiant Crossover Regime"*, Phys. Rev. X **6**, 011025 (2016) .

[24] J. Cline et al., *"Continuous Collective Strong Coupling Between Atoms and a High Finesse Cavity on a Forbidden Optical Transition"*, PhD thesis, University of Colorado Boulder, 2021, p. 011025.

[25] S. Dubey, G. A. Kazakov, B. Heizenreder, S. Zhou, S. Bennetts, S. A. Schäffer, A. Sitaram, F. Schreck, et al., *"Modeling of a continuous superradiant laser on the sub-mHz* $^1\mathrm{S}_0 \rightarrow {}^3\mathrm{P}_0$ *transition in neutral strontium-88"*, Phys. Rev. Res. **7**, 013292 (2025) .

[26] M. J. Martin, J. Ye, et al., *"High-precision laser stabilization via optical cavities"*, Phys. Rev. Res. **7**, 237–258 (2012) .

[27] F. Famà, S. Zhou, B. Heizenreder, M. Tang, S. Bennetts, S. B. Jäger, S. A. Schäffer, F. Schreck, et al., *"Continuous cavity QED with an atomic beam"*, Phys. Rev. A **110**, 063721 (2024) .

[28] N. Hodgson, H. Weber, et al., *"Optical Resonators: Fundamentals, Advanced Concepts and Applications"*, Phys. Rev. A **110**, 063721 (1997) .

[29] G. Hadley et al., *"Injection locking of diode lasers"*, IEEE J. Quantum Electron. **22**, 419–426 (1986) .

[30] D. W. Preston et al., *"Doppler-free saturated absorption: Laser spectroscopy"*, Am. J. Phys. **64**, 1432–1436 (1996) .

[31] E. D. Black et al., *"An introduction to Pound–Drever–Hall laser frequency stabilization"*, Am. J. Phys. **69**, 79–87 (2001) .

[32] H. Tanji-Suzuki, I. D. Leroux, M. H. Schleier-Smith, M. Cetina, A. T. Grier, J. Simon, V. Vuletić, et al., *"Interaction between Atomic Ensembles and Optical Resonators: Classical Description"*, Adv. At. Mol. Opt. Phys. **60**, 201 (2011) .

[33] M. A. Norcia et al., *"New tools for precision measurement and quantum science with narrow linewidth optical transitions"*, PhD thesis, University of Colorado, 2017, p. 201.

[34] J. Bohnet, Z. Chen, J. Weiner, et al., et al., *"A steady-state superradiant laser with less than one intracavity photon"*, Nature **484**, 78–81 (2012) .

[35] E. D. Black et al., *"An introduction to Pound–Drever–Hall laser frequency stabilization"*, Am. J. Phys. **69**, 79–87 (2001) .

[36] C. Zhou, C. He, S.-T. Yan, Y.-H. Ji, L. Zhou, J. Wang, M.-S. Zhan, et al., *"Laser frequency shift up to 5 GHz with a high-efficiency 12-pass 350-MHz acousto-optic modulator"*, Rev. Sci. Instrum. **91**, 033201 (2020) .

[37] M. Tavis, F. W. Cummings, et al., *"Exact Solution for an N-Molecule-Radiation-Field Hamiltonian"*, Phys. Rev. **170**, 379–384 (1968) .

[38] Y. Zhu, D. J. Gauthier, S. E. Morin, Q. Wu, H. J. Carmichael, T. W. Mossberg, et al., *"Vacuum Rabi splitting as a feature of linear-dispersion theory: Analysis and experimental observations"*, Phys. Rev. Lett. **64**, 2499–2502 (1990) .

[39] H. J. Kimble et al., *"Strong interactions of single atoms and photons in cavity QED"*, Phys. Scr. **T76**, 127–137 (1998) .

[40] G. S. Agarwal et al., *"Vacuum-Field Rabi Splittings in Microwave Absorption by Rydberg Atoms in a Cavity"*, Phys. Rev. Lett. **53**, 1732–1734 (1984) .

[41] M. Rossi, N. Kralj, S. Zippilli, R. Natali, A. Borrielli, G. Pandraud, E. Serra, G. Di Giuseppe, D. Vitali, et al., *"Normal-Mode Splitting in a Weakly Coupled Optomechanical System"*, Phys. Rev. Lett. **120**, 073601 (2018) .

[42] Y. Colombe, T. Steinmetz, G. Dubois, et al., et al., *"Strong atom–field coupling for Bose–Einstein condensates in an optical cavity on a chip"*, Nature **450**, 272–276 (2007) .

[43] J. Ye, L.-S. Ma, J. L. Hall, et al., *"Cavity-enhanced frequency modulation spectroscopy: advancing optical detection sensitivity and laser frequency stabilization"*, Nature **3270**, 85 –96 (1998) .

[44] J. Ye, L.-S. Ma, J. L. Hall, et al., *"Ultrasensitive detections in atomic and molecular physics: demonstration in molecular overtone spectroscopy"*, J. Opt. Soc. Am. B **15**, 6–15 (1998) .

[45] D. Grabovsky et al., *"FM Spectroscopy"*, J. Opt. Soc. Am. B **15**, 6–15 (2017) .

[46] L.-S. Ma, J. Ye, P. Dubé, J. L. Hall, et al., *"Ultrasensitive frequency-modulation spectroscopy enhanced by a high-finesse optical cavity: theory and application to overtone transitions of C2H2 and C2HD"*, J. Opt. Soc. Am. B **16**, 2255–2268 (1999) .

[47] L. Gianfrani, R. W. Fox, L. Hollberg, et al., *"Cavity-enhanced absorption spectroscopy of molecular oxygen"*, J. Opt. Soc. Am. B **16**, 2247–2254 (1999) .

[48] A. Foltynowicz, W. Ma, O. Axner, et al., *"Characterization of fiber-laser-based sub-Doppler NICE-OHMS for quantitative trace gas detection"*, Opt. Express **16**, 14689–14702 (2008) .

[49] G. Gagliardi, H.-P. Loock, et al., *"Cavity-Enhanced Spectroscopy and Sensing"*, Opt. Express **16**, 14689–14702 (2012) .

[50] P. D. Lett, W. D. Phillips, S. L. Rolston, C. E. Tanner, R. N. Watts, C. I. Westbrook, et al., *"Optical molasses"*, J. Opt. Soc. Am. B **6**, 2084–2107 (1989) .

[51] H. L. Stover, W. H. Steier, et al., *"Locking of Laser Oscillators by Light Injection"*, Appl. Phys. Lett. **8**, 91–93 (1966) .

[52] C. Buczek, R. Freiberg, M. Skolnick, et al., *"Laser injection locking"*, Proc. IEEE **61**, 1411–1431 (1973) .

[53] C. L. Tang, H. Statz, et al., *"Phase-Locking of Laser Oscillators by Injected Signal"*, J. Appl. Phys. **38**, 323–324 (1967) .

[54] S. B. Jäger, S. Schütz, G. Morigi, et al., *"Mean-field theory of atomic self-organization in optical cavities"*, Phys. Rev. A **94**, 023807 (2016) .

[55] S. B. Jäger, H. Liu, J. Cooper, T. L. Nicholson, M. J. Holland, et al., *"Superradiant emission of a thermal atomic beam into an optical cavity"*, Phys. Rev. A **104**, 033711 (2021) .

[56] S. B. Jäger, M. J. Holland, G. Morigi, et al., *"Superradiant optomechanical phases of cold atomic gases in optical resonators"*, Phys. Rev. A **101**, 023616 (2020) .

[57] S. B. Jäger, H. Liu, J. Cooper, M. J. Holland, et al., *"Collective emission of an atomic beam into an off-resonant cavity mode"*, Phys. Rev. A **104**, 053705 (2021) .

[58] S. B. Jäger, H. Liu, A. Shankar, J. Cooper, M. J. Holland, et al., *"Regular and bistable steady-state superradiant phases of an atomic beam traversing an optical cavity"*, Phys. Rev. A **103**, 013720 (2021) .

[59] H. J. Metcalf, P. Straten, et al., *"Laser Cooling and Trapping"*, Phys. Rev. A **103**, 013720 (1999) .

[60] M. S. Safronova, D. Budker, D. DeMille, D. F. J. Kimball, A. Derevianko, C. W. Clark, et al., *"Search for new physics with atoms and molecules"*, Rev. Mod. Phys. **90**, 025008 (2018) .

Acknowledgment

I am writing this right after sending out the final question about my thesis, and I want to take a moment to reflect on the journey that brought me here and the people who made it meaningful along the way.
First I would like to sincerely thank my supervisor, Prof. Dr. Florian Schreck, for giving me the opportunity to join his group. We first met online during the chaotic times of the COVID-19 pandemic, and despite the unusual circumstances, you placed your trust in my abilities and welcomed me into the team. I am deeply grateful for this opportunity. I also want to thank you for your guidance, especially in the final six months of my PhD, when your presence in the lab and your work on automating experimental sequences saved me countless hours.
Secondly, I would like to express my gratitude to my daily supervisor, Dr. Stefan A. Schäffer. I am truly grateful for your patience and dedication, for your willingness to explain things repeatedly until I fully understood them. Working with you has been one of the most rewarding experiences of my career, and I feel incredibly fortunate to have had you as a mentor. Beyond your scientific guidance, I deeply appreciate the support you offered during my most stressful, anxious, and difficult moments. I know how challenging it can be to help someone struggling with their mental health (as I face that challenge myself), and I will always be thankful for your kindness, empathy, and support.I sincerely wish you all the best in your career and anyone who has the privilege of having you as a supervisor is truly fortunate.
Now comes the moment where I start thanking a bunch of people—so if you're still reading, I know you've been waiting for this!
First, I want to thank the person with whom I spent an absurd amount of time in the lab: Francesca. Thank you for your friendship, both in and outside the lab. The work we accomplished is a shared achievement.

Next, a huge thank you to Prem for being such a supportive, kind, and brilliant friend. You were always there whenever I needed help—whether with electronics, physics, or just life itself. I truly appreciate your generosity, intelligence, and the joy you bring to those around you. Your great smile and big brain make you impossible not to admire! I'm also really glad we ended up in the same city again—so get ready for more unsolicited hugs!
Benedikt, my dear German crossfiter friend, thank you for being such a great companion from the very first day we met. Sadly, we never got the chance to actually work on the same project (as we were supposed to), but sharing the lab with you was always a pleasure. I appreciate all the help and discussions, whether about physics or sports. Thank you for patiently listening to my endless complaints and somehow still choosing to be my friend. I also have to commend you for taking all my roasting so lightly, it was genuinely fun, and, in my own way, a sign of affection.
Ananyna, you were a fantastic addition to the group. You made the endless lab days more fun and bearable. Thank you for your support, empathy, and kindness—and, of course, for all the spilled juice (and poison) and for joining me on roasting Benedikt. Most importantly, thank you for being such an inspiring representation of a strong, accomplished and smart woman.
Thank you to my friends across the corridor, Ivo and Alex. I love your sense of humor, and I truly miss our lunchtime conversations where you always had strong opinions about life, the universe, and everything else. Those moments brought me so much joy.
Ivo, thank you for joining in on the activities in Kochi. I think that was the first time we really spent time together outside the lab, and it allowed us to get to know each other on a deeper level. I felt more connected with you, and I'm really grateful for that. I'll be looking forwards to when we are going on a bike ride together.
Now, moving further up the corridor starting with Elly. Girl, just thinking about how much you've meant to me over these four long years brings tears to my eyes. What is Amsterdam without you? Definitely less shiny! Elly, you are one of those rare people with whom I felt an instant connection. From the very beginning, it

was like we just clicked, right? I've always been amazed by how, despite coming from such different backgrounds and realities, we are still so alike in so many ways. My dear Elly, I can't think of a single moment when you didn't bring me joy. I admire you deeply, and I feel incredibly blessed to have had you as a friend. Thank you for everything, for the coffees, the brunches, and, most importantly, for being my best raving partner. I miss you, and honestly, life feels a little less sparkly without you around.

Still within the ion crew-Rima, thank you for your support, friendship, and for always being someone I could count on. You were my reality check when I needed one, and I truly appreciate that. Matteo, my dear climbing partner, thank you for always giving me the best route-solving advice—"just climb up." Climbing with you was always a great time! Obrigada, Clara, por sempre me ouvir, me apoiar e me entender, mesmo quando eu estava no meu pior estado. Talvez eu não tenha sido a melhor companhia para se morar, mas sou muito grata pelo tempo que tivemos juntas na casinha. Louis, it's remarkable how, despite barely understanding each other's accents, we still became friends and shared so many great moments on the dance floor. Zager and Nela, thank you for always being such wonderful (and impressively tall) people to be around. Your presence made every moment more enjoyable.

I'd also like to thank some wonderful people from the Soft Matter group: Ina, Marcus, Felipe and Marius. Thank you for the coffee corner moments, the beers, and all the fun times! Elham, thank you for your unwavering support and for always being incredibly kind to me. You are an amazing, sweet, and strong woman, and I truly admire you. I wish you could see yourself through my eyes. Now, going beyond the IoP walls, I would like to thank my friends Ana and Thomas. My life improved 100% after you entered in my life. You made me feel so welcomed since the first day we met (that was a Kings day!). I can't express enough how much I'm grateful for everything you two have done for me during those four years. You were crucial in so many ways and times of this journey. I wish one day I can retribute a bit of everything you have done for me. You two became my international family, which I always felt and knew that I could count on and I'm deeply grateful for it.

Quero agradecer aos meus amigos e conterrâneos que me acompanham desde muito antes. Primeiramente, Natalia, quero te agradecer por ser uma das pessoas mais constantes na minha vida ao longo dos anos. Obrigada por tanto e por tanto tempo. Obrigada por todo o apoio, por me entender em praticamente todos os aspectos e por "segurar minha mão", mesmo à distância. Você é meu porto seguro. Já passamos por tanta coisa e chegamos tão longe—coisas que nossas versões de anos atrás jamais teriam sonhado. E estarei sempre ao seu lado para lembrar da nossa história e da nossa jornada. Obrigada por ser minha inspiração há quase 10 anos—e por continuar sendo.

Obrigada Anne, Gabi, Isa e Brenda. Vocês me conhecem há tanto tempo, e conversar com vocês me recarrega, me faz olhar para minha história e me faz sentir em casa de uma maneira que nem consigo expressar. Obrigada por fazerem com que, apesar da inconstância, a amizade permaneça. Sempre que falamos, parece que o tempo parou e que nos encontramos ontem—mesmo que mil coisas tenham acontecido desde então. Esse sentimento de carinho e pertencimento me aquece e me renova, e é crucial para que eu aguente 'só mais um pouquinho' estar fora do Brasil.

Por fim, quero agradecer aos meus pais, Rosilene e Edson. Eu admiro profundamente a história de vocês e sou grata por todos os sacrifícios que fizeram pela nossa família. Hoje consigo olhar para nossa história e entender o quanto tudo foi difícil. Obrigada por me incentivarem a estudar, por não deixarem eu desistir quando eu achava que não ia aguentar mais. Obrigada por, mesmo sem entender o que eu faço, nunca se oporem a isso—mesmo quando decidi morar em um país do outro lado do oceano. Obrigada por sempre terem sido um grande exemplo de resiliência. Talvez eu não tivesse tido a coragem de me mudar para outro país para fazer um doutorado se não fosse pela nossa história de tantas mudanças (11 vezes, certo?). Sem perceber, talvez, vocês me ensinaram a sempre buscar algo a mais, a explorar novas chances e oportunidades, a procurar novos horizontes e aprender a lidar com a saudade. O coração de vocês sempre ficou em casa branca, mas nada disso os impediu de seguir em frente. O meu ficou no Brasil, mas sigo em frente por enquanto, até o dia que eu consiga voltar, mesmo que seja brevemente. Amo vocês.

To everyone else who has been a positive presence in my life over the past four years, many thanks. I truly appreciate it. If we shared good moments, even if I didn't explicitly mention you here, know that I value them. Knowing me, I've probably already said something in person, and if not, I'll make sure to express it another time. Finally, but certainly not least, as Anitta once said, "Thanks to me. I want to thank myself, because I worked so hard, omg."